INTENSE SHALLOW MAGMA SEDIEMENT MINGLING WITHIN DIKES AT GUFFEY BUTTE MAAR, IDAHO

A THESIS IN

Environmental and Urban Geosciences

Presented to the Faculty of the University

of Missouri-Kansas City in partial fulfillment of

the requirements for the degree

MASTER OF SCIENCE

by

HANNAH GRACHEN

B.A., The College of Wooster, 2020

Kansas City, Missouri

2022

INTENSE SHALLOW MAGMA SEDIMENT MINGLING WITHIN DIKES AT GUFFEY BUTTE MAAR, IDAHO

Hannah Grachen, Candidate for the Master of Science Degree

University of Missouri-Kansas City, 2022

ABSTRACT

The interactions between magma and shallow unconsolidated sediments on the way to the surface influences the eruption behavior and products. Phreatomagmatic eruptions are a result of the interaction of magma and water or wet sediment and their deposits are evidence of this interaction. The relative influence of internal magmatic and external environmental factors that control magma sediment interaction are not well constrained. This study focuses on exposed dike structures in an eroded Pleistocene basalt maar complex, Guffey Butte, Idaho to investigate extreme sediment magma mingling in a non-explosive environment. Exposed dikes cut through both lake Idaho sands and silts and Guffey Butte pyroclastic deposits. Through a combination of field mapping, microtexture measurements from 36 thin sections, and geochemistry (whole rock major and trace elements using XRF and ICP-MS), the scales of interactions and diversity of mixing styles between the basaltic dikes and host sediments were constrained. The two host materials were characterized for componentry and grain size. Field observations reveal the scales of these interactions range from blocks (< 10 cm) to individual crystals. GB basalts contain less lithics than mixed samples. The intensity of mingling is diverse and the style of mingling over a spatial area is not systematic. Magma penetrated through wet unconsolidated siliciclastic sediment and due

to their differing densities mixing occurs through Kelvin-Helmholtz Instability. Mingling is separated into three categories: 1) Least Homogenized, 2) Moderate Homogenization, and 3) Homogenized. The different levels of mixing preserve the different stages of Kelvin-Helmholtz instability over a distance of a few cm to meters. In thin section, changes in crystal, sedimentary grain, and basalt fragment sizes occur as well as injections of sediment into basalt and basalt into sediment at the mm scale. Basaltic and siliciclastic mineral preservation suggest mixed dike temperatures to be slight below 900°C - 1,000°C. This study expands the observed range of interactions between wet sediments and shallow basaltic intrusions that can occur in a non-explosive environment.

APPROVAL PAGE

The faculty listed below, appointed by the Dean of the College of Arts and Sciences, have examined a thesis titled “Intense Shallow Magma Sediment Mingling within Dikes at Guffey Butte Maar, Idaho” presented by Hannah Grachen, candidate for the Master of Science degree, and certify that in their opinion it is worthy of acceptance.

Supervisory Committee

Alison H. Graettinger, Ph.D., Committee Chair

Earth and Environmental Sciences

Tina M. Niemi, Ph.D.

Earth and Environmental Sciences

Jejung Lee, Ph.D.

Earth and Environmental Sciences

CONTENTS

LIST OF ILLUSTRATIONS

LIST OF TABLES

Table Page

ACKNOWLEDGEMENTS

Thank you to my advisor, Alison Graettinger, who has been incredibly supportive, encouraging, and immensely compassionate. Thank you for taking a 40 hour road trip with me to do field work in the desert during a heatwave and for making field work so much fun. Your unwavering enthusiasm and passion for the geosciences has been an inspiring and motivating force during my masters. I cannot thank you enough for the opportunities that you have presented me with as a graduate research assistant, graduate teaching assistant, and speaker. Thank you for sharing your wealth of knowledge in the geosciences, music, and culinary arts. Even though you may have misled me to think that Kate Bush was the Australian Björk. Thank you for being someone I can bond with over my love for Pittsburgh sports and Yinzer culture!

Special thanks to Topher Hughes for his never-ending kindness and support. In addition, to motivation to keep writing.

Thank you to Kadie Bennis for being my sounding board, zoom movie pal, and go to person when I need support the most. I am so thankful for your never ending positivity, knowledge, and insight which has been invaluable to this project's success.

Thank you to Aaron Galletly for going out in the field with me. I am truly grateful for your spontaneity and amazing friendship. Thank you so much for helping me make my 3D models of my mixed dikes through photogrammetry. Without you I wouldn't have been able to make these amazing models. Thank you for showing me around Kansas City and introducing me to great restaurants in the area. Without you I would have most likely not seen anything in town.

Thank you to the MELTS Lab for supporting me through my time at UMKC and making my masters such a positive experience; Kadie Bennis, Aaron Galletly, Alex Bearden, Kyle Broley, Brooke Benz, Ivana Torrez, Joe Nolan, and honorary member Trenton McEnaney. I have learned so much from all of you and greatly appreciate the friendship you have given me.

Thank you to Garrett Tinline and Leman Simpson who have supported me through completing this research and degree. I am really great full that you both would check in every so often and that you are always available to talk no matter what is happening in your life.

Lastly, muchísimas gracias a mi familia. Gracias a mi madre pro su aliento interminable, sin importar cuán loco sea mi objetivo. A mi hermanita, Gabriela, por ser mi voz de la razón y estar siempre a una llamada de distancia. Gracias a mis primas Michi y Vero que han sido tan alentadoras, solidarias y amorosas.

CHAPTER 1. INTRODUCTION

Phreatomagmatic eruptions are the result of magma water or wet sediment interactions which could lead to either an explosive or non-explosive eruption. Guffey Butte is a prime study site as is a maar complex created by an explosive eruption when magma interacted with wet unconsolidated siliciclastic sediment about 1 MA. Guffey Butte is located in southwester Idaho and is a part of the Western Snake River Plain. The youngest periods of volcanism in the Western Snake River Plain coincides with the late stages of Lake Idaho. This is a series of lakes which were once present in southwestern Idaho and parts of eastern Oregon (Godchaux *et* al., 1992). In the early Pleistocene Lake Idaho drained but the siliciclastic sediment remained saturated (Jenks and Bonnichsen, 1989). The focus of this study are the well exposed dikes found within the crater and along the flanks and are non-explosive.

1.1 Phreatomagmatism

Phreatomagmatic eruptions are the result of magma water or wet sediment interactions (Zimanowski *et al*. 1991; White, 1996; Befus *et al*., 2008; Bennis and Graettinger, 2020; Nemeth and Koski, 2020). Variables which affect the degree of explosivity from magma water interactions are not well constrained (Casas *et al*., 2018). Siliciclastic host sediment composition, magmatic properties, and water depth are but a few of these variables.

1.1 Molten Fuel-Coolant Interaction

The driving force of phreatomagmatic explosions is the heat transferred between magma and water (Valentine *et al*., 2014). Explosive reactions are not always guarantied through this reaction as a vapor film (Leidenfrost effect) acts a barrier preventing direct

contact of the two interfaces and rapid heat transfer (White *et al*., 1996; Zimanowski *et al*., 1997). Experimental work done by Moitar *et al*. (2020) showed that stable vapor films (1-2 mm) formed at temperatures higher than the Leidenfrost temperature (675-950°C), between 50-250°C below the temperature of liquid basalt found outside a lab setting. The vapor films were stable for a short time (≤5 seconds for samples of magma about 3.2 cm in diameter) before it enters at nucleation boiling regime, in which bubbles form at the surface of the magma, and then they system enters a free convection regime as the temperature at the surface of the magma decreases (Moirtra *et al*., 2020). With increasing water temperatures, a lower Leidenfrost temperature was achieved resulting in the stable vapor film to be sustained for a longer period of time. The short time scale of the vapor films stability could provide constraints to the time available for ample magma-water mixing needed for an energetic explosion in nature (Moitra *et al*., 2020), where magma is more abundant and has sustained temperatures above Leidenfrost temperatures for longer periods of time.

Molten fuel-coolant interaction (MFCI) describes the rapid transfer of heat which triggers phreatomagmatic explosions (Figure 1.1) (Wohletz, 1986; Zimanowski *et al*., 1997; Buttner *et al*., 2002; Sonder *et al*., 2018; Nemeth and Kosik, 2020). MFCI have four phases, described by Zimanowski *et al*. (1997), that occurred in a matter of microseconds: 1) a hydrodynamic mixing phase, 2) a trigger phase, 3) a fine fragmentation phase, and 4) a vaporization and expansion phase. The vapor film serves as a thermal insulation barrier and the boiling interface fragments the magma gradually (Wohletz, 1986). As fragmentation continues, a weak shockwave (<10 J) occurs (Zimanowski *et al*., 1997) that triggers the condensation of the vapor film (Buttner *et al*, 2002). The two interface make contact with each other and the melt is quenched as it comes into contact with water, increasing the heat

transfer rate (Zimanowski *et al*., 1997; Buttner *et al*., 2002). Fracturing of the melt continues to occur, which rapidly increases the area of heat transfer, and increases the heat flux (Wohletz, 1986; Buttner *et al*., 2002). The water is then superheated to the point of spontaneous homogeneous nucleation (Wohlets, 1986), resulting in vaporization and expansion, and thus an explosion (Zimanowski *et al*., 1997; Buttner and Zimanowski, 1998).

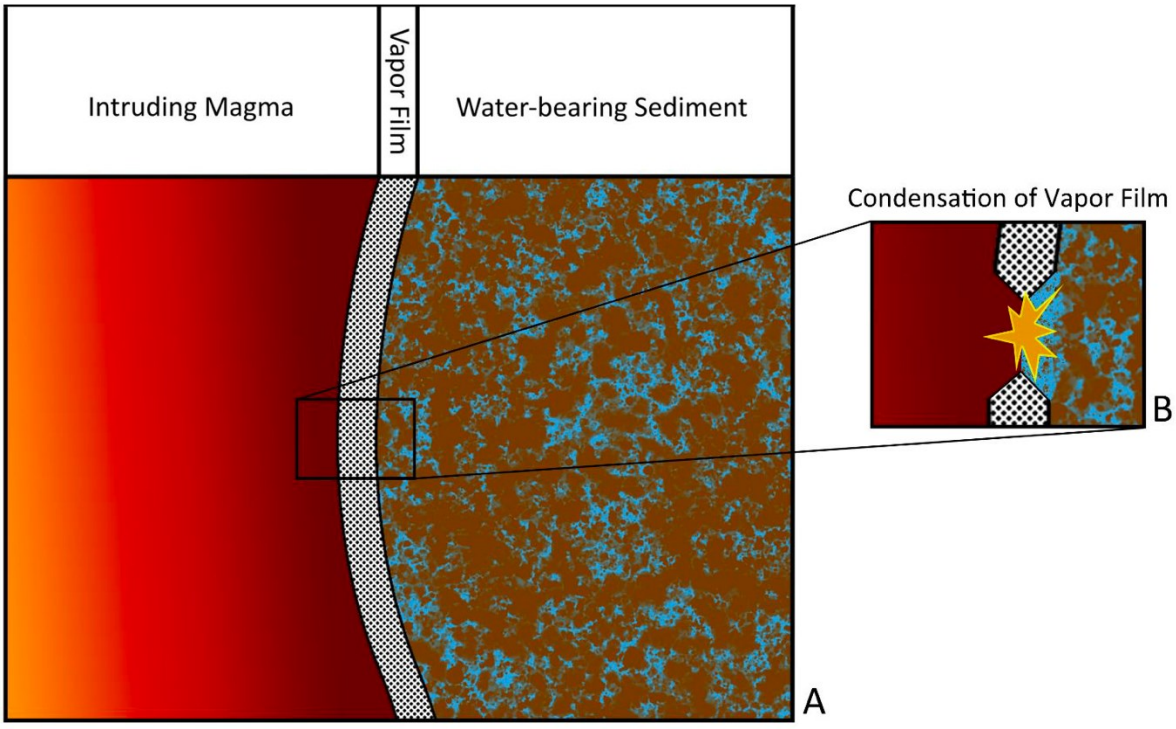

Figure 1. 1 A simplified representation of Molten Fuel-Coolant Interaction. A and B occur sequentially within microseconds, not simultaneously. A) The vapor film serves as an insulating barrier between the intruding magma and the water-bearing sediment. The boiling interface fragments the magma gradually and the mixing of magma and water occurs. B) A weak shockwave triggers the condensation of the vapor film that allows the magma to contact the water-bearing sediment. A rapid transfer of heat then occurs and the water becomes superheated, producing an explosion (Galletly, 2021).

1.3 Maar

Maars are volcanic landforms that are the product subsurface phreatomagmatic eruptions. These explosions result in a distinctive crater that is surrounded by an ejecta ring and has a floor beneath the pre-eruptive surface. Their crates are created by multiple, tens to hundreds, discreate explosions caused by the interaction of magma and ground water (Nichols and Graettinger, 2021; Ross *et al*., 2017; Valentine *et al*., 2017; White and Ross, 2011). The subsurface phreatomagmatic eruptions create an inverted cone of sediment in the subsurface leaving the crater and the tephra ring as a distinguishable surface expression (Figure 1.2).

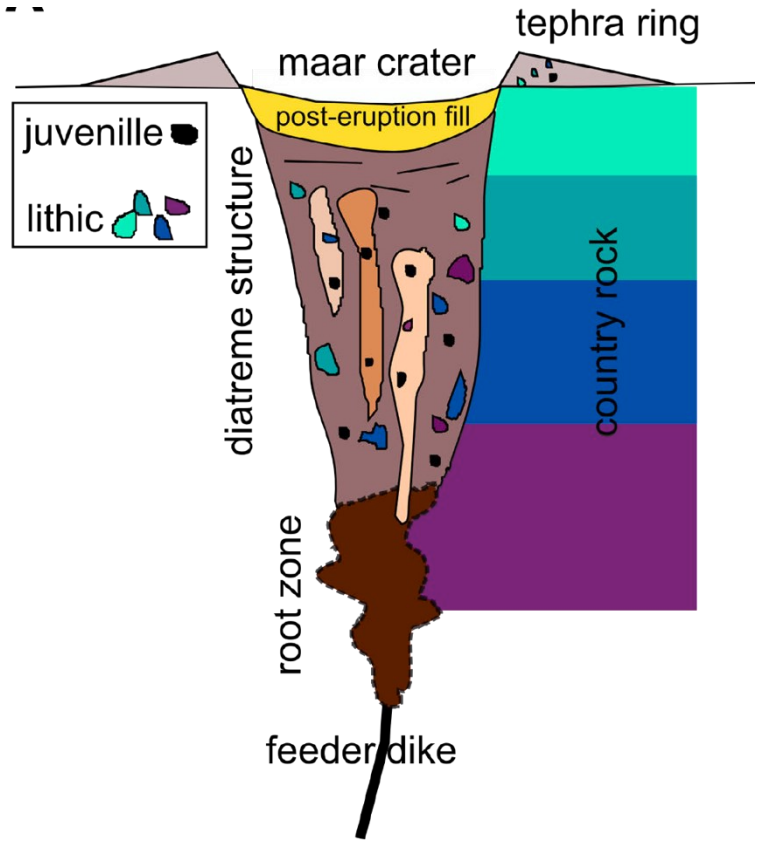

Figure 1. 2 Cartoon drawing showing the subsurface structure of a maar. Colored clasts represent the mixing of volcanic and country rock material within the diatreme (Nichols and Graettinger, 2021).

Any sediment ejected may fall back into the crater making the true depth of the crater unknown. Volcanic activity has affected vast areas including many sedimentary basins around the world (e.g. Bischoff *et al*., 2017; Breitkreuz and Rocchi, 2018; Caineng *et al*., 2013; Coffin and Eldhom, 1994; De Luca *et al*., 2015; Senger *et al*., 2017). The sedimentary systems present during volcanism influences the type volcanic and sedimentary facies created and their preservation (e.g. Ebinghaus *et al*., 2014; Hole *et al*., 2013; Jerram *et al*., 2016a; Ross *et al*., 2005; Waichel *et al*., 2007).

1.4 Non-Explosive feature in an Explosive Environment

The emplacement of non-explosive features in an explosive environment through the interaction of magma and wet sediment have been mentioned by several researchers in locations that have experienced explosive phreatomagmatic eruptions (Zimanowski *et al*., 1991; Dvark, 1992; White, 1996; Starostin *et al*., 2005; Befus *at al*., 2008; Befus *et al*., 2009; Baker *et al*., 2015; Amin and Valentine, 2007; van Otterloo *et* al., 2018; Bennis and Graettinger, 2020; Graettinger *et al*., 2020). Field examples of these interactions include billowed dikes (Hanson and Hargrove, 1999, Kano, 2002; Lavine and Aalto, 2002; Befus *et al*., 2009; Bennis and Graettinger, 2020), peprites (Busby-Spera and White, 1987; White *et al*., 2000; Hooten and Ort, 2002; Skilling *et al*., 2002; White and Houghton, 2006; Befus *et al*., 2009, McLean *et al*., 2016; Kwon and Gihm, 2017; Bennis and Graettinger, 2020; Graettinger *et al*., 2020), convoluted dikes at depth (Befus *et al*., 2009; Muirhead *et al*., 2016), and dikes at shallow depths (top 100m) (Graettinger, 2012; Graettinger *et al*., 2012, Re *et al*., 2016)

Guffey Butte maar is representation of a basaltic maar tuff cone complex where a single complex of magma erupted into unconsolidated siliciclastic sediment that produced

subsurface phreatomagmatic explosions in addition to the non-explosive transport of magma through unconsolidated wet sediment (Murrow, 1996; Watson, 1999; White and Michaud, 2004). What separates the dikes of Guffey Butte from other features created through the interaction of magma and wet siliciclastic sediment at depth is the extent that the magma and host sediment have integrated with each other allowing for a range of textures, hardness, vesicularity, ratio of basalt to host sediment, and lithic content.

1.5 Snake River Plain

The Snake River Plains (SRP) volcanism is associated with the migration of the Yellowstone hotspot and is considered to be an extensive igneous province that extends from southern Idaho to eastern Oregon and northern Nevada (Shervias et al., 2002; Bonnichsen et al., 2016). Primitive volcanism of the SRP is associated with early phases of the Columbia River Basalts that migrated due to movement of the North American Plate (Bonnichsen et al., 2008). The SRP displayed bimodal basaltic and rhyolitic volcanism which spans from northern Nevada and southern Idaho to Yellowstone National Park in northwestern Wyoming (Jenks and Bonnichsen, 1989). Three major regions make up the SRP each experiencing different tectonic environments and are geologically unique: the Eastern Snake River Plain (ESRP), the Central Snake River Plain (CSRP), and the Western Snake River Plain (WSRP). Crustal extension, between 12-7 Ma, in the northeast to southwest direction, produced an intracontinental normal fault 300 km long and 70 km wide (Wood and Clemens, 2002; Bonnichsen et al., 2008). This is what is now known as the WSRP in the southwestern portion of Idaho (Figure 1.3).

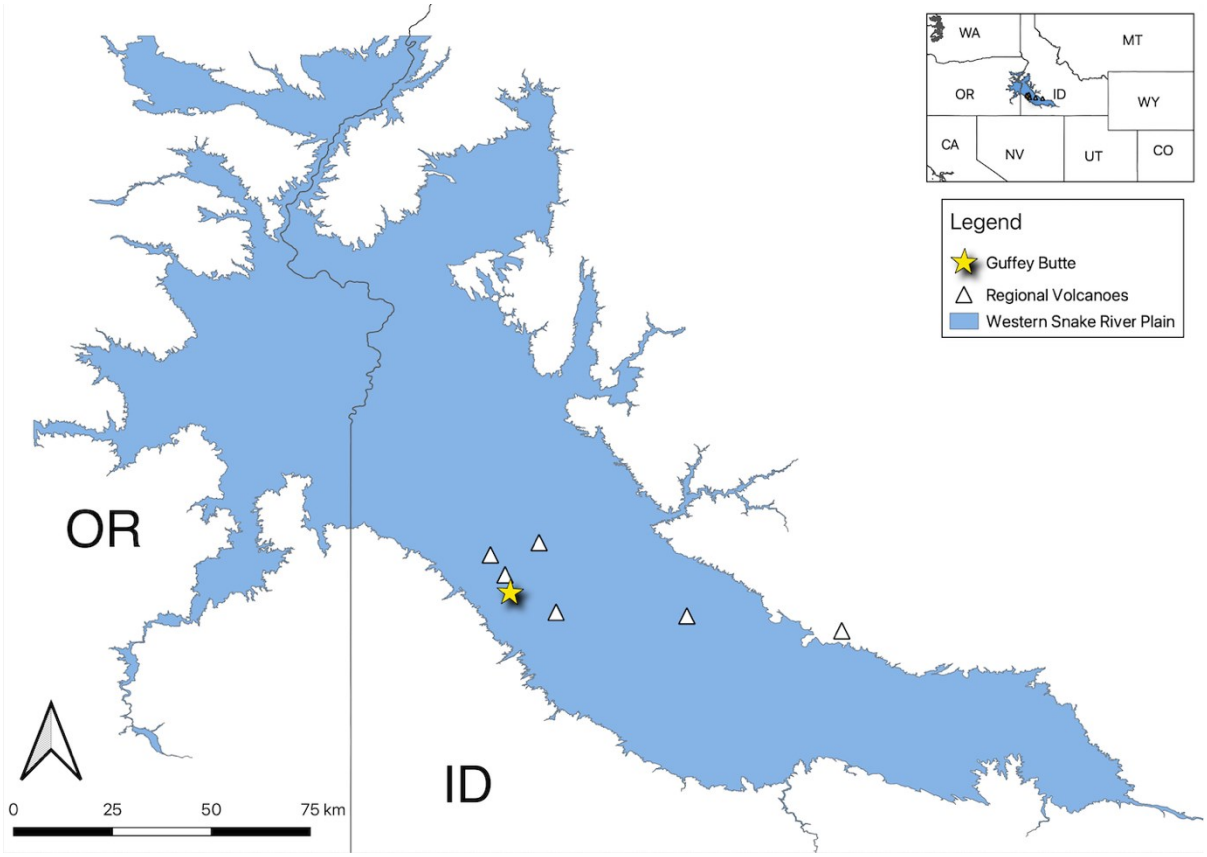

Figure 1. 3 Map showing the location of the Western Snake River Plain in beige in relation to the border between Idaho and Oregon. This figure is edited from Bennis 2019.

The WSRP was subject to rapid subsidence, between 9.5-1.7 Ma, and became an inundated freshwater lacustrine system referred to as Lake Idaho (Wood and Clemens, 2002). Lacustrine deposits from Lake Idaho are 1-2 km thick were placed in the WSRP from Lake Idaho (Wood and Clemens, 2002). Basaltic eruptions are interfingered with lacustrine sediments (Jenks and Bonnichsen, 1989; Godchuax and Bonnichsen, 1992; Shervais *et al*., 2002; Brand and White, 2007; Nemeth and White, 2009). It is suggested, by Shervias *et al*. (2002), that a potential source of the basaltic volcanism occurred in conjunction to mantle plume source of the Columbia River Plateau 9 Ma. The younger episodes are thought to be connected to the Yellowstone hotspot. A hiatus between the basaltic eruptions occurred allowing for deposition and sedimentation. In addition, there is a notable absence of pyroclastic deposits until the basaltic eruptions commenced between 2.2-0.4 Ma (White *et al*., 2002; Bonnichsen *et al*., 2016).

Lake Idaho started to drain and was soon replaced by river systems which accelerated the erosion in the WSRP. In turn, this caused a change in eruptive style (Bonnichsen and Godchaux, 2002) as well as exposed undisturbed lacustrine sediment beneath the volcaniclastic sediment. In the early Pliocene and late Pleistocene, volcanism and sedimentation overlaps leading to explosive and effusive phreatomagmatic eruptions (Shervais *et al*. 2002). The interaction between magma and water and/or wet unconsolidated sediment has the potential to lead to phreatomagmatic eruptions (Zimanowski *et al*., 1991; Dvorak, 1992; White, 1996; Starostin *et al*., 2005; Befus *et al*., 2008; Amin and Valentine, 2017; van Otterloo *et al*., 2018). A multitude of eruptive stages altering between phreatic, phreatomagmatic, and magmatic eruptions are exhibited by these vents. The three eruptive

stages are associated with subaqueous, emergent, and subaerial volcanoes (Godchaux *et al*., 1992). About 10% of the volcanoes in the WSRP, Miocene in age, erupted in subaqueous environments below Lake Idaho (Bonnichsen *et al*., 2016).

1.5 Guffey Butte

Guffey Butte is located in Canyon Country in WSRP of Idaho across from Celebration Park and adjacent to the Snake River (Figure 1.4). It is just southeast of Walters Butte and is one of many late Quaternary volcanoes in the WSRP. It is part of an array of volcanoes in the center of the WSRP: Walters Butte, Sinker Butte, White Butte, Hat Butte, and Kunan Bute. Guffey Butte is an eroded basalt maar 1 Ma and erupted into SRP silts and sands (Watson, 1999; Murrow, 1996). It is composed of bedded tuff, massive tuff, cinder and spatter. Erosion to a depth of -27.21 m exposed multiple diatreme vent structures, large stratigraphic sections, and dikes inside the center and on the flanks. Pre-eruptive deposits are made up of the Glenns Ferry Formation. There are a bunch of dikes on SE side of the structure that display lots of xenolithic material and are the focus of this study.

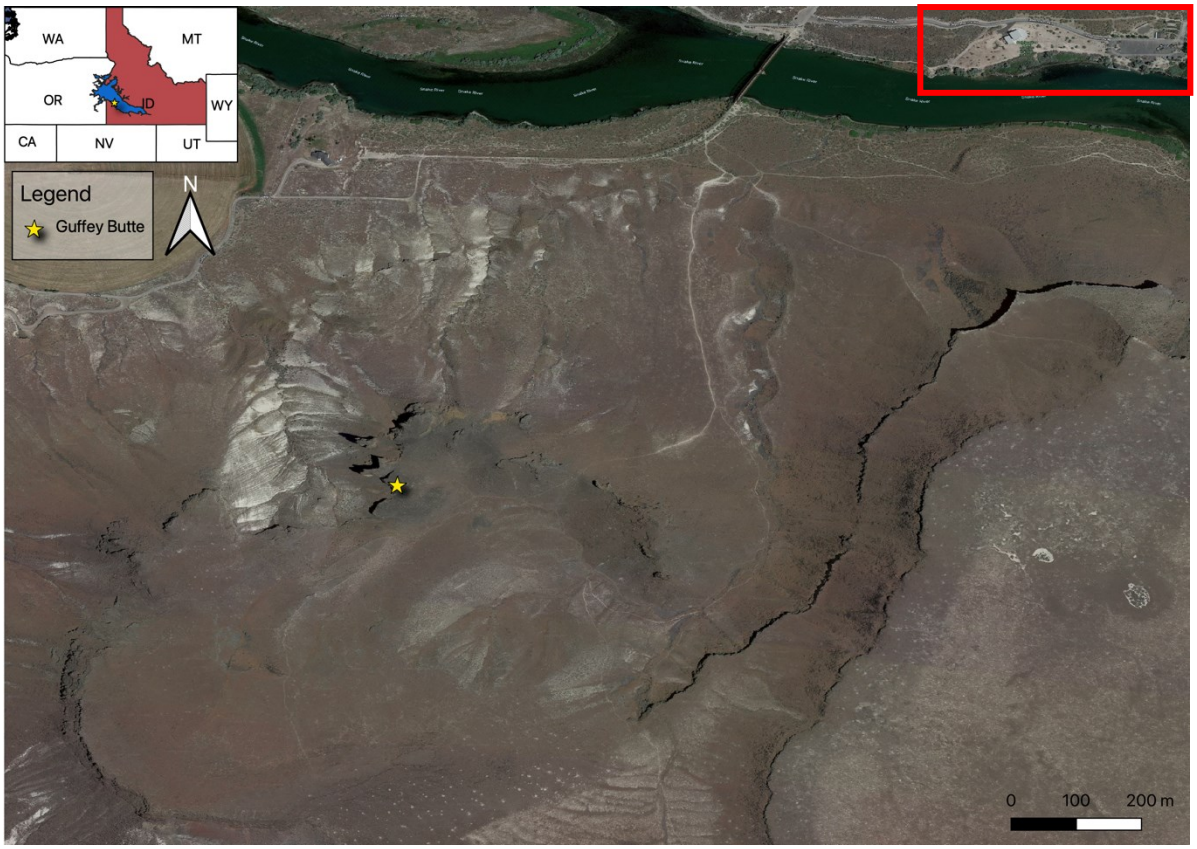

Figure 1. 4 Map showing the location of Guffey Butte (star) across from Celebration Park that is highlighted in the red box and the Snake River..

1.5.1 Glenns Ferry Formation

The Glenns Ferry Formation has an exposure thickness of ~609.6 m consists of fluvial, lacustrine, floodplain deposits, and small quantities of volcanic material (Malde and Powers. 1962; Swirydczuk *et al*., 1981a). The formations basal beds are made up of massive arkose sand, fine grained gravel, and carbonate oolites (Malde and Powers, 1962; Swirydczuk *et al*., 1981a; Swirydczuk *et al*., 1981b). Based on area and volume, the lacustrine facies is the largest and consist of tan, silty layers with some containing faint, diffused bedding or ripple marks (Malde and Powers, 1962; Swirydczuk *et al*., 1981a). The lacustrine facies have traces of secondary gypsum that are associated with the siliceous ash (Malde and Powers, 1962) (Figure 1.5). The fluvial facies are primarily comprised of thick parallel bedded, unevenly layered pale brownish-gray sand and silt with several layers of crossbedding and ripple marks (Malde and Powers, 1962' Swirydczuk *et al*., 1981a). Amongst the fluvial layers are some beds of calcareous olive silt, dark-olive clay, and paper shale which are indicative of flood-plain facies (Malde and Powers, 1962; Swirydczuk *et al*., 1981).

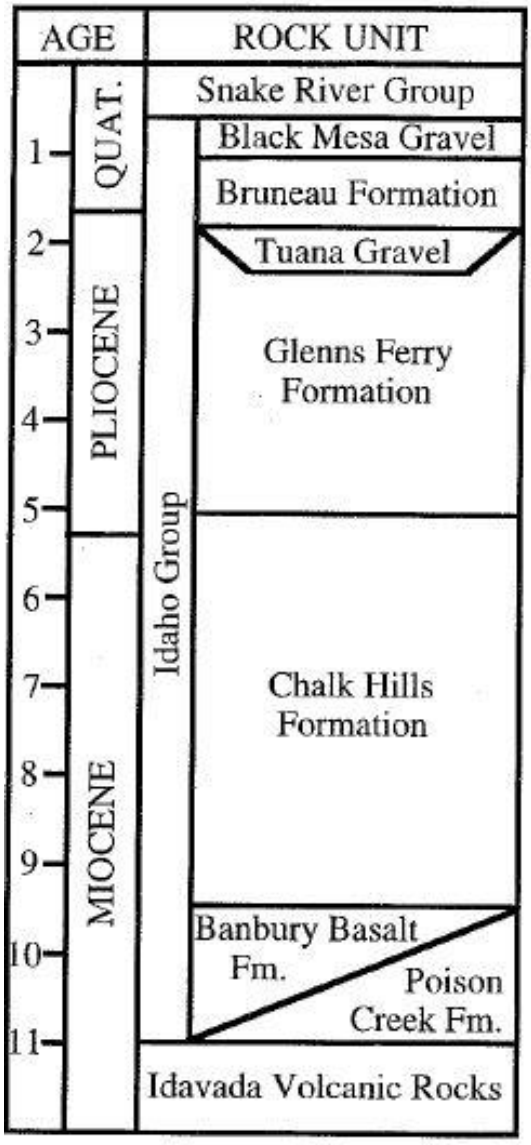

Figure 1. 5 Cenozoic stratigraphy of the Western Snake River Plain (Malde, 1991). Intrusions from Guffey Butte intrude through the Glenns Ferry Formation.

CHAPTER 2. GUFFEY BUTTE

2.1 Methodology

A week of fieldwork was conducted to take structural measurements, map and describe sediment-magma interfaces, and describe host sediment. Componentry and grain sizes of pyroclastic and sedimentary host material were analyzed. Thirty-seven samples were collected: 4 pyroclastic host, 3 siliciclastic host, 14 basalt, 13 mixed dike samples, 3 mixed columnar joints, and 3 margins.

Field maps were created utilizing a culmination of field photos, observations, and measurements of the dikes in addition to their surrounding host sediment. GPS locations recorded latitude, longitude and elevations using WGS 84 Geographic System. These were used to construct maps in ArcGIS Pro v.2.9. A topographical map, at a a contour interval of 20 ft, of Guffey Butte was produced using a digital elevation model from the United States Geological Survey (USGS) (Figure 2.1).

Thirty-six billets were cut and sent to the National Petrographic Service to produce thin sections. Photomicrograph mosaics and petrologic descriptions were generated from thin sections. Major and trace element data was gathered from six samples of the intrusive material, 2 basalt rich and 2 heavily mingled, through X-Ray Fluorescence (XRF) and Inductively Coupled Plasma Mass Spectrometry (ICP-MS) at the Washington State University GeoAnalytical Laboratory. Point counts in thin section, hand sample, and field photos were done to quantify the amount of minerals and lithics in each sample using JMicroVison (1.3.4). The same process was done for lithic types, sedimentary or basalt, found in hand samples and field photos of outcrops. Crystals smaller than 0.0025 mm were not counted as they were too small to properly identify. Mineral percentages were then

converted to counts based off the total points counted. Eleven polished thin sections were analyzed using a Tuscan Vega 3LMU Scanning Electron Microscope, Backscatter electron image (BSE), and Energy Dispersive X-Ray Spectroscopy (EDS) at the University of Missouri-Kansas City. The beam intensity was set to 15 and the High Voltage (HV) at 20 kV. All samples were carbon coated to reduce charging. The Bruker Quantax 200 EDS System was used to create elemental maps of whole BSE images. The Multipoint tool aided in identifying specific major phenocrysts, groundmass, microlites, and vesicles to analyze EDS spectra (Appendix). The QMap function at 1/8 resolution created elemental maps for the backscatter images (Appendix).

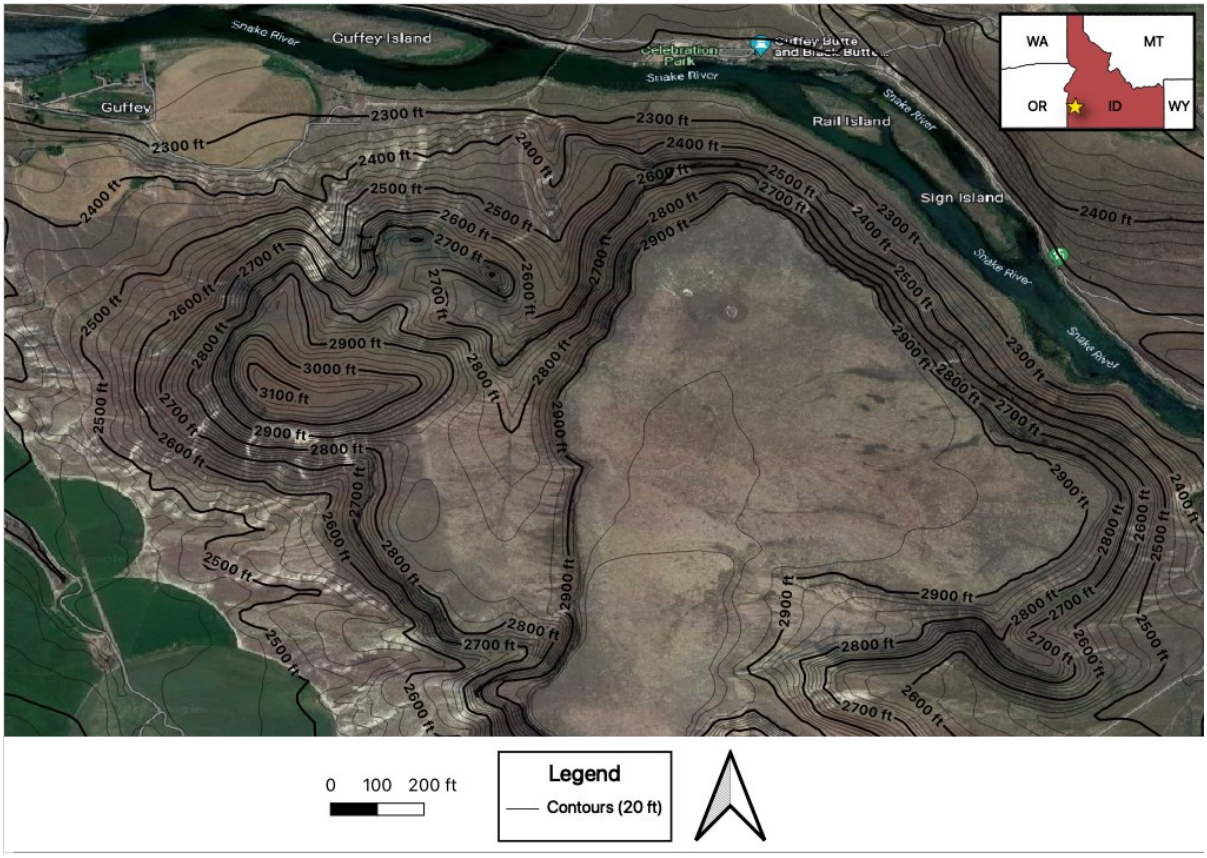

Figure 2. 1 Topographic map of Guffey Butte.

CHAPTER 3. RESULTS: FIELD DESCRIPTIONS, PETROGRAPHY, AND GEOCHEMISTRY

3.1 Deposits

Thirty-seven samples were taken from the host sediments, basaltic dike, and mixed dike (Table 3.1). Categories were defined using field and thin section observations. Thirty-six thin sections from deposits were into five categories: host sediments, basalt, least homogenized intrusions, moderate mixing intrusions, and homogenized intrusions (Figure 3.1). All 36 thin sections were analyzed using a petrographic microscope to identify the minerals present, microtextures, and growth patterns. Point counts of thirty-four thin sections were done from mosaic photomicrographs. Crystals smaller than 0.003 mm were not counted as it was difficult to identify exactly what mineral it was. The point count data was then separated into categories for analysis: Plagioclase (Pl), Quartz (Qtz), and Other. The point totals and their N numbers can be found in the appendix. Of the thin sections twelve were analyzed using SEM-EDS for mineral identification and groundmass analysis. All hand sample analysis can be found in the appendix.

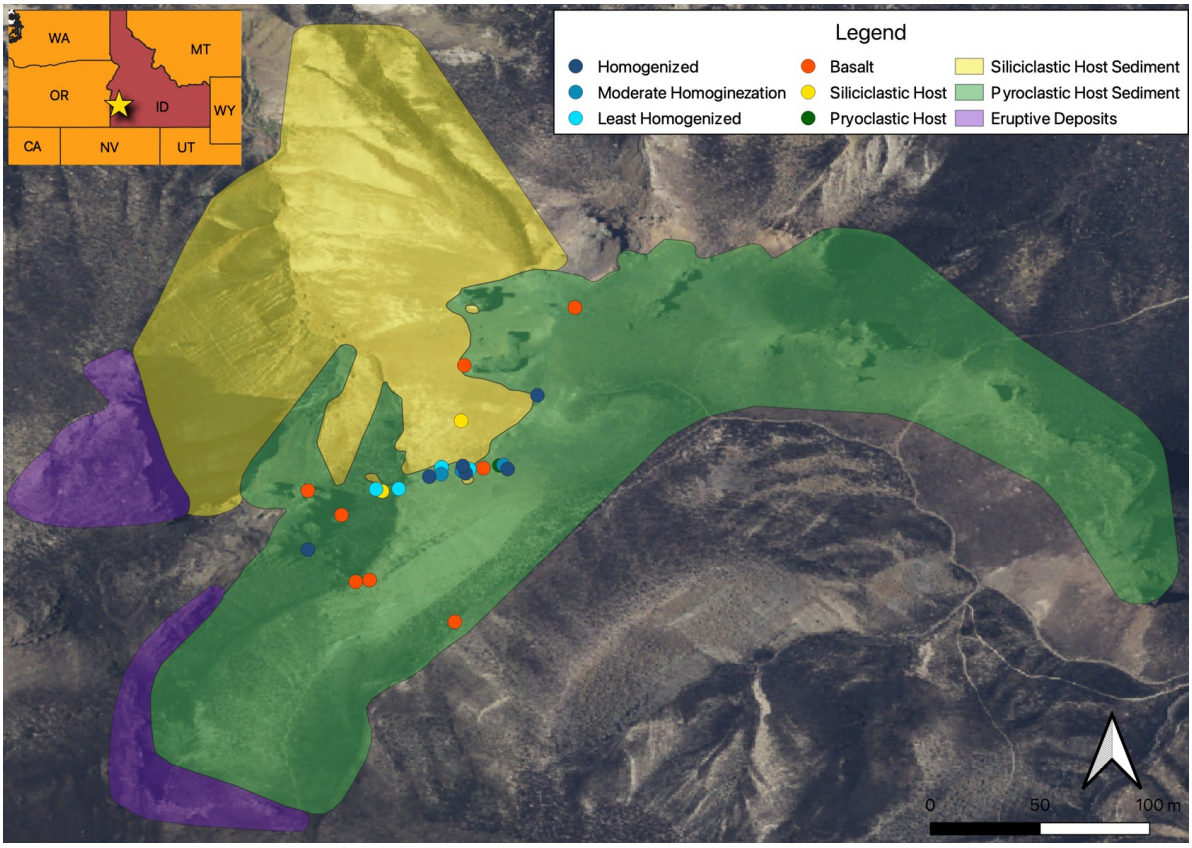

Figure 3. 1 Map of Guffey Butte with the locations of all thirty-six samples collected color coded by lithology. Polygons represent areas of the maar where each host type can be found. There is some overlap of samples that were collected close to each other.

Sample ID	Lithology	Depth (m)	Distance from Mixing Dike (m)
21-HG-029	Lapilli Tuff	-58.7	89
21-HG-023	Scoria	-77.6	75
21-HG-011	Tuff	-64.9	29
21-HG-037	Lapilli Tuff	-59.1	23
21-HG-035	Sandstone	-24.5	45
21-HG-030	Silstone	-36.7	13
21-HG-031	Sandstone	-36.7	13
21-HG-001	Basalt	-86.8	168
21-HG-002	Basalt	-86.8	168
21-HG-034	Basalt	-70.7	142
21-HG-036	Basalt	-39.7	96
21-HG-027	Basalt	-55.3	90
21-HG-028	Basalt	-58.7	89
21-HG-022	Basalt	-77.6	71
21-HG-021	Basalt	-77.6	71
21-HG-019	Basalt	-60.9	40
21-HG-020	Basalt	-57.0	32
21-HG-003	Basalt	-64.9	29
21-HG-004	Basalt	-64.9	29
21-HG-013	Basalt	-37.5	17
21-HG-005	Basalt	-56.9	12
21-HG-006	Least Homogenized	-51.4	
21-HG-018	Least Homogenized	-43.6	
21-HG-014	Least Homogenized	-37.5	
21-HG-012	Least Homogenized	-37.5	
21-HG-017	Least Homogenized	-27.2	
21-HG-032 (a,b)	Moderate Homoginezation	-59.1	
212-HG-009	Moderate Homoginezation	-56.8	
21-HG-015	Moderate Homoginezation	-39.6	
21-HG-010	Moderate Homoginezation	-38.1	
21-HG-024	Homogenized	-77.6	71
21-HG-025	Homogenized	-77.6	71
21-HG-026	Homogenized	-77.6	71
21-HG-033	Homogenized	-64.9	
21-HG-008	Homogenized	-46.0	
21-HG-007	Homogenized	-43.8	
21-HG-016	Homogenized	-39.6	

Table 3. 1 List of samples collected ordered by their lithology then radial distance from the mixed dike. If a distance is not listed the samples are ordered by depth. The colors correspond to the colors used in maps and annotated photos. Depths were calculated using the presumptive surface at 868.7 m.

3.1.1 Host Sediment

Five host sediment samples were collected including four pyroclastic and three sedimentary deposits (Figure 3.2). Pyroclastic deposits were the most predominant host sediment type followed by siliciclastic material from the Glenns Ferry formation. Of the pyroclastic host sediment two samples (21-HG-023 and 21-HG-029) were collected from the southwest side of the maar and two more were collected from the southeast side of the maar (21-HG011- and 21-HG-037). Three sedimentary host samples were collected. Two from the southwestern side and one from the. All the host sediment samples were collected next to the dikes or as close to the dikes as possible.

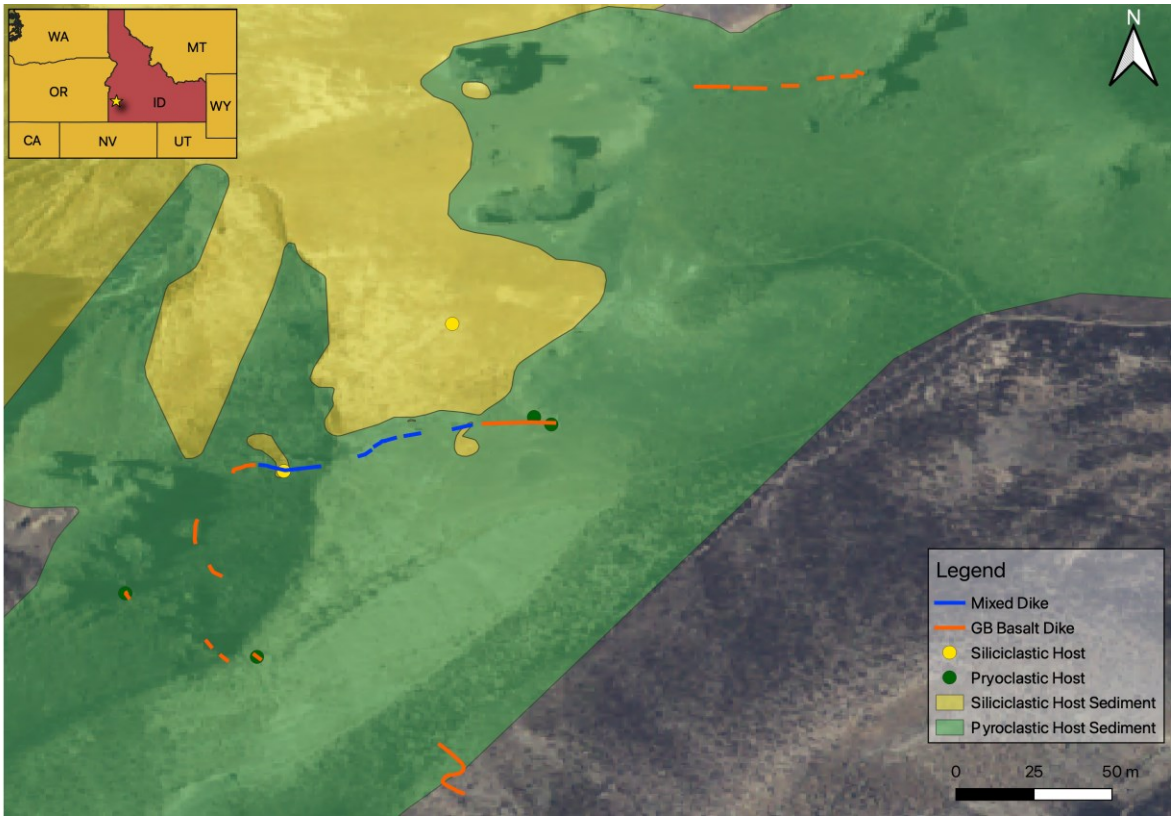

Figure 3. 2 map showing the locations for the pyroclastic (green) and siliciclastic (yellow) samples. Areas where the host types can be found are highlighted by polygons of the same color. GB basalt dikes are highlighted in orange and mixed dikes are highlighted in blue.

3.1.1.1 Pyroclastic Host Sediment

Pyroclastic deposits dominate Guffey Butte and include: heterolithic lapilli tuffs and tuffs (Figure 3.3). The deposits' color ranges from orange red to orange brown with lithics ranging in size from 0.5-13 cm. The pyroclastic deposits are predominantly matrix supported and dominated by sub-rounded basaltic juvenile lapilli. Sedimentary lithics make up ten percent of the pyroclastic deposits and range in size from 1 - 13 cm. Nonjuvenile frothy clasts of basalt with glass are also present (~5-15%) and range in shape from angular to rounded. These basalt clasts range in size from 0.54-2 cm. Pyroclastic material was predominantly found on the southwestern and eastern sides of the maar.

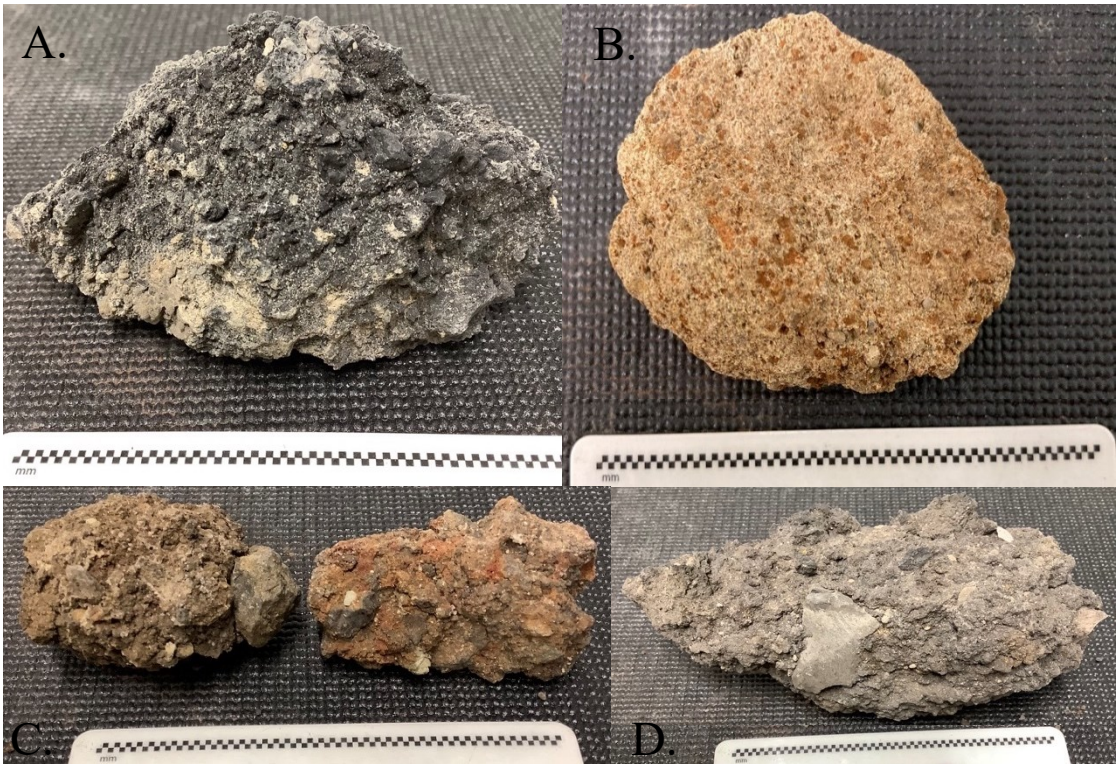

Figure 3. 3 Hand sample photos of all the pyroclastic samples collected. A) Scoria collected next to homogenized columnar joints, B) Lapilli tuff collected next to a mixed dike C) tuff breccia collected besides a GB basalt dike, and D) tuff breccia from northeaster side of maar. Increments on the scale in all photos are in mm. C and D are what the bulk of pyroclastic material at Guffey Butte.

Two thin sections were made of the pyroclastic host sediment and analyzed: lapilli tuff and scoria. Clasts in the pyroclastic deposit sample 21-HG-023 are made up of subhedral to euhedral plagioclase laths, anhedral to subhedral olivine, anhedral to subhedral clinopyroxene, and sporadic anhedral to subhedral quartz. Tachylyte composes a majority of the ground mass (80-85%) with sporadic sideromelane (10-15%) (Figure 3.4).

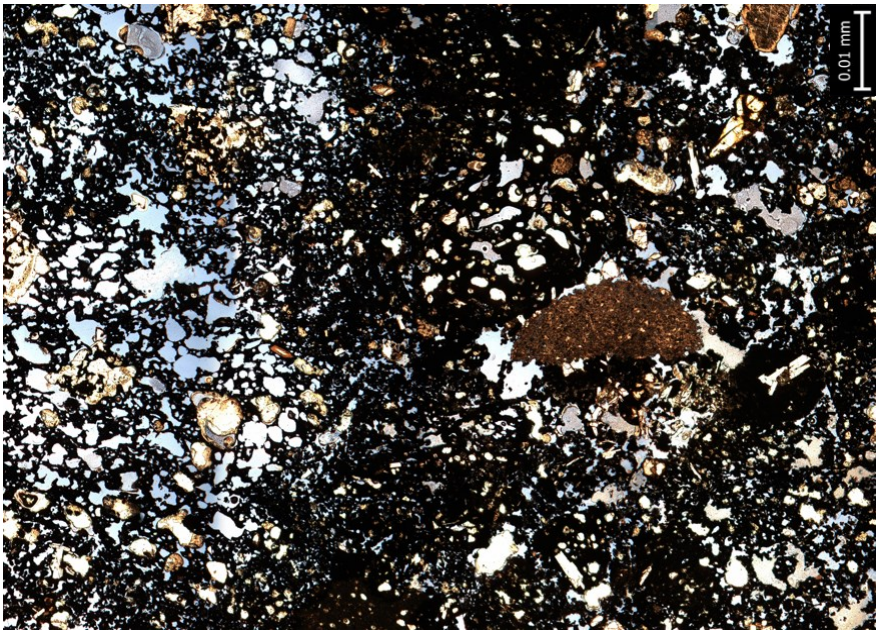

Figure 3. 4 Thin section photo, of sample 21-HG-023, showing the tachylyte dominant groundmass.

Quartz crystals are no larger than ~0.005 mm and are angular to sub-rounded. Oxides are present with in minerals and in the matrix of the samples. Vesicularity ranges from 30-35% and vesicles are subrounded to coalesced. It should be noted that partial alignment of vesicles is visible and that there is no phenocryst alignment. Non-igneous clasts consist of quartz, ranging from sub-angular to sub-rounded, and are no larger than 0.025 mm. Minerals identified in sample 21-HG-037 are similar to that of 12-HG-023 (Figure 3.5).

Point counts for both thin sections yielded N numbers listed in table 3.2. The quaintly of plagioclase (N =36) and quartz (N = 35) was noticeably much lower in 21-HG-023 than that of 21-HG-037 (N = 124 and N = 50) (Figure 3.6).

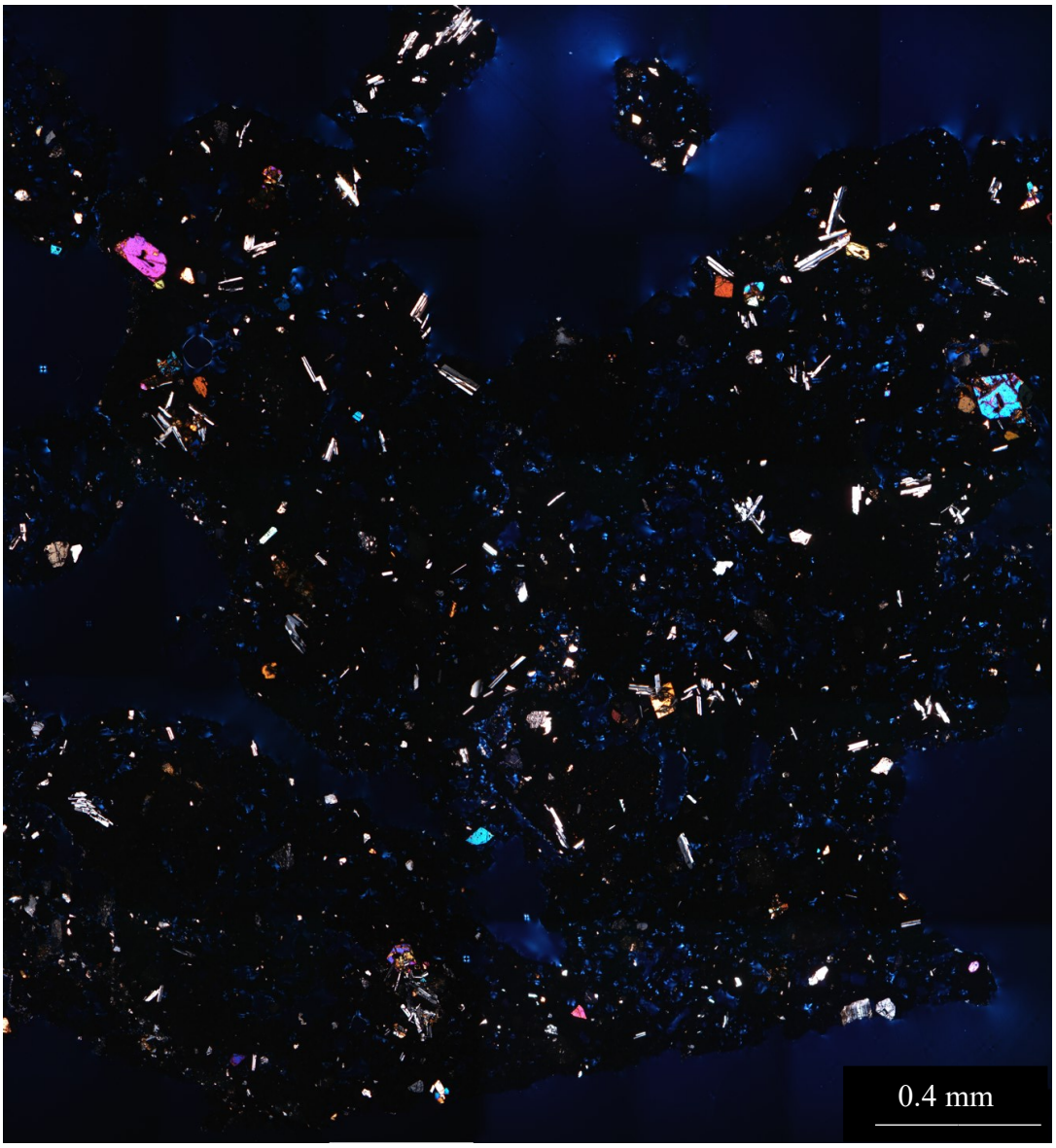

Figure 3. 5 Thin section mosaic, of sample 21-HG-037, showing the minerals anhedral to euhedral structure. This mosaic was taken in XPL at a magnification of 4x.

Pyroclastic Host				
Sample ID	Pl	Qtz	Rock Fragments	Other
21-HG-023	36	35	0	144
21-HG-037	124	50	0	42

Table 3. 2 Pyroclastic N counts from point count data.

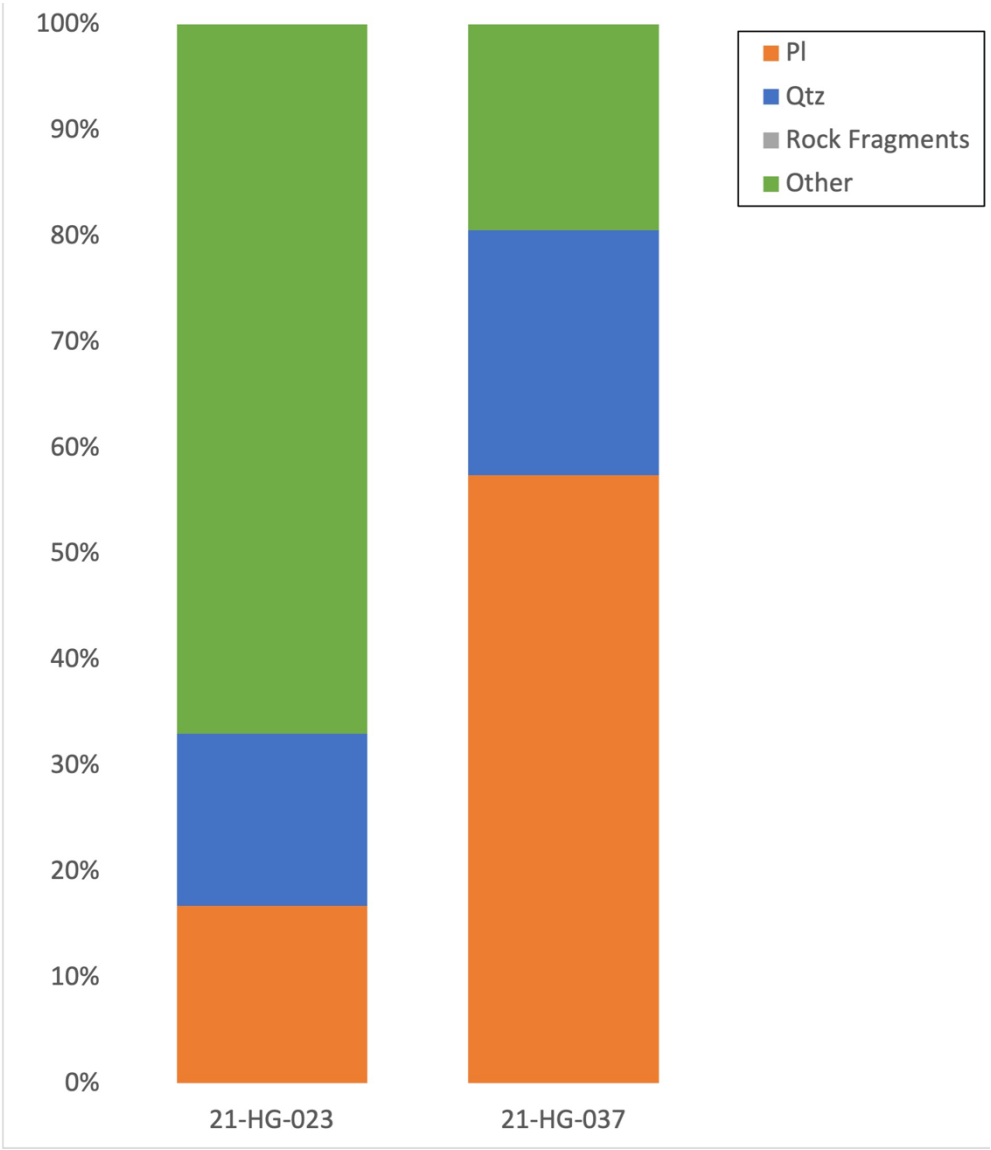

Figure 3. 6 Bar graph of pyroclastic samples N numbers calculated from point counts for the categories of plagioclase (orange), quartz (blue), rock fragments (gray), and other (green). The other category consists of the minerals: olivine, clinopyroxene, mica, oxides, and calcite.

3.1.1.2 Siliciclastic Host Sediment

The siliciclastic host sediment is part of the Glenns Ferry Formation that was deposited by Lake Idaho (Figure 1.5) and is comprised of unconsolidated silt and sandstone. The most abundant exposed siliciclastic units were Quartz Arenite (90% quartz with minor feldspar and rare micas) with a grain size of medium sand (0.0625-2 mm) and have no lithics of any kind visible (Figure 3.7a-b).

Figure 3. 7 Siliciclastic hand samples that are representative of siliciclastic host material. A) Sandstone sample 21-HG-035 B) Siltstone sample 21-HG-030

The siltstone was composed of fine, rounded grains, and were well sorted. Siliciclastic materials were delicate and weakly consolidated. In hand sample quartz, plagioclase, and the occasional mica are visible. Samples are comprised of 85-90% of quartz, 3-6% of plagioclase, and no more than 2% of mica. Siltstone, sample 21-HG-030, was found and collected on the Southwestern portion of the maar (Figure 3.2). Sample 21-HG-030 is a silt stone collected ~ 1m away from the dike. It is comprised of quartz (75-80%) and feldspar

(15%). Outcrops of siltstone were limited to deeper exposures that were proximal to the studied intrusions.

Sandstone, 21-HG-031 and 21-HG-035, is the dominant host sediment that is predominantly found on the northwestern to part of the northeaster portion of the maar and is comprised of quartz and feldspar. Sample 21-HG-031 was collected on the Southwestern portion of the maar next to the siltstone sample collected. Both sandstone samples collected are comprised of quartz 80-90%, 5-10% plagioclase, and no more than 3% of mafic minerals in hand sample. The quartz is predominantly subrounded with the occasional subangular grains. Plagioclase grains and the mafic minerals are subangular.

In thin section the sandstones are well sorted consisting of angular to rounded quartz, angular to subangular plagioclase, angular olivine, and angular clinopyroxene (Figure 3.8). They have no grading and are clast supported. Oxides are present within minerals ranging from a blocky to rounded shape. Only sample 21-HG-035 has long angular flakes of mica. Quartz is the dominant mineral comprising 40-85% of the sample, followed by plagioclase at 5-15%, olivine making up no more than 5%, and clinopyroxene making up no more than 3%. Mica composes no more than at most 2% in sample 21-HG-035. Siltstone sample (21-HG-030) is poorly sorted and consists of angular to subrounded quartz, angular plagioclase, angular olivine, and angular clinopyroxene (Figure 3.7b). It is ungraded and matrix supported. Quartz is the dominant mineral, composing 25-45%, plagioclase making up 5-10%, olivine making up no more than 3%, and clinopyroxene making up no more than 2%. Quartz in all siliciclastic sample thin section range from rounded to subangular and few have

fractures in them. Plagioclase crystals are not tabular and range in shape from subangular to subrounded.

Figure 3. 8 Thin section mosaic, of sample 21-HG-035, which shows minerals in the sandstone host sediment and their textures.

All three samples N numbers can be found in table 3.3 and graphed in figure 3.9. For plagioclase An# was calculated from EDS data. Plagioclase phenocrysts are predominantly andesine, An# ranging from 0.30-0.50, but all types of plagioclase were identified (Table 3.4 and Appendix). Quartz crystals were analyzed as a baseline to compare to the quartz in the mixing samples and have a normalized mass concentration of 31-63% O and 31-63% Si (Figure 3.10 and appendix).

Siliciclastic Host				
Sample ID	Pl	Qtz	Rock Fragments	Other
21-HG-030	20	294	0	4
21-HG-031	43	726	0	54
21-HG-035	27	839	0	36

Table 3. 3 Siliciclastic host N numbers calculated from point counts.

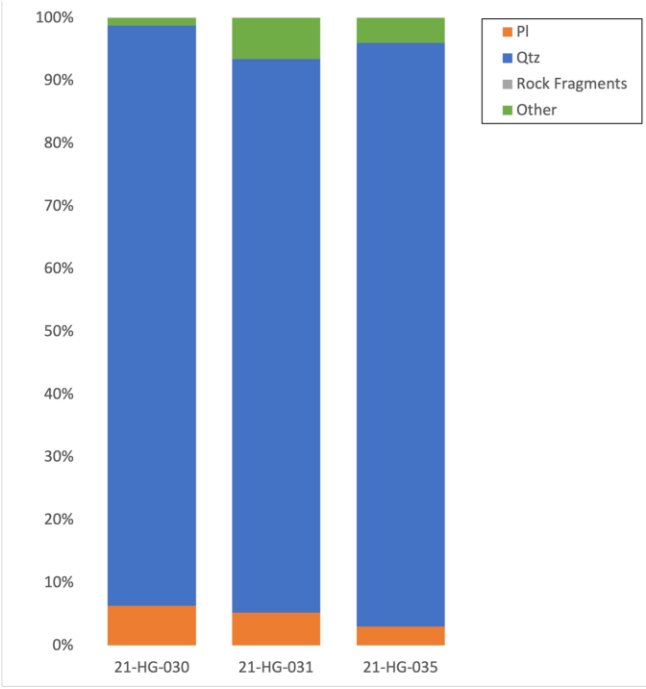

Figure 3. 9 Bar graph of siliciclastic samples N numbers calculated from point counts for the categories of plagioclase (orange), quartz (blue), rock fragments (gray), and other (green). The other category consists of the minerals: olivine, clinopyroxene, mica,

Siliciclastic An#							
Sample	Spectra	Ca	Na	K	An #	An %	Name
21-HG-030	4	6.55	6.60	0.27	0.49	48.81	Andesine
21-HG-030	5	4.33	4.55	0.37	0.47	46.81	Andesine
21-HG-030	6	4.99	3.51	0.38	0.56	56.19	Labradorite
21-HG-031	1	0.36	1.52	2.40	0.08	8.41	Albite
21-HG-031	2	1.74	4.39	0.16	0.28	27.66	Oligoclase
21-HG-031	1	5.39	5.27	1.72	0.44	43.54	Andesine
21-HG-031	2	5.68	5.22	1.66	0.45	45.24	Andesine
21-HG-031	5	10.63	3.47	0.21	0.74	74.28	Bytownite
21-HG-031	6	11.65	2.91	0.16	0.79	79.14	Bytownite
21-HG-035	1	5.20	4.02	2.71	0.44	43.59	Andesine
21-HG-035	2	1.43	3.10	5.98	0.14	13.61	Oligoclase
21-HG-035	3	6.48	4.31	1.59	0.52	52.34	Labradorite
21-HG-035	4	1.24	2.90	6.05	0.12	12.17	Oligoclase
21-HG-035	5	1.04	2.70	6.69	0.10	9.97	Albite

Table 3. 4 An#'s and An%'s of plagioclases in the all three siliciclastic samples collected.

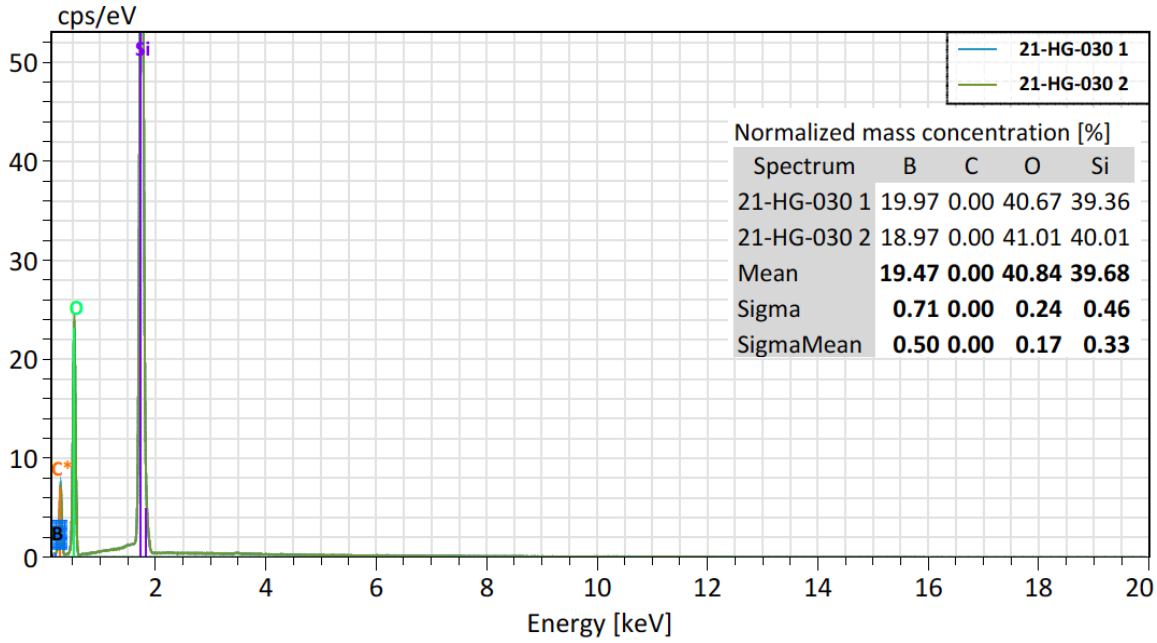

Figure 3. 10 Elemental spectra 1 and 2 of quartz in siltstone sample 21-HG-030.

3.1.2 Basalt

There is about 221 m of exposed intrusions at Guffey Butte of which ~128 m is comprised of GB basalt and are at depths ranging from 94-128 m (Figure 3.11). The basaltic dikes crosscut the host sediments and the contact between the pyroclastic host sediments and the dikes are not consistent. The dikes have variable trends ranging from 84-231 and plunges ranging from 30-69.

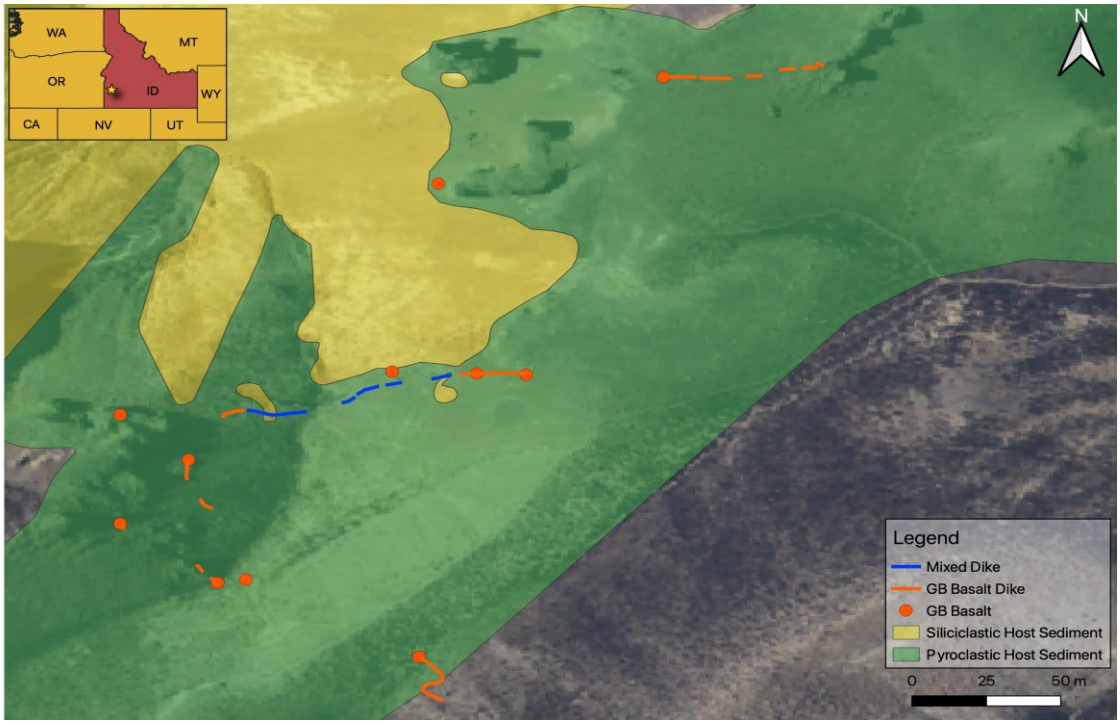

Figure 3. 11 Map of GB basalt samples collected around the maar to capture the range of basalt present. GB basalt dikes are highlighted in orange and mixed dikes are highlighted in blue.

Basaltic dikes are contaminated with lithics ranging from 2-20%, both basaltic and siliciclastic rock fragments, ranging in size from 0.5-11 cm (Figure 3.12a-d). Both lithic types range from cognate to accidental (Dickinson, 1970). Cognate lithics were made up of fragments of juvenile non-vesiculated basalts that are dense and angular. Accidental lithics are picked up by flows or surges and are subangular to subrounded (Dickinson, 1907;

Affolter and Ingersoll, 2019; and Allabay, 2008). From this point forward all basalts will be referred to as GB basalt(s).

Figure 3. 12 Hand samples of GB basalt showing the range of basalt at Guffey Butte. Image A shows the cleanest basalt and C shows the basalt with the most contamination (~20%). Image B has the basalt annotated in orange. Image D has the siliciclastic lithics in yellow and basalt lithics in orange. The scale in all four images is in mm.

There are two types of dikes present at Guffey Butte: tabular and billowed (Figure 3.13a-b). The GB basaltic dikes are generally tabular and characterized by their approximately linear morphology with local variations in the margins. Their thicknesses range from 20-170 cm and their preserved margins range 0.5-2.5 cm (Figure 3.14a-b). The margins are dense and less vesicular in comparison to the center of the dikes which were

more vesicular (25-38%). However, several of these dikes have dense interiors and little to no vesicles (10-0%) which made them difficult to sample. There is one billowed dike characterized by repetitive undulatory and curved margins. It is ~ 2 m wide and has no quenched margins and the billows are only present on the eastern facing section of the dike. In several of the dikes, elongated vesicles were visible and showed partial preferential directionality subparallel to parallel in relation to the preserved margin (Figure 3.14b). A total of fourteen GB basalt samples were taken from exposed dikes (Table 3.1).

Figure 3. 13 Field photos that show the two types of dikes and their orientations. A) Tabular dike that changes orientation B) Billowed dike. Billows are highlighted by the red circles.

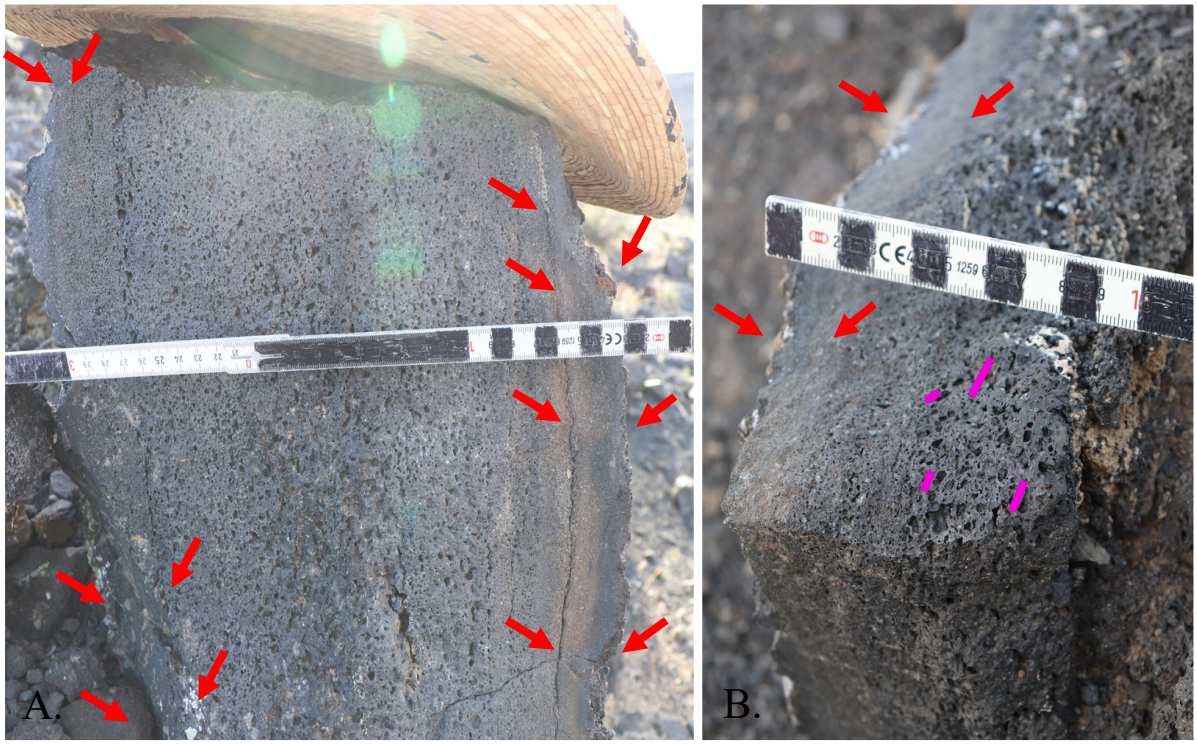

Figure 3. 14 A & B) Field photos of the interiors of GB basalt dikes that demonstrate the preservation of the dike margins (red arrows). B) Shows vesicle elongation subparallel to parallel to dikes preserved margin highlighted by the pink lines.

All fifteen collected samples of GB basalt had thin sections made and analyzed. All samples are porphyritic containing phenocrysts of subhedral to euhedral plagioclase laths, subhedral to euhedral olivine, subhedral to euhedral clinopyroxene, and anhedral quartz (Figure 3.15a-c) in a tachylyte groundmass. Some samples contain microlites of plagioclase that have a pilotaxitic texture (Figure 3.16a). Plagioclase feldspar are the dominant mineral, composing 10-80%, quartz makes up 5-8%, olivine follows at 2-5%, and clinopyroxene composes no more than 5%. Blocky to rounded oxides were observed in minerals and compose no more than 3%. Glomerocrysts were observed in samples which exhibits heavy microlitic textures (Figure 3.15c). Vesicularity ranges between 0-35% as some vesicles had coalesced. Tachylyte makes up the ground mass of all GB basalt samples and is partially visible in samples that exhibit a microlitic texture as the plagioclase crystals are small and clump together. Quartz found in GB basalts are low in abundance and are likely derived from the unconsolidated sediment.

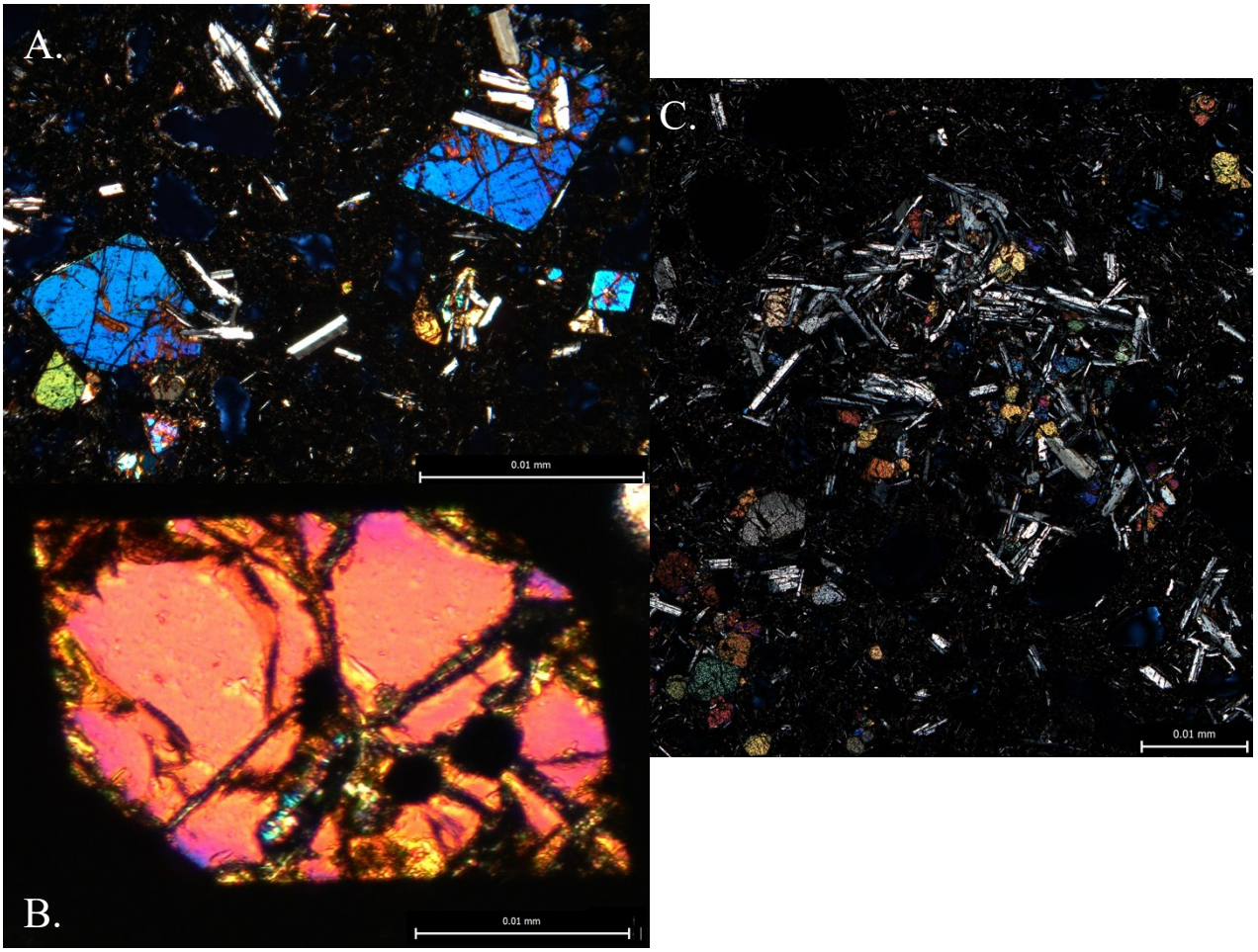

Figure 3. 14 Cross polarized images showing the subhedral to euhedral shapes of minerals found in GB basalts. A) Subhedral to euhedral clinopyroxene and plagioclase, B) Euhedral olivine with subhedral oxides, C) Glomerocryst of plagioclase and clinopyroxene.

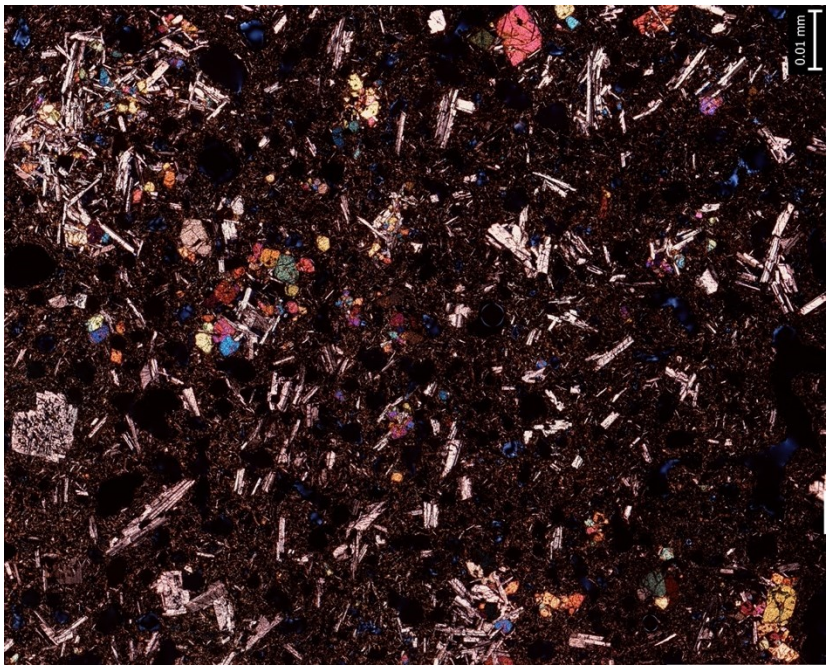

Figure 3. 16 Thin section photo, of 21-HG-002, showing the microlites of plagioclase with a pilotaxitic texture, vesicle shape, plagioclase with a sieve texture, and euhedral olivine and clinopyroxene crystals.

Point counts for all fifteen thin sections yielded N numbers listed in table 3.5. The percentage of other minerals varies greatly from 1-73%. Plagioclase remains the most dominant mineral with an average of 55% followed by quartz at 28% (Figure 3.17). An# was calculated, from EDS data (Table 3.6). Plagioclase phenocrysts were predominantly bytownite and ranged down to Albite. Quartz crystals which were the least fractured and the most subhedral were analyzed yielding normalized mass concentration percentages of 49% O and 50% Si (Figure 3.18).

GB Basalt				
Sample ID	Pl	Qtz	Rock Fragments	Other
21-HG-005	356	20	0	15
21-HG-013	207	146	8	12
21-HG-003	231	153	2	9
21-HG-004	211	105	2	27
21-HG-020	193	146	8	31
21-HG-019	33	7	0	81
21-HG-021	410	32	0	155
21-HG-022	370	32	0	240
21-HG-028	137	102	0	26
21-HG-027	317	3	0	81
21-HG-036	262	28	1	57
21-HG-034	238	72	0	53
21-HG-001	532	0	0	99
21-HG-002	425	2	0	83

Table 3. 5 GB basalt N numbers calculated from points counts categorized into: plagiolcase (orange), quartz (blue), rock fragments (gray), and other (green)

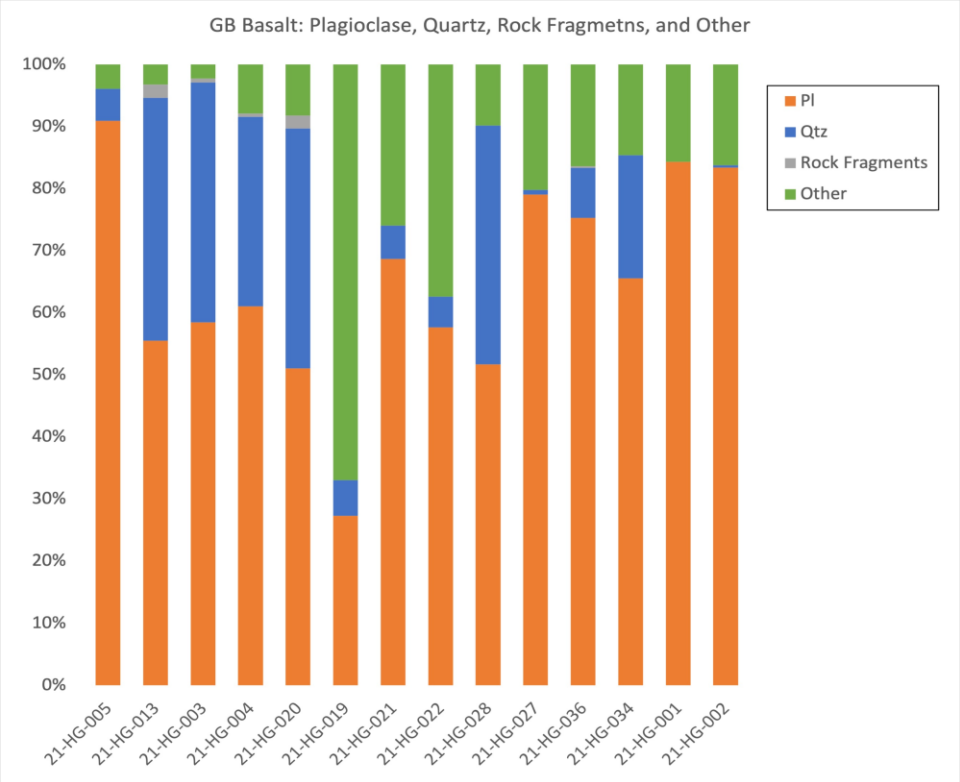

Figure 3. 17 Bar graph of GB basalt N numbers calculated from point counts then separated into the categories of plagioclase (orange), quartz (blue), rock fragments (gray), and other (green). The other category consists of the minerals: olivine, clinopyroxene, mica, oxides, and calcite. Samples are ordered based off their radial distance from the nearest mixed dike.

GB Basalt An#							
Sample	Spectra	Ca	Na	K	An #	An %	Name
21-HG-004	1	4.73	3.61	2.56	0.43	43.39	Andesine
21-HG-004	2	3.85	3.64	3.45	0.35	35.19	Andesine
21-HG-004	3	13.39	2.18	0.15	0.85	85.18	Bytownite
21-HG-004	4	13.42	2.09	0.16	0.86	85.64	Bytownite
21-HG-004	5	7.97	4.57	1.25	0.58	57.80	Labradorite
21-HG-004	6	7.03	4.12	1.25	0.57	56.69	Labradorite
21-HG-004	7	8.31	1.91	0.35	0.79	78.62	Bytownite
21-HG-004	8	8.27	1.80	0.34	0.79	79.44	Bytownite
21-HG-004	9	6.84	1.94	0.43	0.74	74.27	Bytownite
21-HG-004	10	9.44	1.77	0.78	0.79	78.73	Bytownite
21-HG-004	11	1.90	0.62	0.99	0.54	54.13	Labradorite
21-HG-004	12	6.68	1.92	0.40	0.74	74.22	Bytownite
21-HG-004	1	5.35	5.63	1.10	0.44	44.29	Andesine
21-HG-004	2	4.74	5.93	1.18	0.40	40.00	Andesine
21-HG-004	3	13.39	2.18	0.15	0.85	85.18	Bytownite
21-HG-004	4	13.42	2.09	0.16	0.86	85.64	Bytownite
21-HG-004	7	5.33	3.79	2.28	0.47	46.75	Andesine
21-HG-004	10	8.36	1.98	0.34	0.78	78.28	Bytownite
21-HG-004	1	9.39	2.04	0.42	0.79	79.24	Bytownite
21-HG-004	2	8.01	1.99	0.45	0.77	76.65	Bytownite
21-HG-004	3	12.01	2.61	0.25	0.81	80.77	Bytownite
21-HG-004	4	12.78	2.22	0.25	0.84	83.80	Bytownite
21-HG-013	4	4.27	3.28	2.09	0.44	44.29	Andesine
21-HG-013	1	11.99	2.21	0.09	0.84	83.90	Bytownite
21-HG-013	2	11.70	2.39	0.12	0.82	82.34	Bytownite
21-HG-013	3	11.91	2.33	0.13	0.83	82.88	Bytownite
21-HG-013	4	12.36	2.16	0.15	0.84	84.25	Bytownite
21-HG-013	5	11.77	2.35	0.18	0.82	82.31	Bytownite
21-HG-013	2	0.69	1.30	6.09	0.09	8.54	Albite
21-HG-013	3	8.41	3.35	0.60	0.68	68.04	Labradorite
21-HG-013	4	8.15	2.92	0.81	0.69	68.60	Labradorite

Table 3. 6 GB basalt An#'s from plagioclase minerals analyzed.

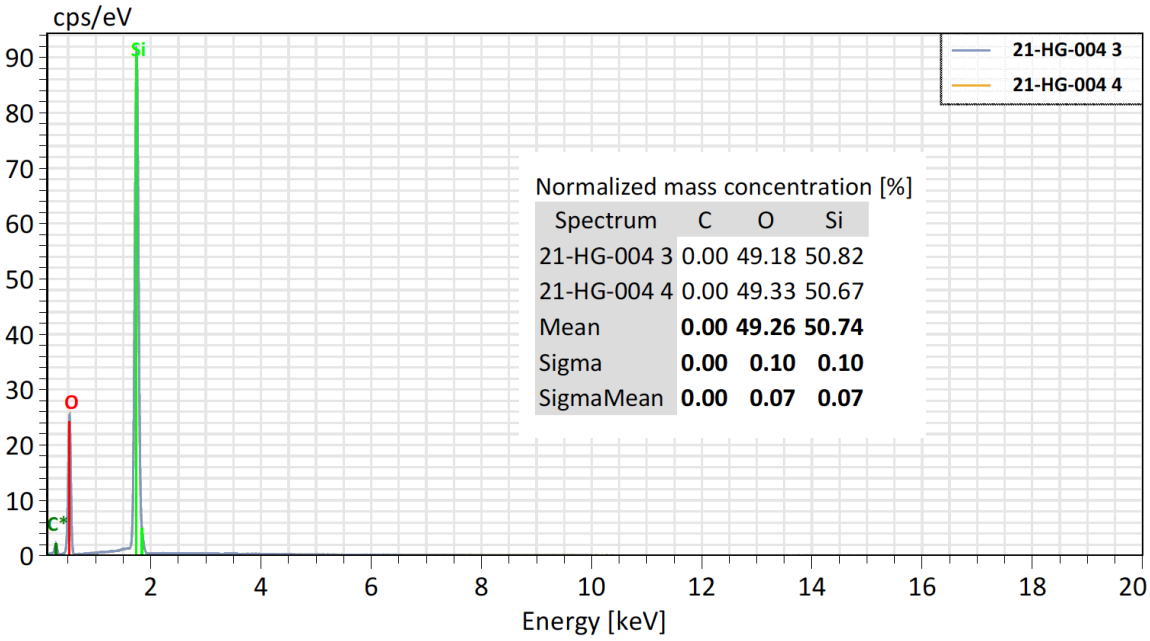

Figure 3. 18 Elemental spectra 3 and 4 of quarts in GB basalt sample 21-HG-004.

3.1.3 Mixing

Of the ~221 m of exposed dike at Guffey Butte ~93 m is comprised of a range of mixing between GB basalt and siliciclastic material (Figure 3.19). The intensity of mingling is diverse, and the variations in the style of mingling over a spatial area is not systematic. The transition between the basaltic dike sections and the mingled dikes are not well constrained as they gradationally change into each other. There is no patern as to what syle of mingling grades into eachother making mixing variable.

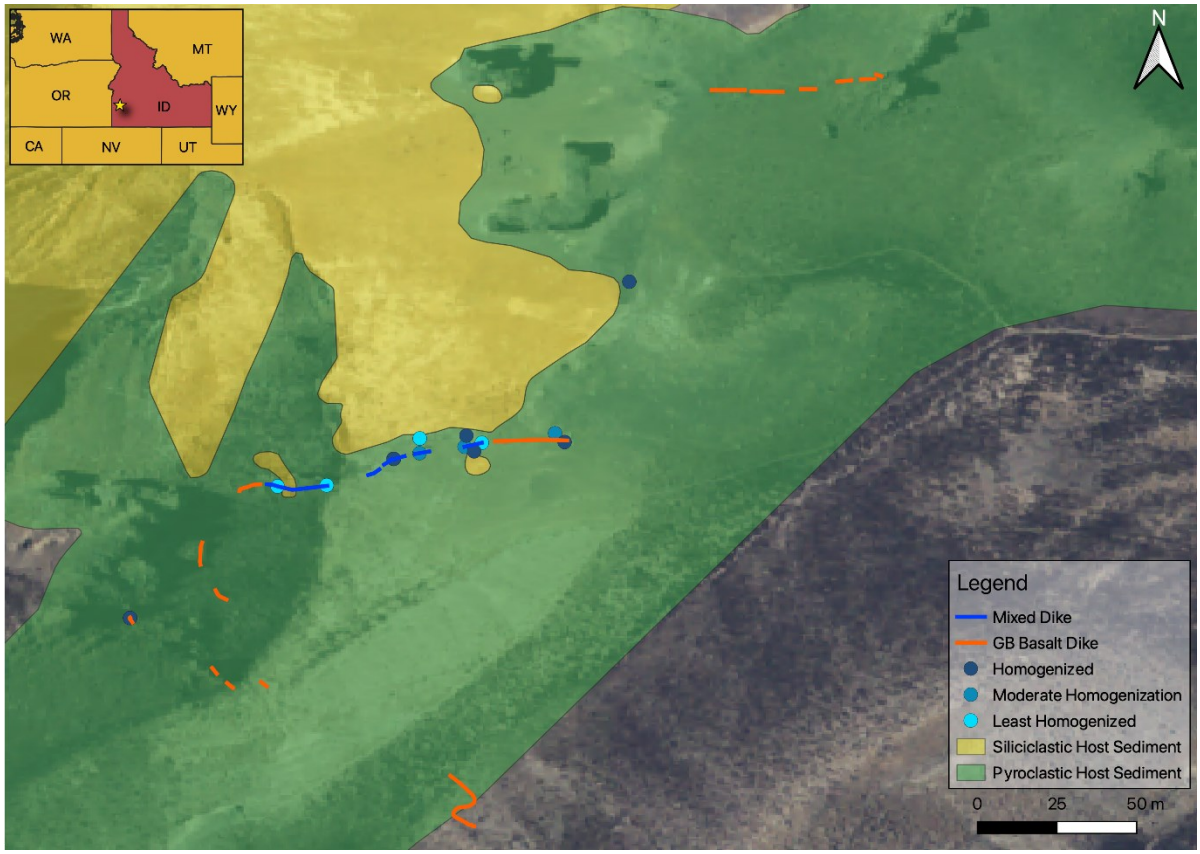

Figure 3. 19 Map showing the locations where all the mixed samples were collected.

At times contacts between the dikes and the surrounding host sediment were sharp while others were transitional and hard to identify. Local sections (up to 25 m long) appeared highly homogenous, where GB basaltic and sedimentary material were not visually distinguishable. Transitional zoning between the interaction of magma and mixing was visible in the field (Figure 3.20). Within several centimeters the type (GB basalt and siliciclastic fragments), concentration (up to 85%), and size (0.5-10 cm) of the lithics within the dikes change (Figure 3.21).

Figure 3. 20 Field photo showing the transitional zoning. A) Un annotated field photo with a scale bar in the top left-hand corner. B) GB basalt, highlighted in orange, surrounding the mixing from left to right. A transition zone between the GB basalt and the mixing columnar joint, show in dark blue, is represented by the dashed light blue lines

Figure 3. 21 Field photo of the north side of the dike which is eroded allowing for the interior of the dike to be exposed. A change in lithic size and concentration is visible over ~2 ft. The transitional zoning between mixing types is also visible.

The dikes are tabular and their thicknesses range from 20-170 cm (Figure 3.22a). The margins of mixing dikes were preserved only on the southern side and exhibit a texture similar to columnar joints on the southern side (Figure 3.22 a-b). The margins on the northern side were eroded which allowed for the interior of the mixed dike to be visible. In several of the mixed dikes elongated vesicles were visible with preferential vesicle alignment subparallel to parallel of the preserved margins (Figure 3.23). Vesicle elongation was also documented subparallel to parallel the bands and swirls of the mixing GB basalt and siliciclastic sediment. Mixing has been separated into three categories: least homogenized, moderate homogenization, and homogenized based on field and petrographic observations (Figure 3.24a-c).

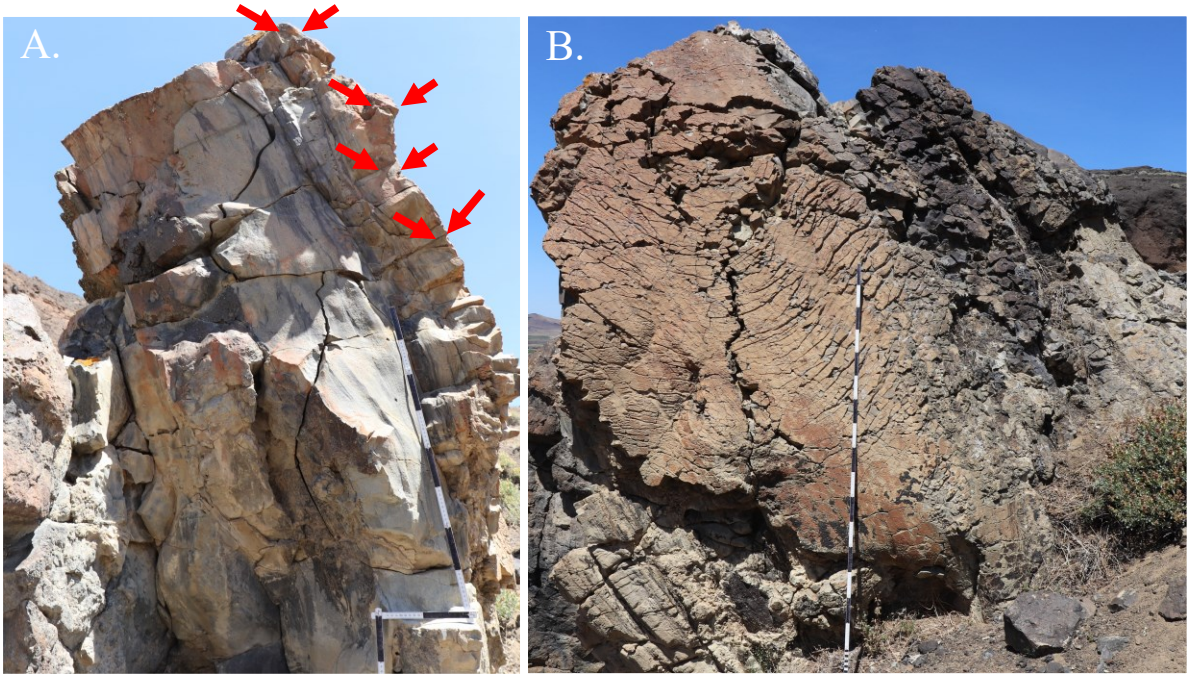

Figure 3. 22 Field photos showing the thickness and preserved margin of the mixed dikes. A) Shows the thickness of the mixed dike. The red arrows point to the preserved margin on the south side of the mixed dike. B) The columnar joint texture in the margin of the mixed dike composed of mixing.

Figure 3. 23 Field photo taken from the northern side of the mixed dike that shows the interior, Elongated vesicles subparallel to parallel are visible and highlighted in pink.

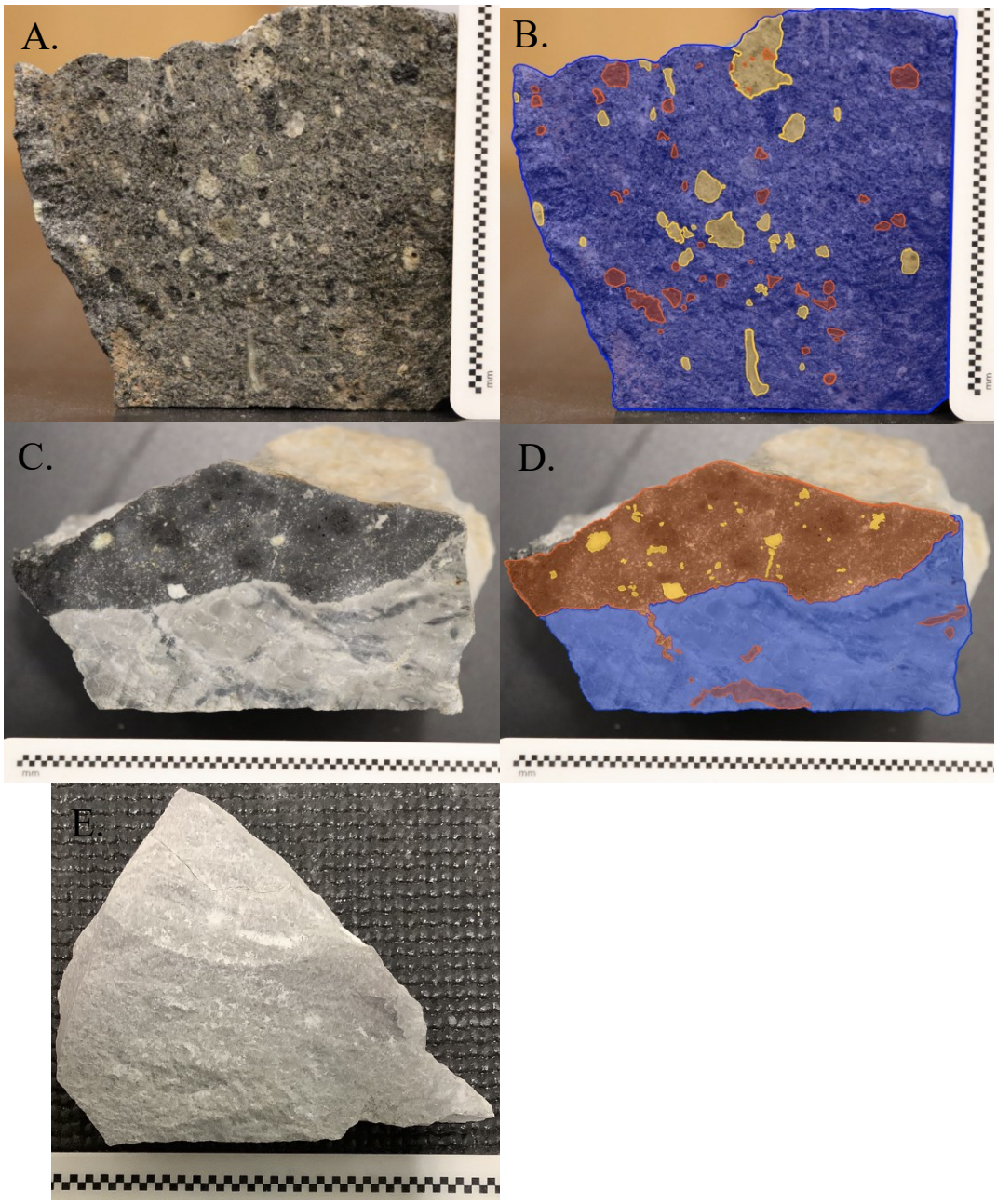

Figure 3. 24 Hand samples of the three mixing categories. A) Least homogenized sample 21-HG-018, B) Annotated version of A. GB basalt shows in orange, siliciclastic material shown in yellow, and mixing shown in blue, C) Moderately homogenized sample 21-HG-007. Ribbons of basalt are visible in the lower half of the sample and a small area where GB basalt is being injected to the mixing, D) Annotated version of C. Annotation color scheme is the same as in B, E) Homogenized sample 21-HG-016. It is hard to identify whether GB basalt or siliciclastic sediments is the most dominant.

3.1.4 Least Homogenized

Parts of the dike that are least homogenized are sections in which basaltic and siliciclastic material is easily distinguishable by eye (Figure 3.24a). Lithics consist of fragments of GB basalt and siliciclastic rock ranging in size from less than 0.5-11 cm, from angular to rounded, and composed 5-90% of the dike. Individual minerals can be seen GB basalt lithics (~2 mm at most). There is no grading of lithics as the larger lithics are locally scattered and at other locations gather in a singular location (Figure 3.24a and 3.21).

Locally elongated vesicles have preferred orientations aligned with the fragments in the rock surrounding it. Vesicles are rare in the matrix, composed of not more than 10%, and are visible in several of the GB basaltic lithics. Vesicles are also present in the GB basalt lithics composing no more than 4% of the lithic. The matrix is a combination of GB basalt and siliciclastic host but have higher quantities of either host. If the matrix is siliciclastic host, it is possible to distinguish whether it is sand or silt stone, if the siliciclastic host is not clearly visible nearby (Figure 3.25a-b). Five of the collected mixed samples fall into this category (Table 3.1).

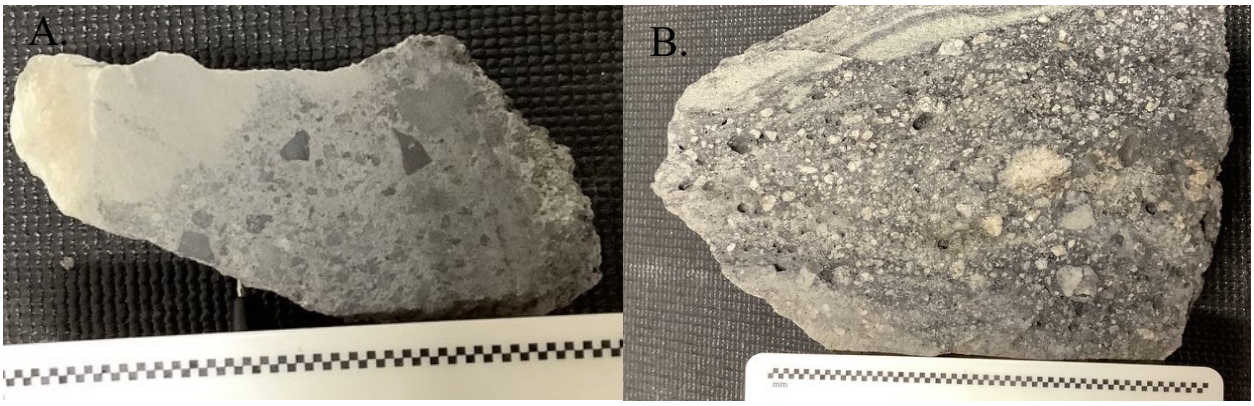

Figure 3. 25 Hand sample photos that illustrates the difference in mixing between the sandstone (B) and siltstone (A). The scale in both A and B are in mm.

Thin sections were made of all five least homogenized samples which contain anhedral to euhedral plagioclase, anhedral to subhedral clinopyroxene, anhedral to subhedral olivine, and anhedral to subhedral quartz. Crystals are suspended in a tachylyte matrix. There were little to no vesicles visible (0-10%) and if present had the beginnings of vesicle fill. Quartz is the dominant mineral, comprising 30-55%, plagioclase made up 5-20%, olivine composed no more than 3%, clinopyroxene comprised no more than 2%, and lithics made up no more than 1%. Oxides were also present both in the matrix and within minerals (>5%). Quartz crystals were fractured, range from angular to subrounded, and range in size up to no more than 1 mm. Some quartz crystals were coalesced with each other and were no more than 2 mm (Figure 3.26).

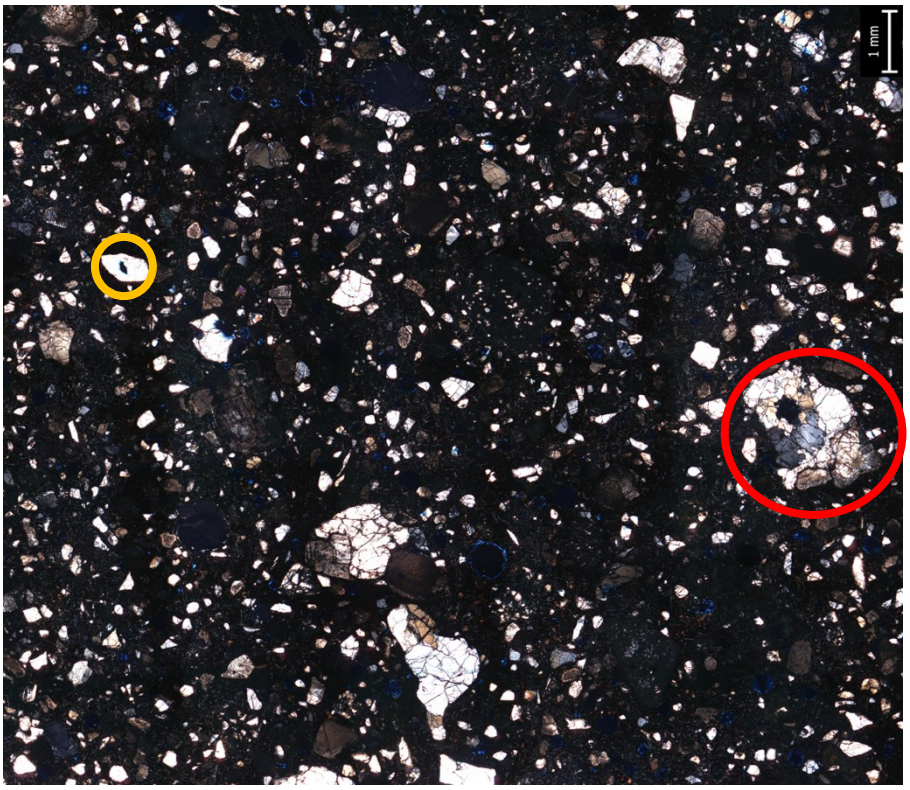

Figure 3. 26 Photomicrograph, of 21-HG-017, that shows range of minerals identified in in least homogenized samples. Coalesced quartz is circled in red and individual quartz crystals are circled in

Point counts for all thin sections yielded N numbers listed in table 3.7. It should be noted that the N numbers will vary based on the size of the minerals and the area selected in the thin section (Figure 3.27). Samples like 21-HG-006 had sections which consisted of mineral grains too small to identify which may skew the data. An# was calculated from EDS data. Plagioclase phenocrysts were predominantly bytownite, An# ranging from 0.70-0.90, followed by andesine with an An# ranging from 0.30-0.50, labradorite with An# ranging from 0.50-0.70, and albite ranging from 0-0.10 (Table 3.8). Plagioclase crystals thought to have been altered are k-feldspar with rims of plagioclase (Figure 3.29). The quartz crystals analyzed yielded normalized mass concentration percentages of 50% O and 49% Si (Figure 3.30). Spectra collected to identify the groundmass show that it is tachylyte (Figure 3.31).

Least Homogenized				
Sample ID	Pl	Qtz	Rock Fragments	Other
21-HG-006	49	190	1	27
21-HG-018	20	291	1	23
21-HG-012	37	359	0	8
21-HG-014	199	406	0	13
21-HG-017	3	173	0	30

Table 3. 7 Least homogenized N numbers calculated from point count data.

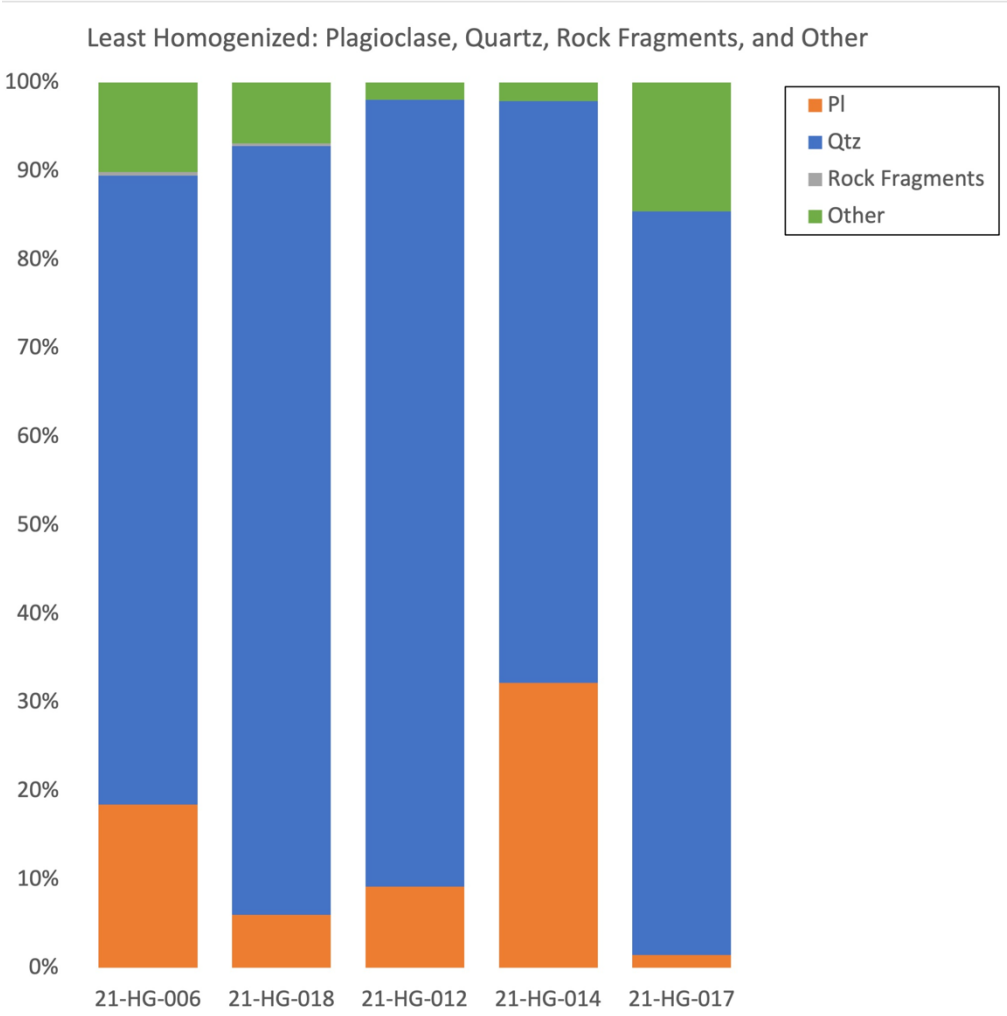

Figure 3. 27 Bar graph of GB basalt N numbers calculated from point counts then separated into the categories of plagioclase (orange), quartz (blue), rock fragments (gray), and other (green). The other category consists of the minerals: olivine, clinopyroxene, mica, oxides, and calcite. Samples are ordered based off their radial distance from the nearest mixed dike.

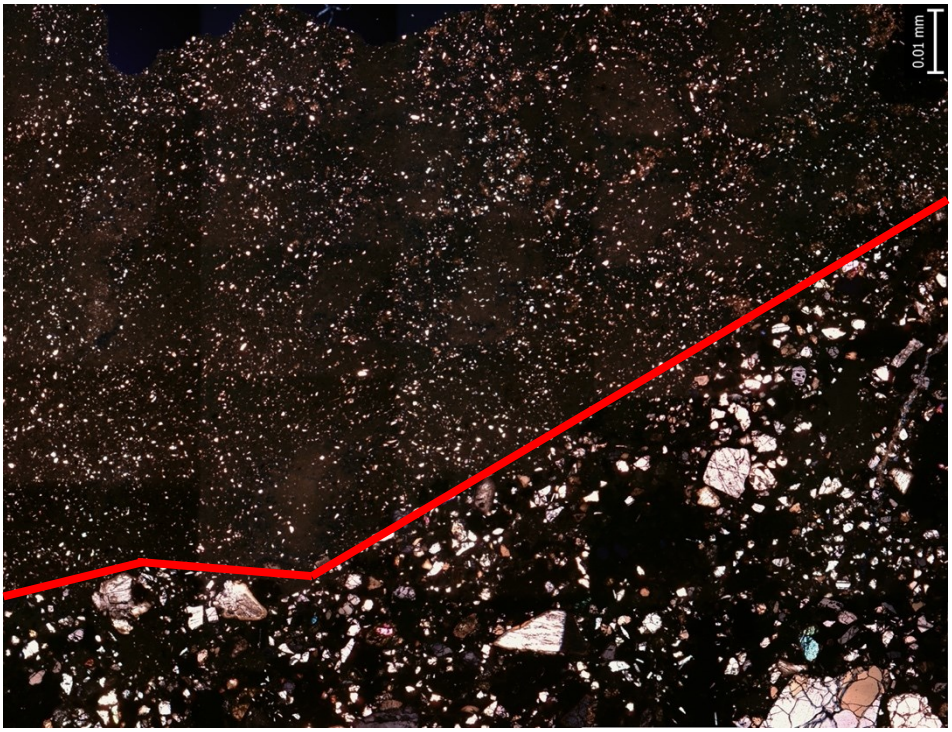

Figure 3. 28 Photomicrograph, of 21-HG-006, with a red line separating the portions too small to use for point counts. Any minerals above the red line could not be used as they are too small to identify properly.

Least Homonized An#							
Sample	Spectra	Ca	Na	K	An #	An %	Name
21-HG-012	1	10.73	2.27	0.37	0.80	80.25	Bytownite
21-HG-012	2	10.61	2.25	0.42	0.80	79.89	Bytownite
21-HG-012	3	10.43	2.17	0.38	0.80	80.35	Bytownite
21-HG-017	3	8.30	3.77	0.99	0.64	63.55	Labradorite
21-HG-017	4	6.19	2.76	1.77	0.58	57.74	Labradorite
21-HG-017	1	0.84	2.55	8.49	0.07	7.07	Albite
21-HG-017	2	0.85	2.56	8.50	0.07	7.14	Albite
21-HG-017	3	4.07	3.04	3.81	0.37	37.27	Andesine
21-HG-017	4	5.49	3.53	2.80	0.46	46.45	Andesine

Table 3. 8 An#, An%, and name based on An percentage for plagioclase found in least homogenized samples.

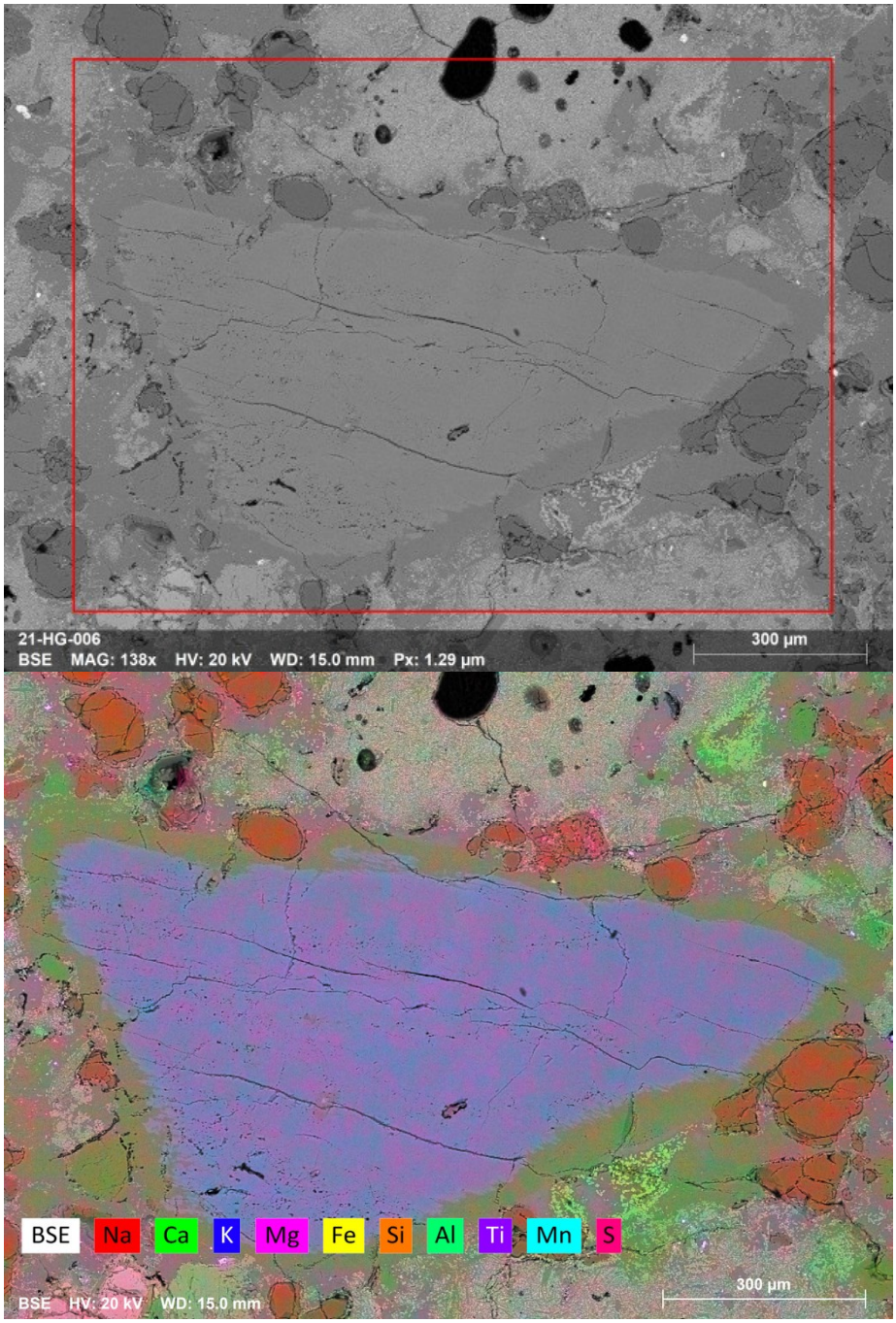

Figure 3. 29 Qmap of k-feldspar with a plagioclase rim. A) BSE image with the analysis area shown by the red box. B) Qmap of the area in the red box. The core is made up of K and Al. The rim is made up of Ca and Na.

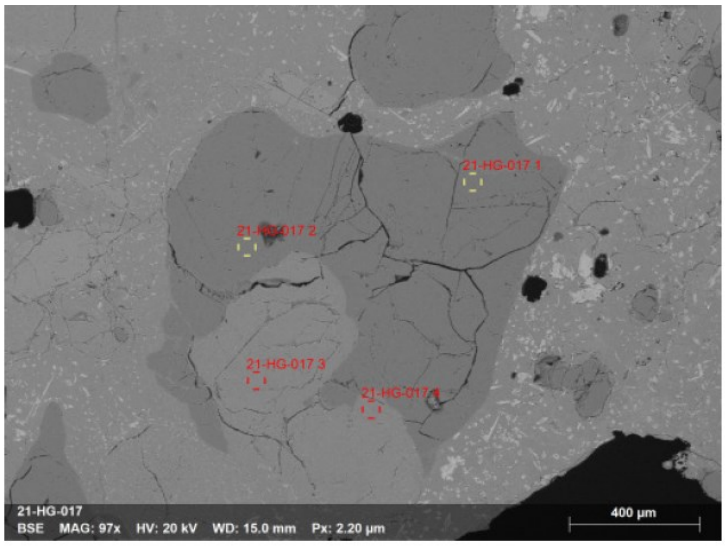

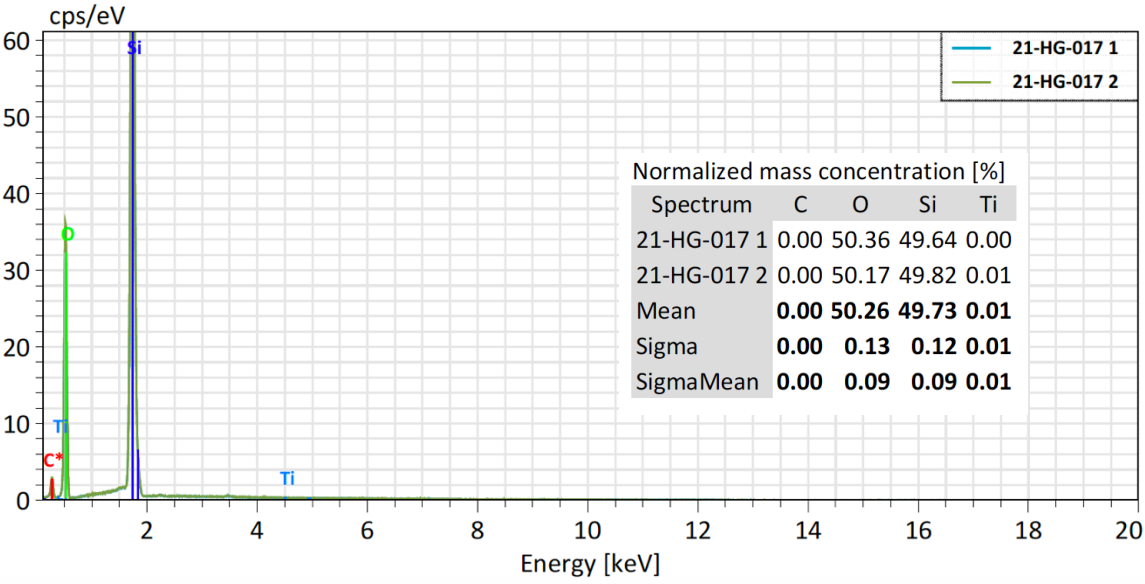

Figure 3. 30 BSE image highlighting elemental spectra 1 and 2 (quartz crystal).

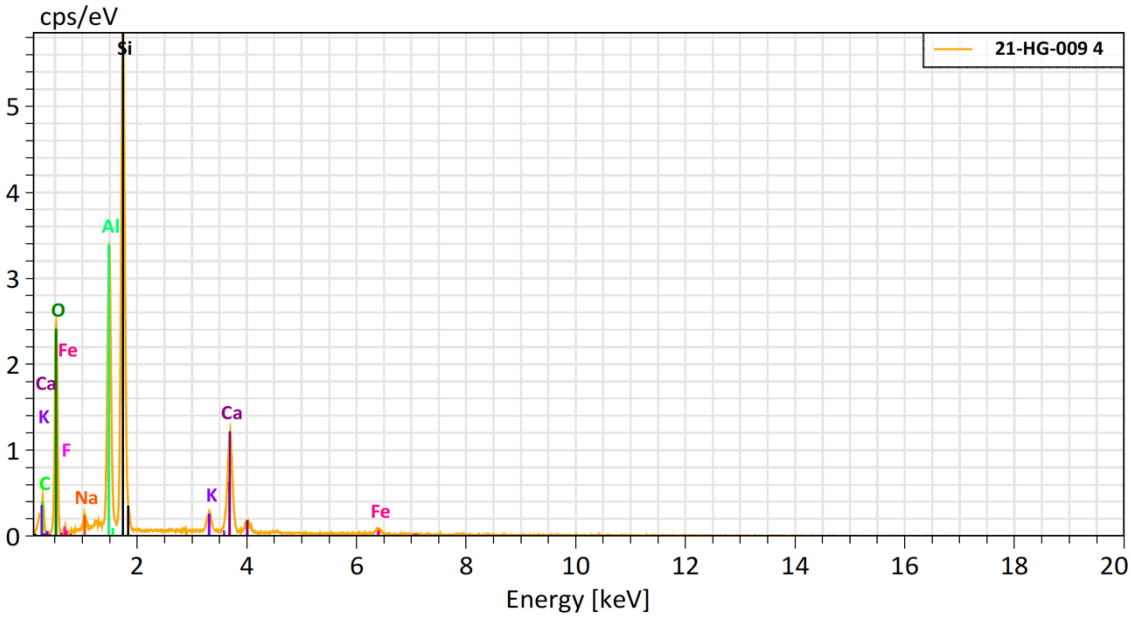

Figure 3. 31 BSE image highlighting elemental spectra 4 (tachylyte).

3.1.4 Moderate Homogenization

Moderate homogenization contains little to no lithics (>5%) and it is still partially possible to identify basaltic and siliciclastic material from each other. Lithics come from GB basalt and siliciclastic rock. In the field multiple different types of mingling textures were observed (Figure 3.32). Unlike the least homogenized rocks, moderately homogenized rocks have banding of alternating GB basalt and siliciclastic material in the form of waves, ribbons, bands, and swirls. Moderately homogenized rocks are harder and denser in comparison to least homogenized rocks which made sampling difficult. When sampled the faces of resembled that of a quartzite as the rock is well cemented.

Vesicularity of the dike ranged from 0-15% and ranged from angular to rounded. Elongated vesicles are also observed subparallel to parallel to the banding or swirling. In hand sample vesicles range from subangular to rounded. Some vesicles are elongated and are parallel to or in the bands or ribbons of basalt. GB basalt lithics in these samples have no visible vesicles and are the least predominant lithic. Siliciclastic lithics are the most predominant and are subangular to sub rounded. Large quartz crystals are visible and varied in size <1 mm. The mixed dikes that are moderately homogenized rocks are found in propagated through pyroclastic and siliciclastic host sediment. Moderately homogenized zones also transition into least homogenized and homogenized zones. Of the samples collected four samples fall with in this category (Figure 3.33 and Table 3.1).

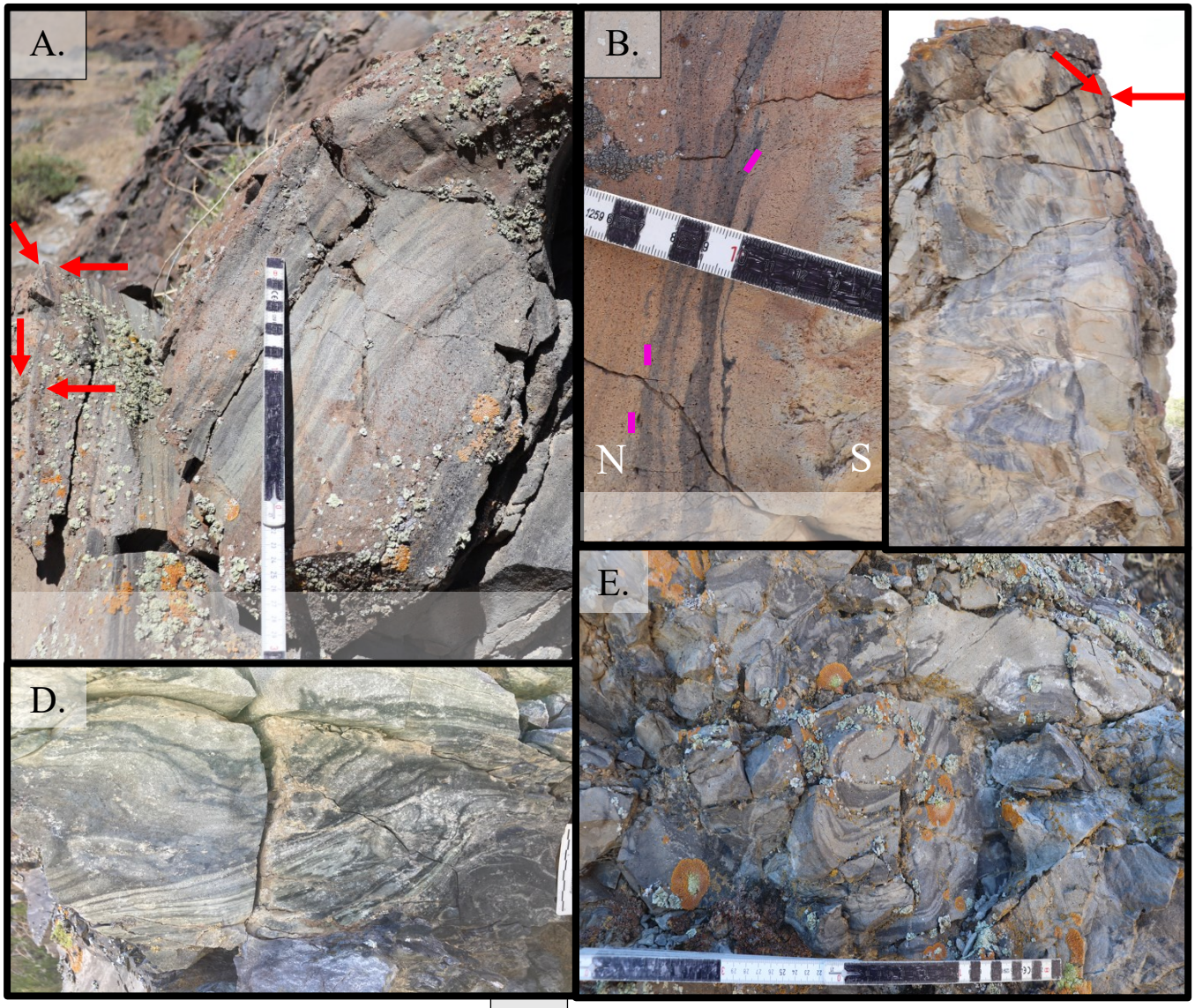

Figure 3. 32 Textures found in moderate mixing in the field. A) Banding textures are parallel to the preserved margin on the southern portion of the dike. The red arrows point to the margin. B) Banding and the beginning of waves parallel to the preserved margin. Elongated vesicles are visible subparallel to parallel to the banding, waves, and margin (pink lines). C) The wavy texture is best seen at the bottom of the interior of the dike running parallel to the preserved margin. The red arrows point to the preserved margin. D) A mix between banding, waves, and the swirling. E) Swirling texture.

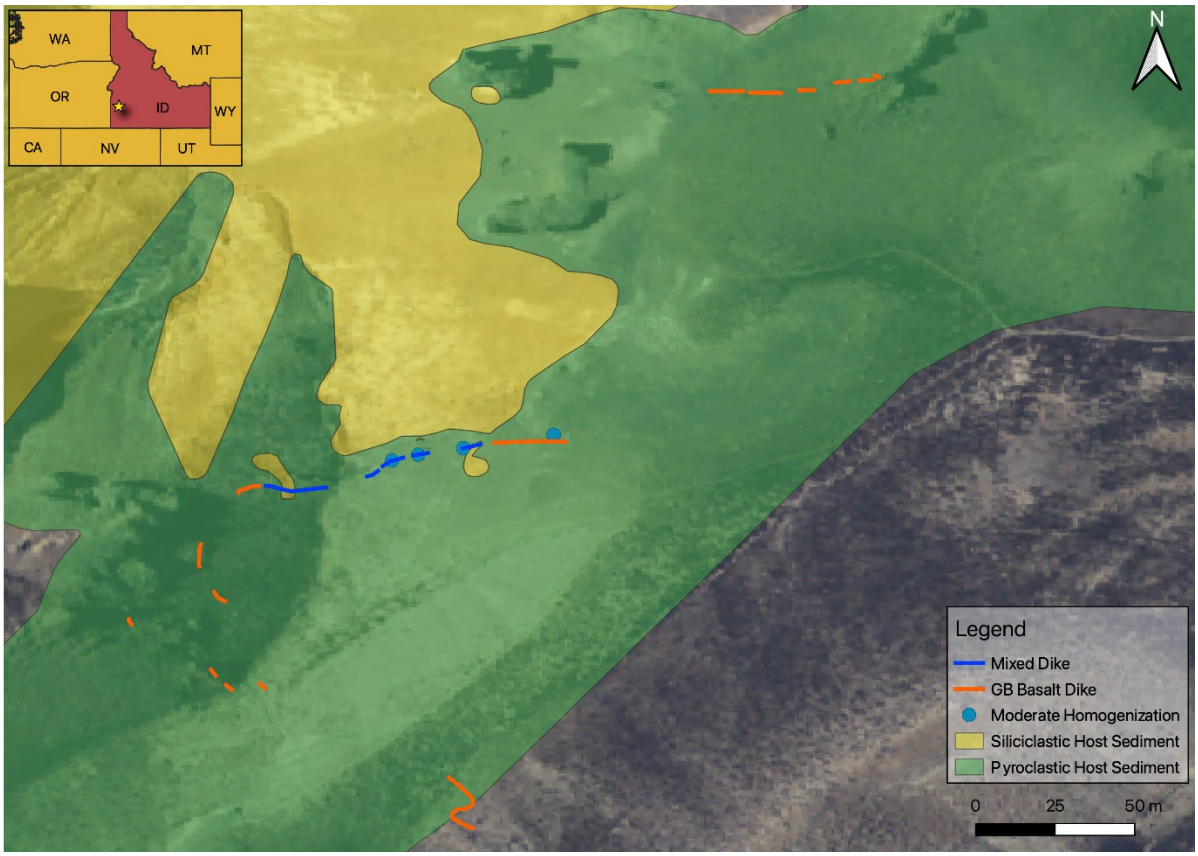

Figure 3. 33 Map showing the location of the moderate homogenized samples collected. GB basalt dikes are highlighted in orange and the mixed dikes are highlighted in blue.

Thin sections of the three samples consist of anhedral to euhedral quartz, subhedral to euhedral plagioclase, subhedral olivine, subhedral clinopyroxene, and subhedral to anhedral oxides. The matrix of these samples is tachylyte. Quartz is the dominant mineral, in samples 21-HG-0010 and21-HG-015, at 40-65%, followed by plagioclase at 5-10%, olivine at no more than 2%, clinopyroxene making up no more than 2%.

Point counts for both thin sections yielded N numbers listed in table 3.9. Sample 21-HG-32 is plagioclase dominate, comprising 25-45%, and has an N number of 127 (Figure 3.34). This sample has a section in which its minerals are too small to identify making the minerals in that particular area inoperable and may skew the data. An# of plagioclase was calculated from EDS data. Plagioclase crystals are predominantly bytownite, An# ranging from 0.70-0.90, followed by andesine with an An# ranging from 0.30-0.50, labradorite with An# ranging from 0.50-0.70, and albite ranging from 0-0.10 (Table 3.10 and Figure 3.35). Several have sieve textures and are mainly andesine (0.30-0.50). The quartz crystals analyzed yielding normalized mass concentration percentages of 35-51% O and 13--24% Si (Figure 3.36). Analysis of the groundmass show that it is basaltic in nature (Figure 3.37).

Moderate Homoginezation				
Sample ID	Pl	Qtz	Rock Fragments	Other
21-HG-032a	127	86	1	13
212-HG-009	4	81	0	28
21-HG-015	25	464	0	33
21-HG-010	34	438	0	8

Table 3. 9 Moderate homogenization N numbers calculated from point counts.

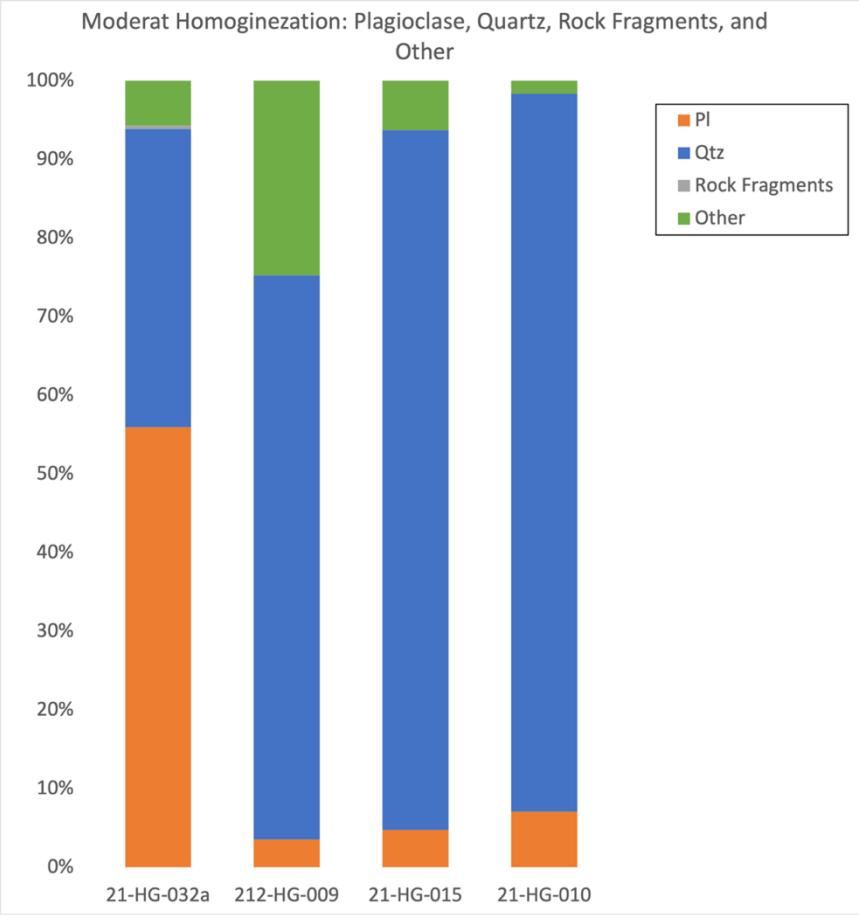

Figure 3. 34 Bar graph of GB basalt N numbers calculated from point counts then separated into the categories of plagioclase (orange), quartz (blue), rock fragments (gray), and other (green). The other category consists of the minerals: olivine, clinopyroxene, mica, oxides, and calcite. Samples are ordered based off their radial distance from the nearest mixed dike.

Moderate Homogineztion An#							
Sample	Spectra	Ca	Na	K	An #	An %	Name
21-HG-009	4	5.08	0.87	3.00	0.57	56.76	Labradorite
21-HG-009	5	8.13	0.54	2.12	0.75	75.35	Bytownite
21-HG-009	10	3.45	0.67	1.28	0.64	63.89	Labradorite
21-HG-009	4	11.29	1.04	1.64	0.81	80.82	Bytownite
21-HG-009	5	3.63	0.74	3.78	0.45	44.54	Andesine
21-HG-015	3	4.78	1.44	2.72	0.53	53.47	Labradorite
21-HG-015	4	0.64	0.89	2.13	0.17	17.49	Oligoclase
21-HG-015	5	1.41	0.99	1.63	0.35	34.99	Andesine
21-HG-015	9	2.22	1.03	1.63	0.45	45.49	Andesine

Table 3. 10 Moderate homogenization An#, An%, and name taken from several elemental spectra.

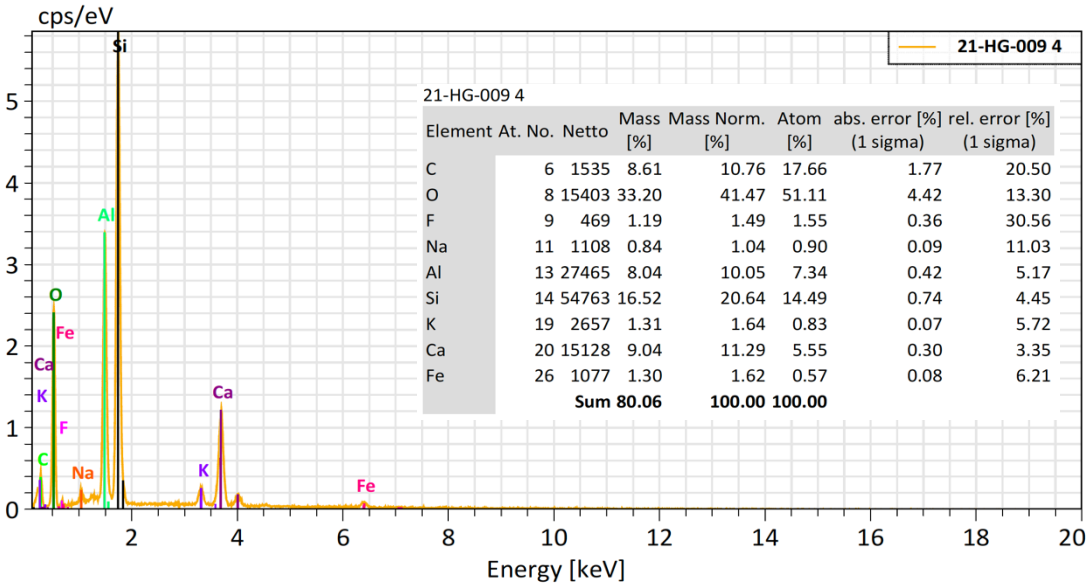

21-HG-009 4

Element	At. No.	Netto	Mass [%]	Mass Norm. [%]	Atom [%]	abs. error [%] (1 sigma)	rel. error [%] (1 sigma)
C	6	1535	8.61	10.76	17.66	1.77	20.50
O	8	15403	33.20	41.47	51.11	4.42	13.30
F	9	469	1.19	1.49	1.55	0.36	30.56
Na	11	1108	0.84	1.04	0.90	0.09	11.03
Al	13	27465	8.04	10.05	7.34	0.42	5.17
Si	14	54763	16.52	20.64	14.49	0.74	4.45
K	19	2657	1.31	1.64	0.83	0.07	5.72
Ca	20	15128	9.04	11.29	5.55	0.30	3.35
Fe	26	1077	1.30	1.62	0.57	0.08	6.21
		Sum	80.06	100.00	100.00		

Figure 3. 36 Elemental spectra of a plagioclase in sample 21-HG-009.

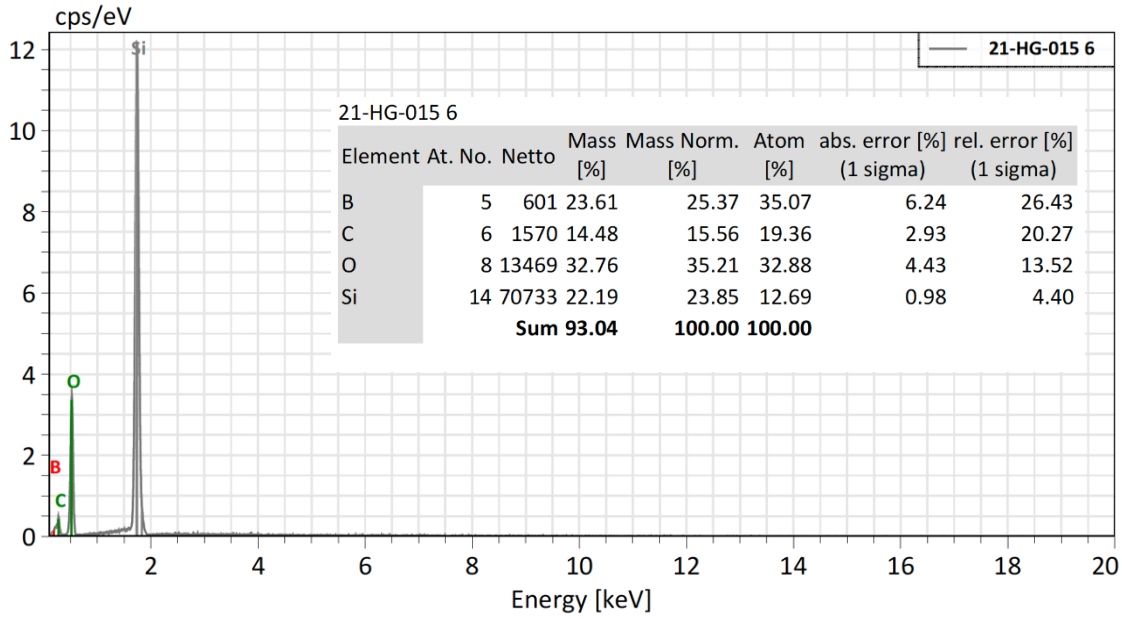

21-HG-015 6

Element	At. No.	Netto	Mass [%]	Mass Norm. [%]	Atom [%]	abs. error [%] (1 sigma)	rel. error [%] (1 sigma)
B	5	601	23.61	25.37	35.07	6.24	26.43
C	6	1570	14.48	15.56	19.36	2.93	20.27
O	8	13469	32.76	35.21	32.88	4.43	13.52
Si	14	70733	22.19	23.85	12.69	0.98	4.40
		Sum	93.04	100.00	100.00		

Figure 3. 35 Elemental spectra of quartz in sample 21-HG-015.

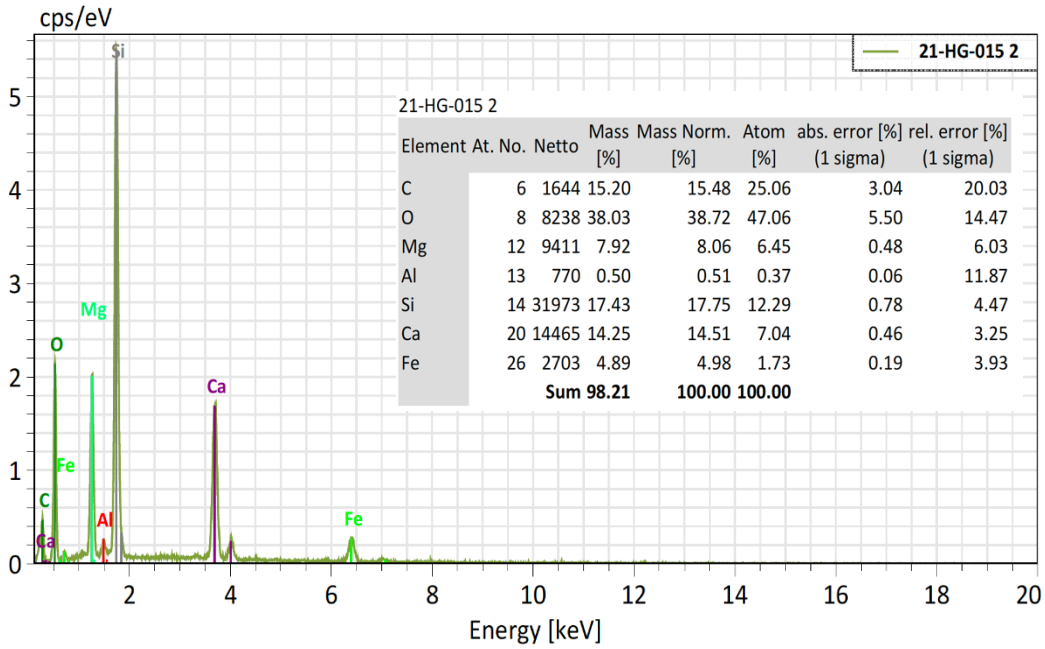

Figure 3. 37 Elemental spectrum of tachylyte in sample 21-HG-015.

3.1.5 Homogenized

In homogenized dikes it is visually not possible to distinguish between basalt and siliciclastic host in the field and in hand sample (Figure 3.38a-b). Homogenized rocks have a high hardness, vitric luster, high density, and present local columnar joints. Vesicles range from rounded to coalesced and comprise about 0-30% of localized sections. Some vesicles are elongated and show preferential alignment subparallel to parallel to the margin of the dikes or to columns of columnar joints (Figure 3.39). Dikes that contain homogenized rock propagate through pyroclastic and siliciclastic host material and transition into least homogenized and moderately homogenized zones.

Figure 3. 38 Homogenized hand sample photos demonstrating the indistinguishability of host material type dominance. In addition, illustrating the homogenization with courser grained siliciclastic host (A) and finer grained siliciclastic host (B). The scale in both images is in mm.

Figure 3. 39 Vesicles are elongated subparallel to parallel in relation the jointing of columnar joints.

Columnar joints are present in the homogenized dikes in the southwestern corner of the exposure (Figure 3.40 and 3.20). They sit at a depth of -77.60 m while the mixed dike is at a depth between -27.21 - -64.89 m. Samples 21-HG-024 to 026 were collected from the columnar joints. An injection of basalt transitions into homogenized columnar joints (Figure 3.20).

Figure 3. 40 Field image of the homogenized columnar joints. Sample 21-HG-024-26 were taken from the right to the left as the grain size of the joints changed from coarse to fine.

The siliciclastic material the GB basalt mixed with ranged from fine to coarse grained and range and in color from a dark gray to light gray (Figure 3.38a-b). Sample 21-HG-024 has the coarsest grains and is the most fragile homogenized sample collected (Figure 3.38a). The dikes cut through scoria that consists of fine grained siliciclastic lithics and angular to subangular basalt lithics that are frothy and dense. A total of six samples were collected and are listed in table 3.1 in addition to the appendix.

Thin sections consist of subhedral quartz, euhedral plagioclase, subhedral olivine, subhedral to euhedral clinopyroxene, and euhedral oxides (Figure 3.41). Vesicles comprise no more than 5% and are rounded to coalesced. Some vesicles have the onset of vesicle fill while others are almost completely filled. Quartz is the most abundant mineral, comprising 30-70%, plagioclase comprise 10-20%, olivine comprising 5%, clinopyroxene comprising no more than 5%. Oxides are present (3%) with in minerals and are rounded to blocky in shape.

Figure 3. 41 Cross polarized photomicrograph of sample 21-HG-025 that shows the crystal structure of minerals in the homogenized category.

Point counts for both thin sections yielded N numbers listed in the in figure 3.42 and table 3.11. An# from plagioclase phenocryst were calculated from EDS data and show that they are anorthite (0.90-1.00) (Table 3.12). Quartz was analyzed and have normal mass concentrations of 49-50% O and 48% Si (Figure 3.43). The ground mass was analyzed and is basaltic in nature (Figure 3.44).

Homogenized				
Sample ID	Pl	Qtz	Rock Fragments	Other
21-HG-024	35	595	0	96
21-HG-025	13	405	0	55
21-HG-026	9	428	0	30
21-HG-033	42	776	0	37
21-HG-007	179	190	0	16
21-HG-008	29	284	0	6

Table 3. 11 Homogenized N numbers calculated from point counts.

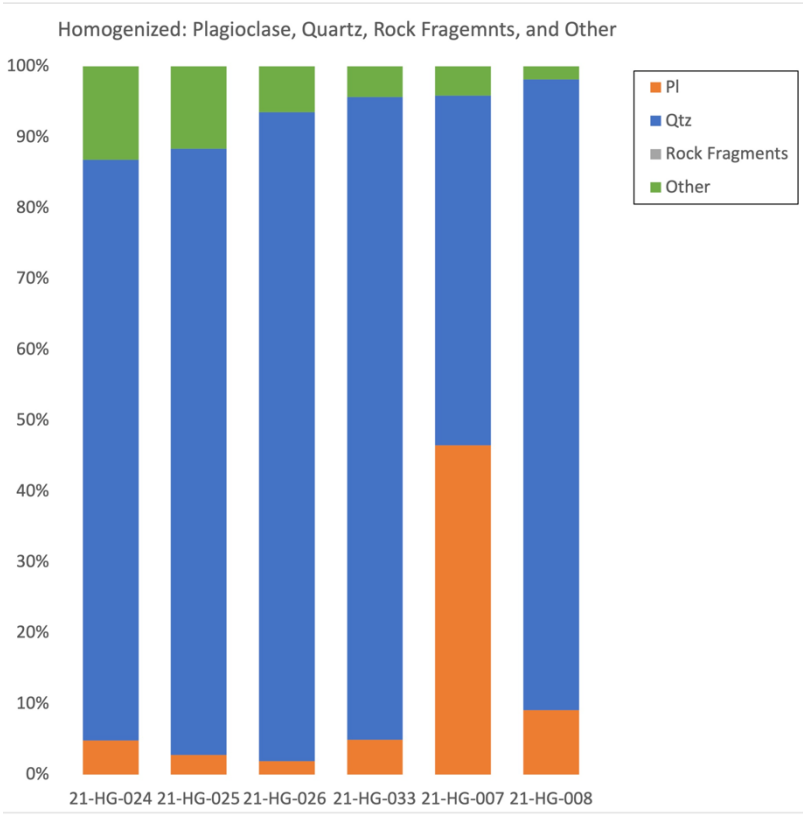

Figure 3. 42 Bar graph showing the dominant minerals in each homogenized sample collected.

Homogenized An#							
Sample	Spectra	Ca	Na	K	An #	An %	Name
21-HG-007	5	0.30	0.90	3.54	0.06	6.33	Albite
21-HG-007	7	3.22	1.96	0.46	0.57	57.09	Labradorite
21-HG-007	1	8.06	4.02	1.11	0.61	61.11	Labradorite
21-HG-007	3	1.22	1.30	5.72	0.15	14.81	Oligoclase
21-HG-007	4	6.17	3.06	2.09	0.55	54.51	Labradorite
21-HG-007	5	12.10	2.18	1.33	0.78	77.51	Bytownite
21-HG-007	6	4.90	1.99	3.88	0.45	45.50	Andesine
21-HG-007	7	6.25	2.46	2.13	0.58	57.66	Labradorite
21-HG-007	4	1.09	1.01	5.50	0.14	14.34	Oligoclase
21-HG-007	5	1.14	1.13	5.29	0.15	15.08	Oligoclase
21-HG-007	6	1.43	1.07	5.23	0.18	18.50	Oligoclase
21-HG-026	1	16.64	0.18	0.04	0.99	98.70	Anorthite
21-HG-026	2	17.15	0.21	0.01	0.99	98.73	Anorthite
21-HG-026	3	19.57	0.15	0.18	0.98	98.34	Anorthite
21-HG-026	4	17.03	0.54	0.04	0.97	96.71	Anorthite
21-HG-026	5	18.06	0.52	0.10	0.97	96.68	Anorthite
21-HG-033	5	13.58	0.15	0.02	0.99	98.76	Anorthite
21-HG-033	8	13.51	0.19	0.66	0.94	94.08	Anorthite

Table 3. 12 Bar graph of homogenized mixing samples N numbers calculated from point counts for the categories of plagioclase (orange), quartz (blue), rock fragments (gray), and other (green). The other category consists of the minerals: olivine, clinopyroxene, mica, oxides, and calcite.

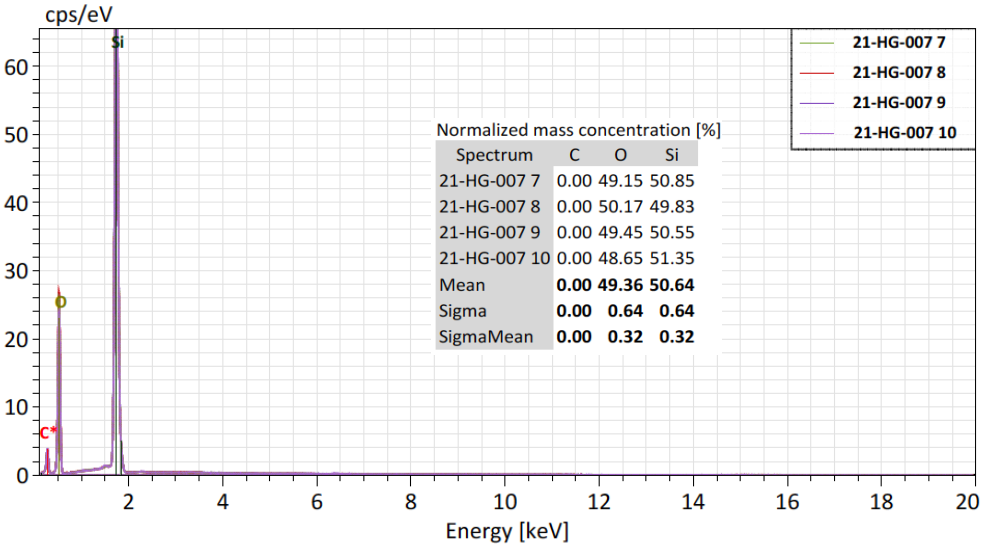

Figure 3. 43 BSE image highlighting elemental spectra 1 and 2 (quartz crystal).

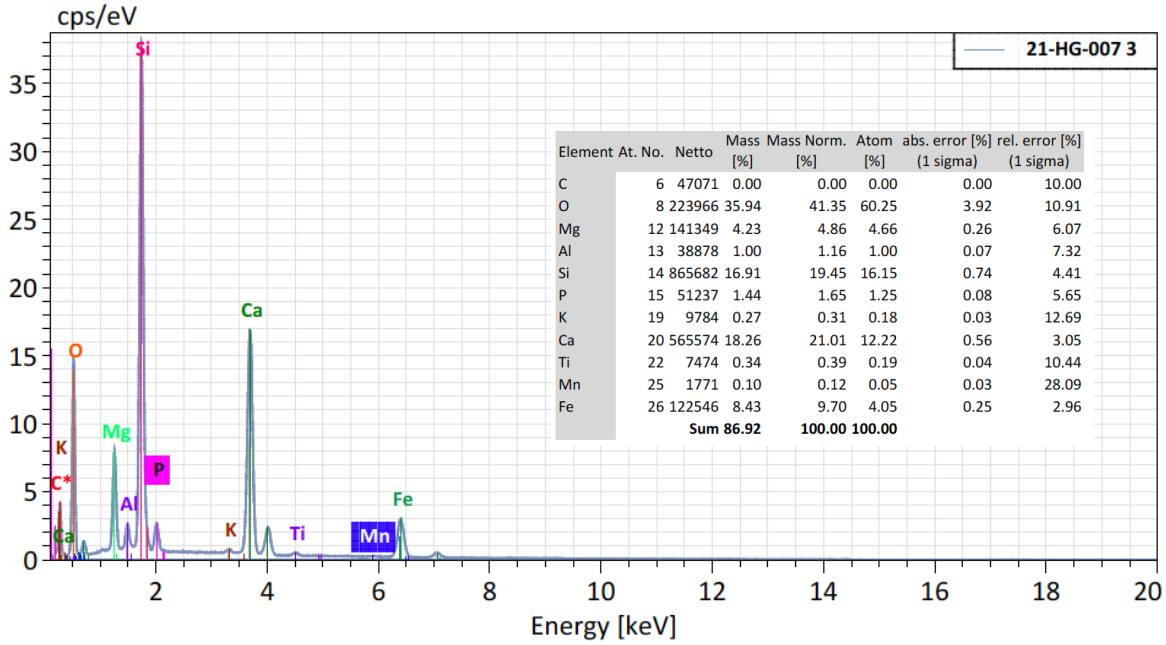

Element	At. No.	Netto	Mass [%]	Mass Norm. [%]	Atom [%]	abs. error [%] (1 sigma)	rel. error [%] (1 sigma)
C	6	47071	0.00	0.00	0.00	0.00	10.00
O	8	223966	35.94	41.35	60.25	3.92	10.91
Mg	12	141349	4.23	4.86	4.66	0.26	6.07
Al	13	38878	1.00	1.16	1.00	0.07	7.32
Si	14	865682	16.91	19.45	16.15	0.74	4.41
P	15	51237	1.44	1.65	1.25	0.08	5.65
K	19	9784	0.27	0.31	0.18	0.03	12.69
Ca	20	565574	18.26	21.01	12.22	0.56	3.05
Ti	22	7474	0.34	0.39	0.19	0.04	10.44
Mn	25	1771	0.10	0.12	0.05	0.03	28.09
Fe	26	122546	8.43	9.70	4.05	0.25	2.96
			Sum 86.92	100.00	100.00		

Figure 3. 44 EDS spectra 3 of tachylyte from homogenized sample 21-HG-007.

3.2 Geochemistry (Whole Rock)

3.2.1 Guffey Butte

Four basalt and four homogenized samples, two collected by Bennis (2019), analyzed for major and trace elements (Figure 3.45 and Table 3.13). In addition, basalt samples from Watson (1999) have been added. All coherent samples have low alkali content, plot as basalts, and fall within the tholeiitic range (Figure 3.46 and 3.47). Watson (1999) samples have low alkali content and plot as basalts. All but two samples from Watson (1999) fall within the tholeiitic range. There is low variation in the oxide weight precent of 21-HG samples. 21-HG basalt samples cluster together with samples from Watson (1999). However, there are few acceptations 21-HG-027 and three samples from Watson (1999). The Mg#'s calculated for 21-HG basalts range from 0.26-0.31 and 0.34-0.48 for homogenized samples (Appendix). Mg#'s from Watson (1999) range from 0.25-0.45. Common basalts from the WSRP, collected by Sherviais *et al*. (2002) and White *et al*. (2002), have Mg# ranging from 0.35-0.59. Rb was included as a component which represents K-rich plagioclase and Sr was included as component which represents Ca-right plagioclase (Figure 3.48). Guffey Butte homogenized samples display relatively high amounts of Rb and SiO2 when compared to the basalt samples. Homogenized samples show a distinct geochemical trend of an enrichment of alkalis and silica in relation to MgO wt. %. Two (21-HG-033 and GB002(1)) of the four homogenized samples behave similarly while 21-HG-016 and GB002(2) have higher SiO2 wt. %.

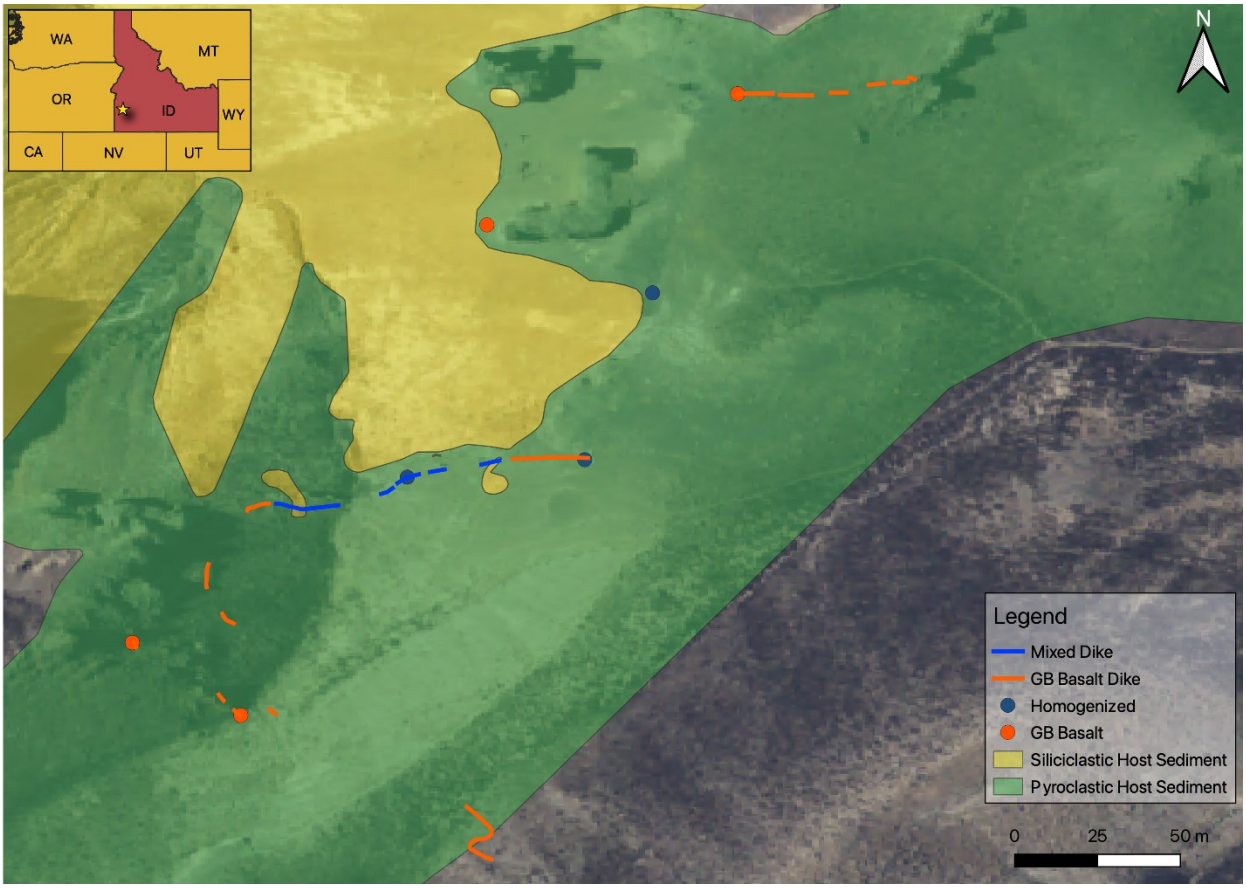

Figure 3. 45 Map showing the location of samples used for geochemistry. Some samples overlap due to their close proximity.

Geochemistry Samples	
Sample ID	**Lithology**
21-HG-021	Basalt
21-HG-027	Basalt
21-HG-036	Basalt
21-HG-002	Basalt
21-HG-016	Homogenized
21-HG-033	Homogenized
GB-002 (1)	Homogenized
GB-002 (2)	Homogenized

Table 3. 13 List of samples taken for geochemical analysis. Samples GB-002 were taken by Kadie Bennis 2019.

Trace elements show a degree of similarity between the basalt across dikes at Guffey Butte suggesting they originated from a similar magma source. Normalized trace elements are plotted against primitive mantel (Sun and McDonough, 1995), showing that basalts are enriched in incompatible elements and have a similar trend (Figure 3.49). Homogenized samples are more enriched in incompatible elements and are not clustered together. Both the basalt and homogenized samples resemble the Sun and McDonough (1995) trend of oceanic alkali basalt. All samples have a negative Eu anomaly and a positive Nd anomaly, but the homogenized samples have steeper negative and positive slopes respectively. Incompatible trace element ratios show high variations between basalt (Nb/Y 0.54-0.58; Zr/Y 6.16-7.11) and homogenized samples (Nb/Y 0.58-0.74; Zr/Y 7.51-10.10) (Figure 3.50 and Appendix). Complete major and trace element data sets can be located in the Appendix.

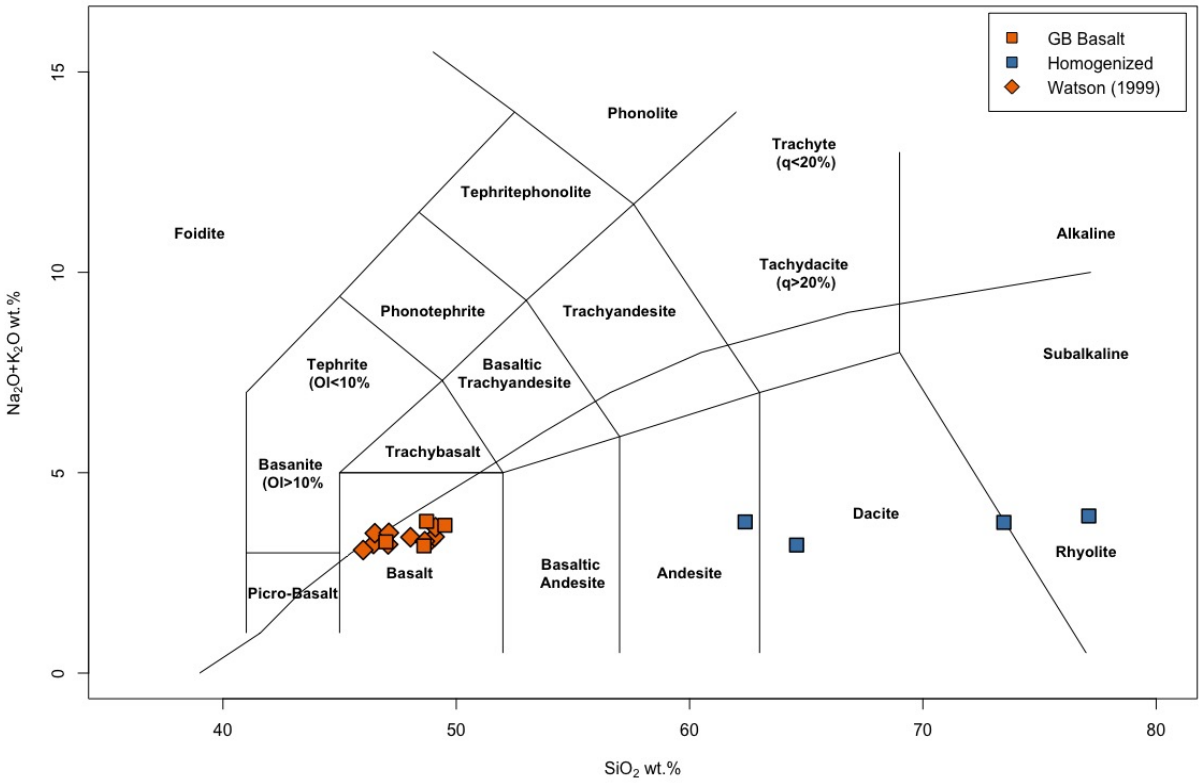

Figure 3. 46 TAS diagram of GB basalt and homogenized samples with the edition of Guffey Butte samples from Walters 1999.

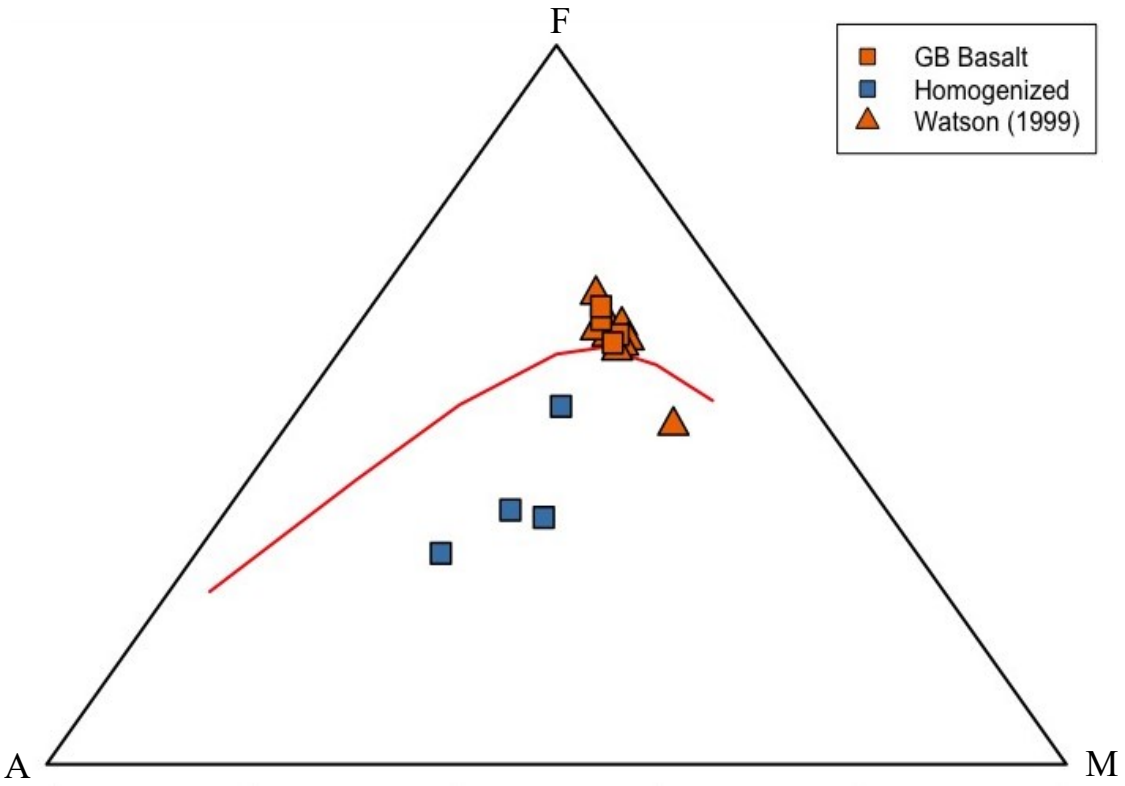

Figure 3. 47 AFM diagram of GB basalt (blue squares) and homogenized samples (orange squares). Guffey Butte samples from Walters (1999) (orange triangles).

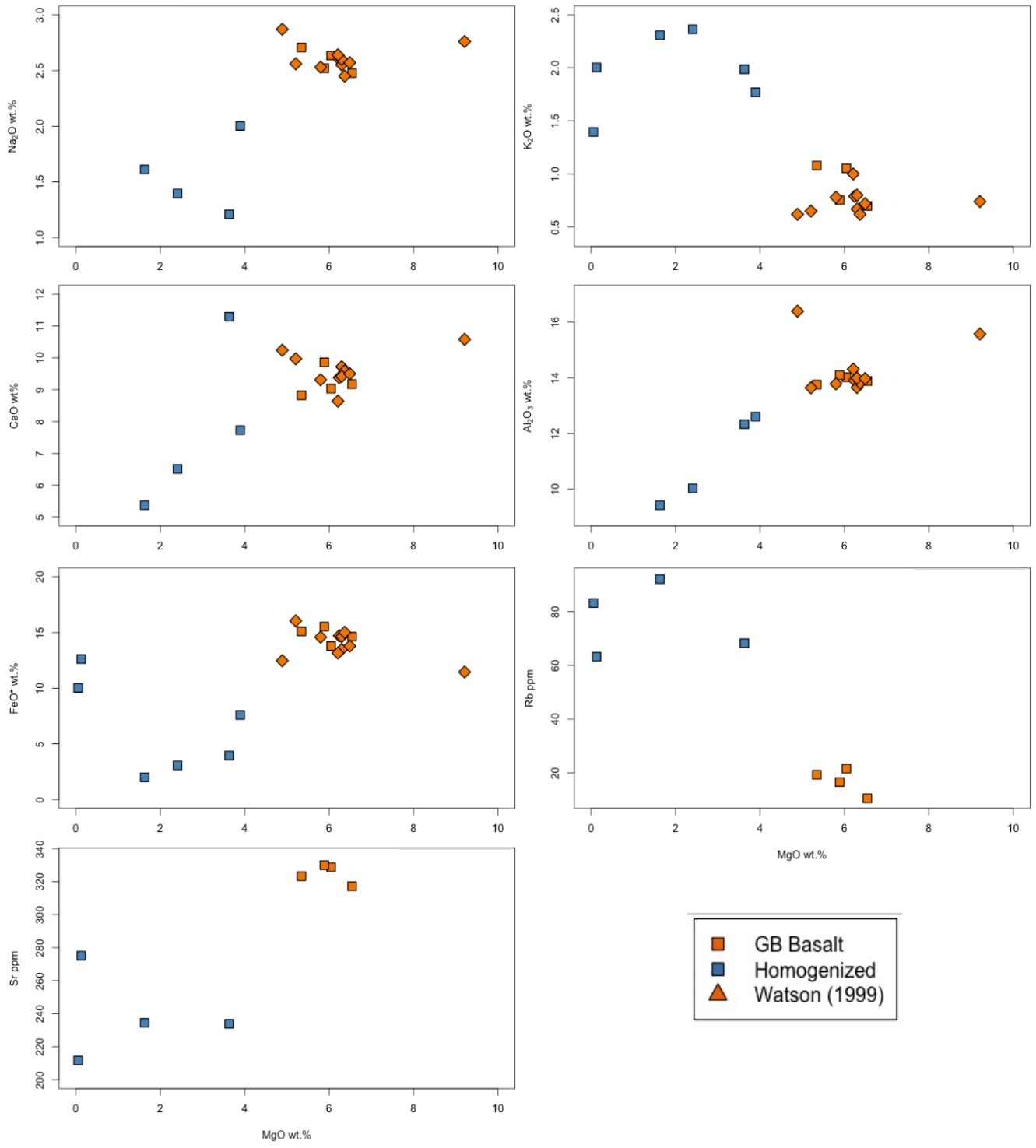

Figure 3. 48 Variation diagram that plots Na2O, K2O, Al2O3, CaO, FeO2, Sr ppm, and Rb ppm. These plots highlight the chemical abnormalities between the GB basalt and homogenized. Basalt samples from Watson (1999) don't have data from Sr ppm and Rb ppm.

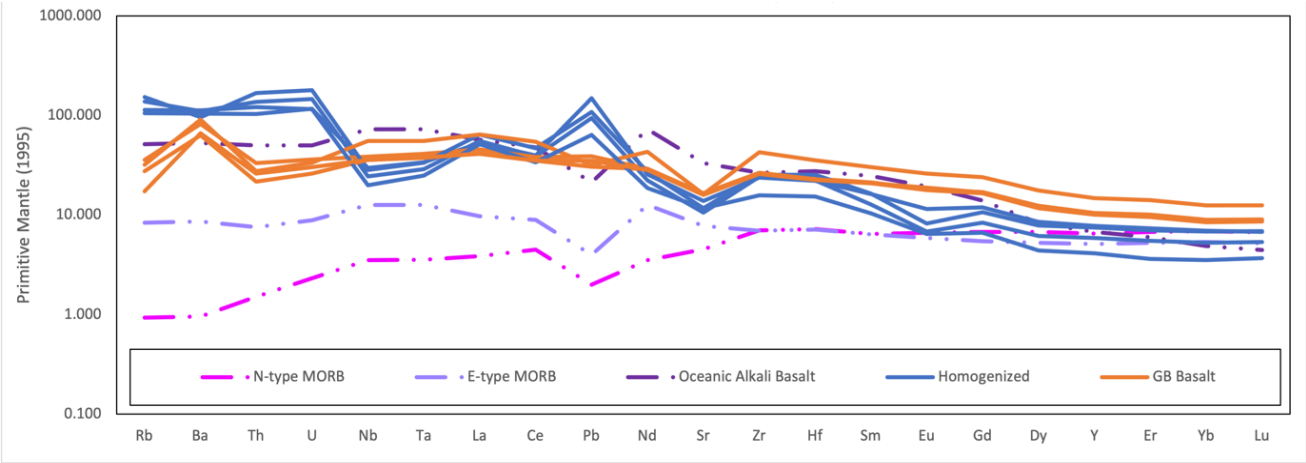

Figure 3. 49 REE plot of GB basalt (orange) and homogenized (blue) samples from Guffey Butte. Both plot similarly to an oceanic alkali basalt. Little variation is shown in GB basalt samples and homogenized samples. Both GB basalt and homogenized samples have negative anomalies in Eu and Sr. Homogenizes samples have a positive Rb anomaly.

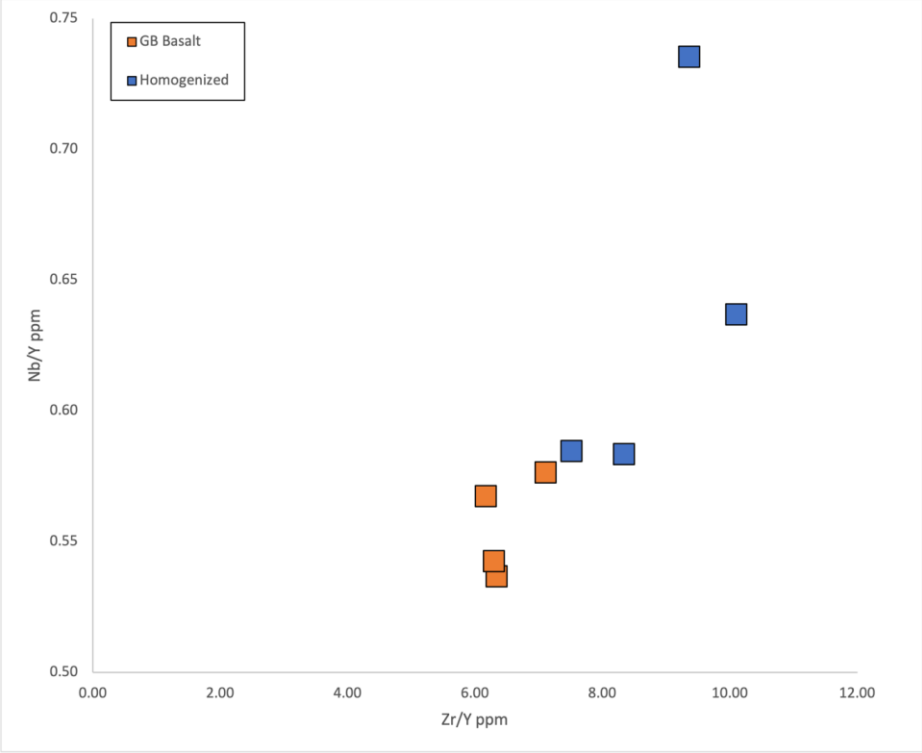

Figure 3. 50 Nb/Y vs. Zr/Y, are typically used as a measure of different levels of melting, shows variation in melting between Gb basalt and homogenized samples.

3.2.2 Guffey Butte to the WSRP

Coherent basalt samples of Guffey Butte were compared to those collected from nearby volcanic fields within the WSRP (71 Gulch, Mountain Home basalt, and Melba basalts) using major and trace elements (Figure 3.51 and 3.52) (Morrow, 1996; Shervais *et al.*, 2002; White *et al*., 2002). Silica content was similar over all sites; all samples plotted as tholeiitic basalts with a few exceptions. Mg# range from 0.25-0.59 with Guffey Butte samples having the lowest Mg#. The multi-element plot shows an enrichment of incompatible elements with an overall negative trend across the WSRP basalts (Figure 3.53). Mg#'s from Guffey Butte plot lower than 71 Gulch and the WSRP (Figure 3.54). In addition, it shows slight variability as the samples from Mountain Home and the Melba basalts. A distinct negative trend is visible in TiO2 to Mg# as Mg# increase.

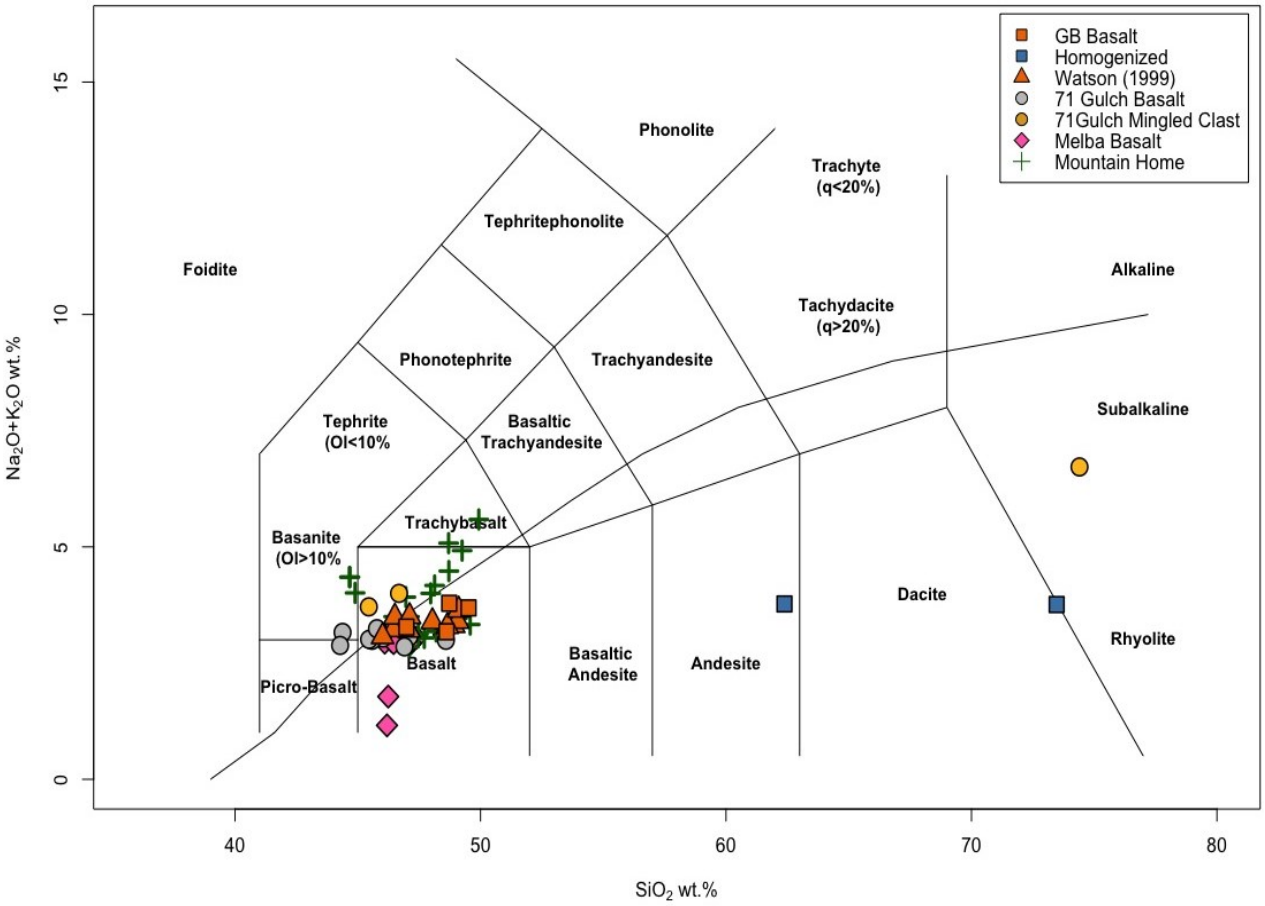

Figure 3. 51 TAS diagram plotting GB basalt and homogenized samples to basalt from the WSRP (Morrow, 1996; Watson, 1999; Shervais *et al*., 2002; White *et al*., 2002; Bennis and Graettinger, 2020). GB basalts plot similarly to basalts of the region with exception to the homogenized samples.

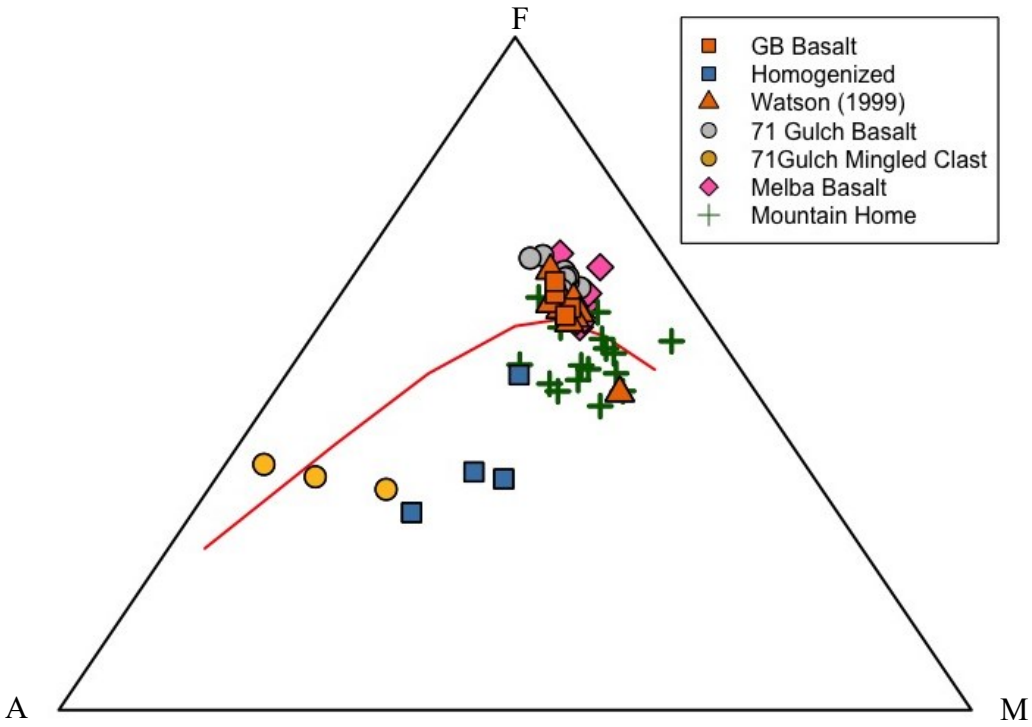

Figure 3. 53 AFM diagram illustrating GB basalt and homogenized samples to basalts of the WSRP. Most samples plot as tholeiitic basalts (Morrow, 1996; Watson, 1999; Shervais *et al*., 2002; White *et al*., 2002; Bennis and Graettinger, 2020).

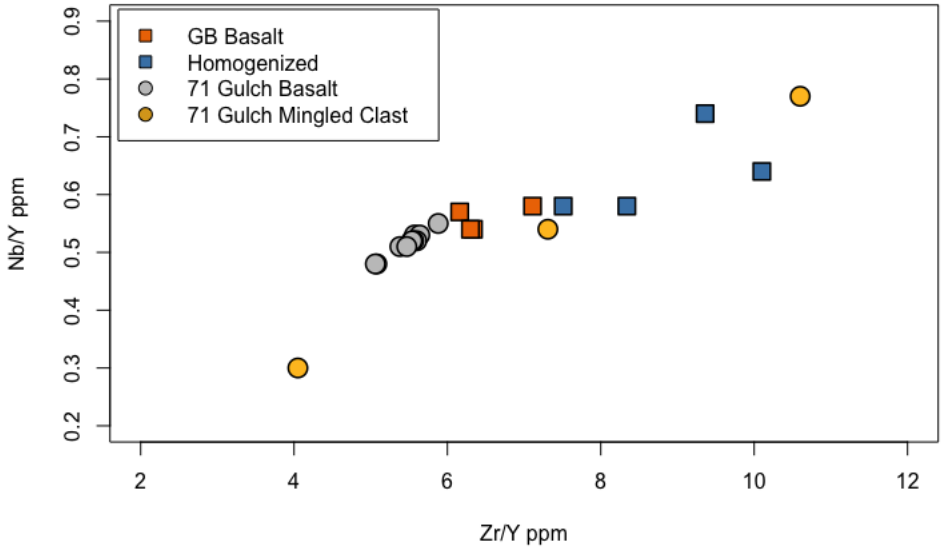

Figure 3. 52 Multi-element plot highlighting enrichment in trace elements across the Western Snake River Plain (Bennis, 2019; Bennis and Graettinger, 2020; Graettinger et al., 2020).

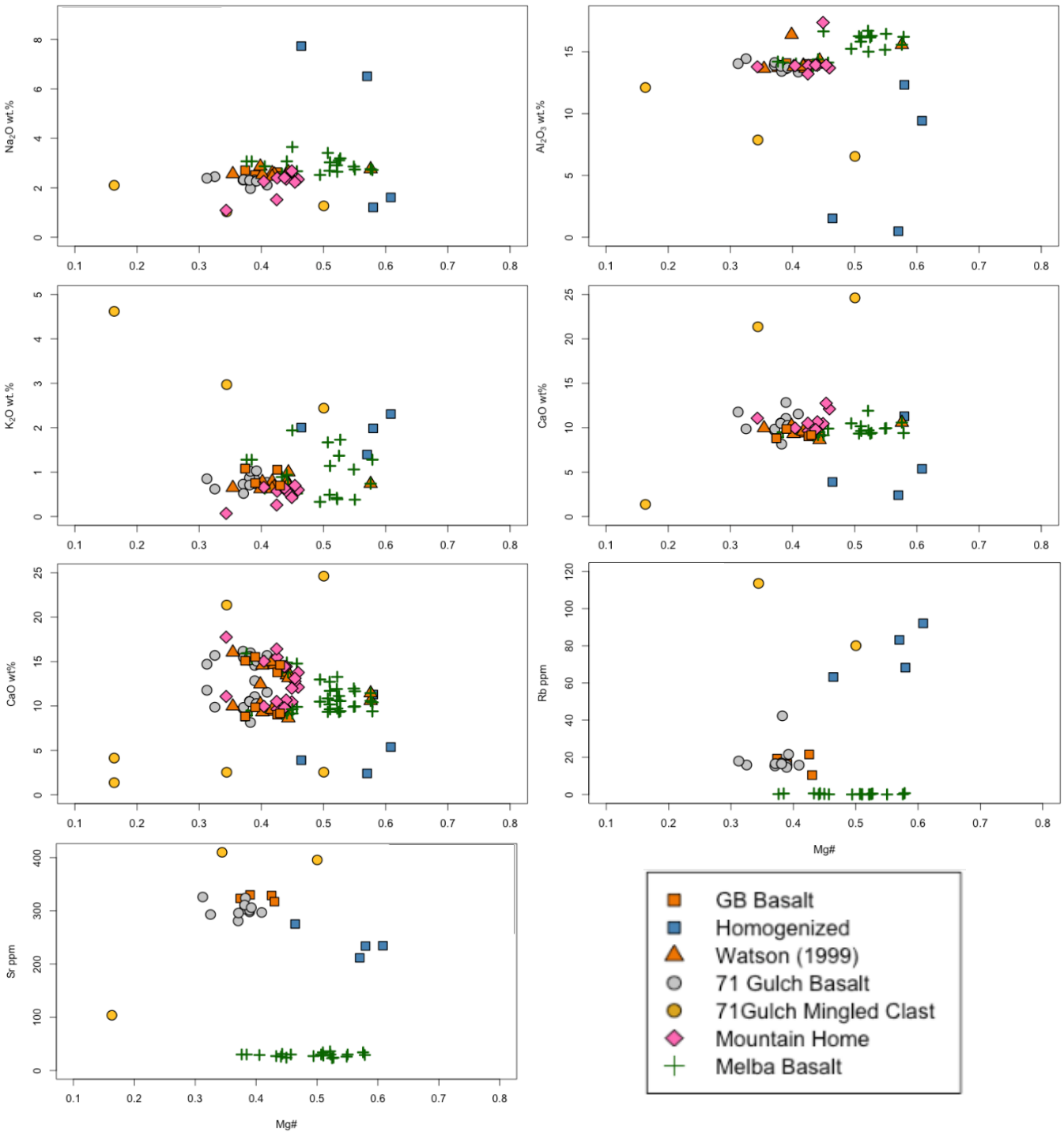

Figure 3. 54 Harker diagrams of major oxides against Mg#. Mg# is partially higher in homogenized samples compared to GB basalts and to the basalts of the region (Morrow, 1996; Watson, 1999; Shervais *et al*., 2002; White *et al*., Bennis and Graettinger, 2020).

CHAPTER 4. DISCUSSION

Major element data indicated that GB basalts are related to one batch of magma and that they are primitive in comparison to the mixing samples. A chemical separation between the mixed samples and GB basalt samples are illustrated (Figure 3.48-3.56). GB basalts are more evolve as they are low in MgO (Winter, 2001) while mixed samples are high in MgO (Figure 3.50). Trace element chemistry of GB basalts cluster together with exception to sample 21-HG-027 and plot below the homogenized samples (Figure 3.51 and 3.55). Primitive mantle lines of GB basalts plot tightly which indicate a singular batch of magma. The homogenized mixed samples plot tight together showing similar chemical componentry. There is a negative Eu and Sr anomaly in all samples which can be correlated to the crystallization of plagioclase minerals in the system. Homogenized samples have a positive anomaly for Rb which can be correlated to the presence of K-Feldspar.

GB basalts propagated through wet unconsolidated siliciclastic sediment of the Glenns Ferry formation and are predominantly tabular. GB basalts are contaminated with up to 20% of both basaltic and siliciclastic lithics and are at the shallowest depths (-37.55- -86.77 m) (Table 3.1). In contrast, lithics in mixed samples range from 0-85% with the least homogenized areas/samples contain the most lithics and homogenized little to no lithics made of GB basalt, siliciclastic rock fragments, and xenocrysts of quartz. The mixed dikes were located in the deepest parts of the exposure (-27.21- -51.44 m) (Figure 4.2). An exception to this is the mixed columns that are located laterally away from the main outcrop where the GB basalt dikes are located. This essentially shows that dike contamination increases as the depth and relative pressure increased. Cooled margins and the columnar joint texture in mixed dikes margins indicate that contraction occurred due to cooling of the hot

mixture of basalt and sediment. Figure 4.1 illustrates the field relationship previously described. Vesicles are visible in both GB basalts and mixed dikes and their elongation runs subparallel to parallel in relation to the dike's margins (Figure 3.14b and 3.23). This is also true in hand sample and thin section (Figure 4.3). Direct transitions between GB basalt and mixing in addition to quenched margins observed in the field indicates that the mixed portions were continuations of the GB basalt dike. The GB basalt and siliciclastic componentry is preserved in mixing with differences in grain shape and angularity, which could be contributed to the amount of movement they experienced, and minerals.

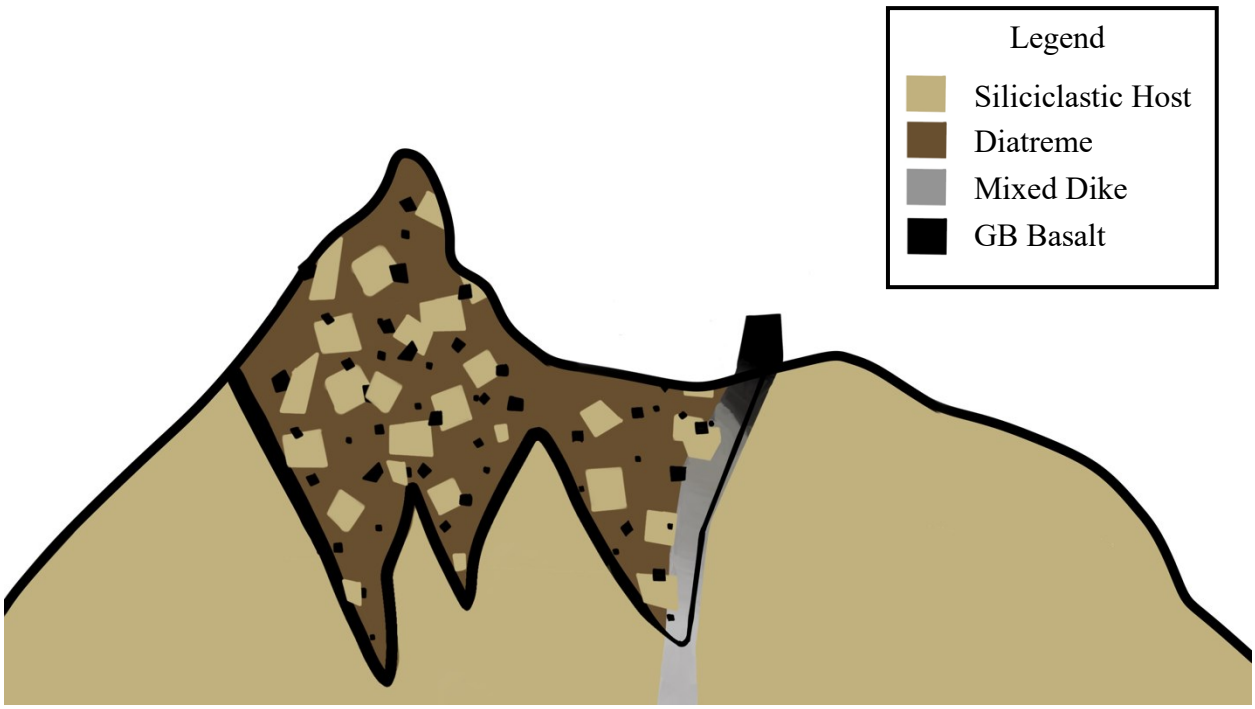

Figure 4. 1 Cartoon rendering showing the field relationship between the GB basalt, the mixed dike, pyroclastic host sediment of the diatreme, and the siliciclastic host. The depth difference between mixed dike and GB basalt dike is highlighted. Not to scale.

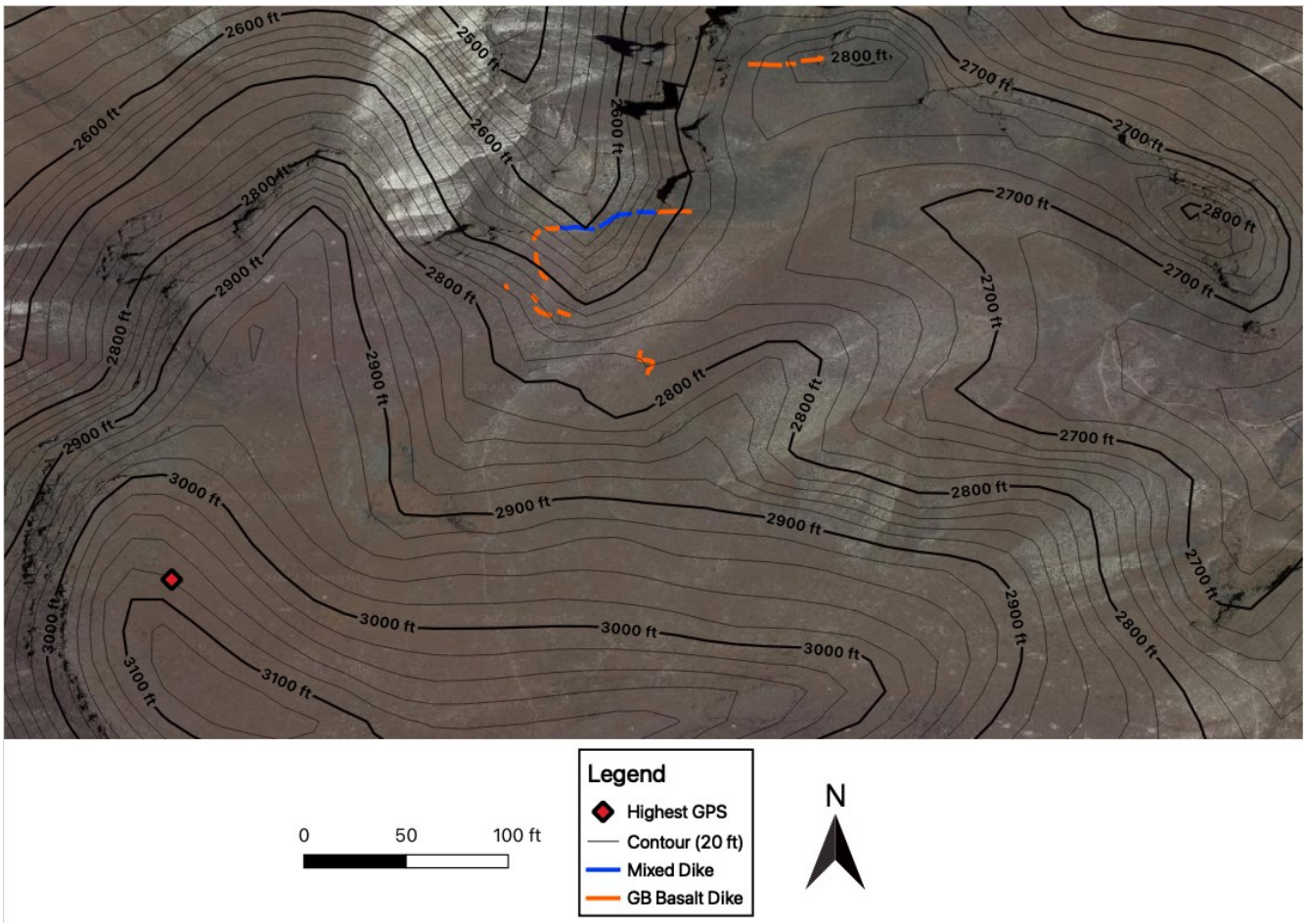

Figure 4. 2 Topographic map illustrating the difference in depth between GB basalt dikes and the mixed dikes.

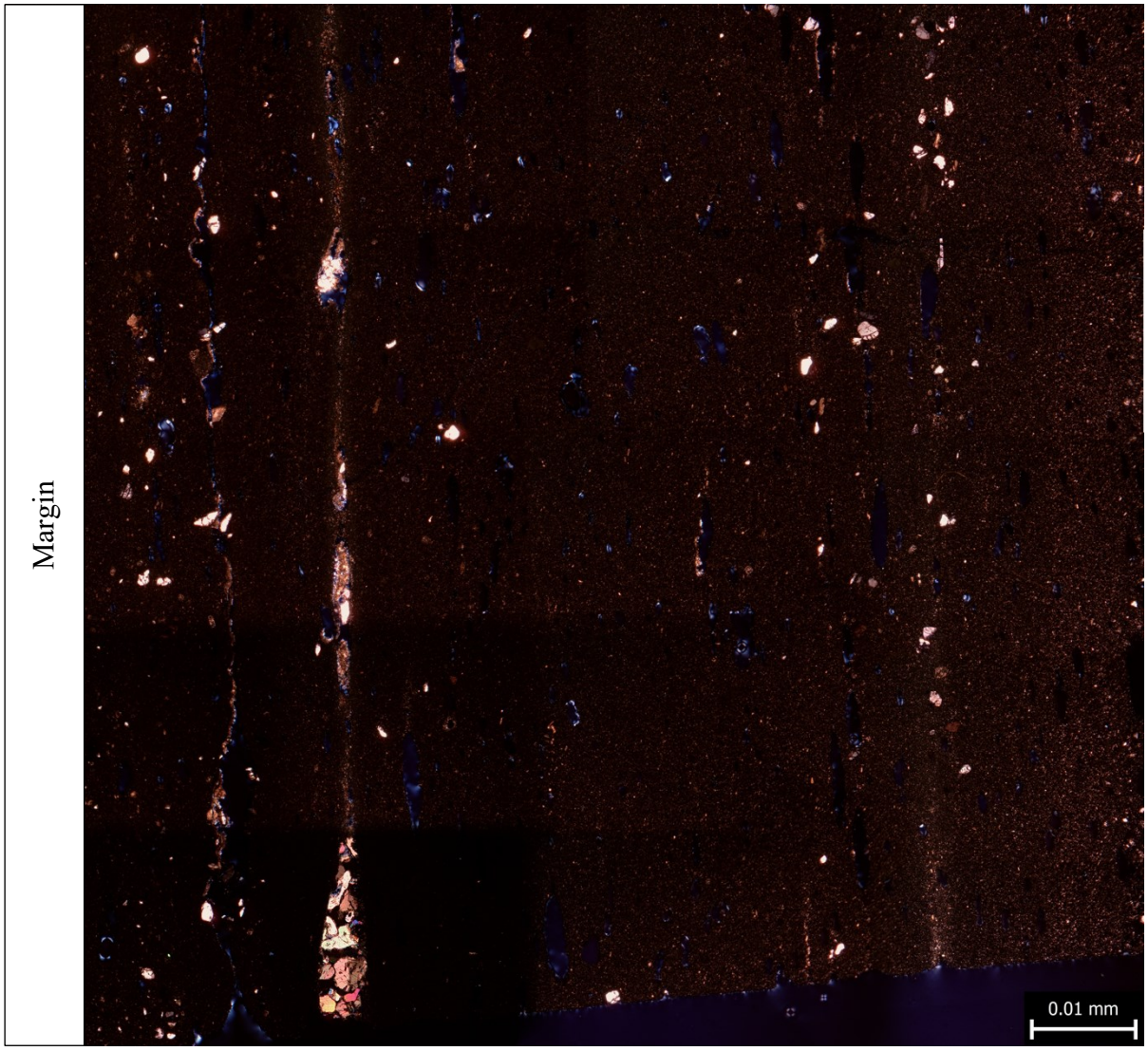

Figure 4. 3 Thin section of sample 21-HG-009 that shows that vesicles are elongated subparallel to parallel to the margin of mixed dikes.

4.1 Is it mingling?

The presence of GB basalt, while hard to see in homogenized samples, is present at a microscopic level. In thin section components of GB basalts and siliciclastic sediments are preserved with exception to mica (Table 3.7, 3.9, and 3.11). All mixed samples contain olivine, quartz, plagioclase, clinopyroxenes, k-feldspar, calcite, and oxides. Olivine and clinopyroxene in GB basalts range from subhedral to euhedral. In mixing samples, they are primarily anhedral with few being subhedral. The battered state in which basaltic minerals in the mixed samples have been observed indicate that the mixed dikes environment was turbulent enough to break up the basaltic minerals as the basalt integrated with the siliciclastic material. Mixed samples all have a groundmass of tachylyte (Figure 3.31, 3.37, and 3.46). Mixed sections are composed of disaggregated sediment grains and should not be considered a whole xenolith. The siliciclastic material is not solely made up of siliciclastic minerals as GB basalt minerals are amongst the siliciclastic ones, and they are all separated by tachylyte groundmass. Minerals do not cluster together to from glomerocrysts like the ones found in GB basalt samples (3.13c). There are no glassy films surrounding. Each mixed section is not separated by a glassy film and their boundaries are not rounded. Mixing happened while dike was still hot before quench margins and temperatures were high enough to form columnar joints.

4.2 Temperature of mixed dike

Knowing that biotite from the siliciclastic sediments is not preserved in the mixed dikes and that there is no evidence of melting of quartz and feldspar grains from the mixed samples thin sections a temperature range can be approximated. Typical basaltic

temperatures are between 1000-1200°C. Low quartz is stable up to 573°C and cristobalite from 1470-1720°C (Larson, 1929) (Figure 4.4). Quartz melts at a temperature of 1710°C (Ainslie *et al*., 1961, Aanslie *et al*., 2007). Plagioclase melts at a temperature of 1,099°C at 0 atm (Smith, 1972; Branlund and Hofmeister, 2012). K-Feldspar melts at a temperature of 1,200°C (Smith, 1972). All mixed samples contain both GB basalt and siliciclastic minerals with exception to biotite Biotite melts at around 900°C (Gardien *et al*., 1995; Gardien *et al*., 2000). Knowing that biotite is not present in the mixed dikes thin sections they had to be at a temperature above 900°C but below a temperature of 1,000°C as quartz and other basaltic minerals are found. However, some EDS spectra have the elements for biotite but the crystals are too fine grained for EDS analysis. The elements for biotite are located in fine grained areas (below 5 μm), in turn, biotite crystals are not well defined. If these are biotite mica crystals this will decrease the mixed dikes temperature to be slightly below 900°C. Thus, making it just hot enough for the mixed dikes to form quenched margins.

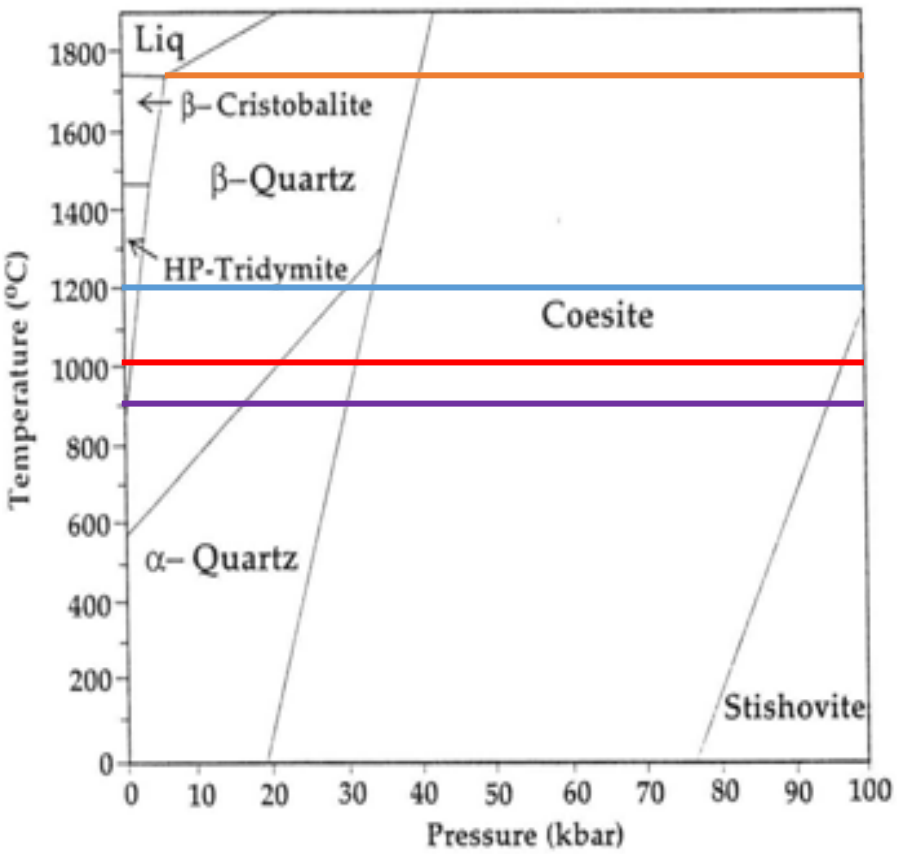

- Mica – 900 °C (Purple) (Gardien *et al.*, 2000; Gardien *et al., 1995)*
- Plagioclase – 1,099 °C (Red) (Branlund and Hofmeister, 2012)
- K-Feldspar - 1,200 °C (Blue) (Branlund and Hofmeister, 2012)
- Quartz – 1,710 °C (Orange) (Aasly *et al.*, 2007)

Figure 4. 4 Phase diagram of quartz highlighting the melting temperatures of mica, plagioclase, and K-Feldspar to illustrate the temperature of the dike.

There is no evidence of melting textures in mixing sample thin sections. Microscopic textures which identify partial melting are not present (Sawyer, 1999). In mixed samples quartz crystals are heavily fractured and there are no interlocking crystals in all sample. The exception to this is the siliciclastic lithics (Figure 4.5a). Plagioclases have zoning, twinning, and are fractured. K-feldspar have sieve textures in the center and a rim of plagioclase (Figure 4.5c). Thin sections show that GB basalt and siliciclastic crystals are breaking apart indicating that mixing is a violent process (Figure 4.5b). In siliciclastic sample thin section void spaces between the grains are visible. There is no embayment texture in any of the quartz or olivine which show the tachylyte ground mass through it (Figure 4.5d).

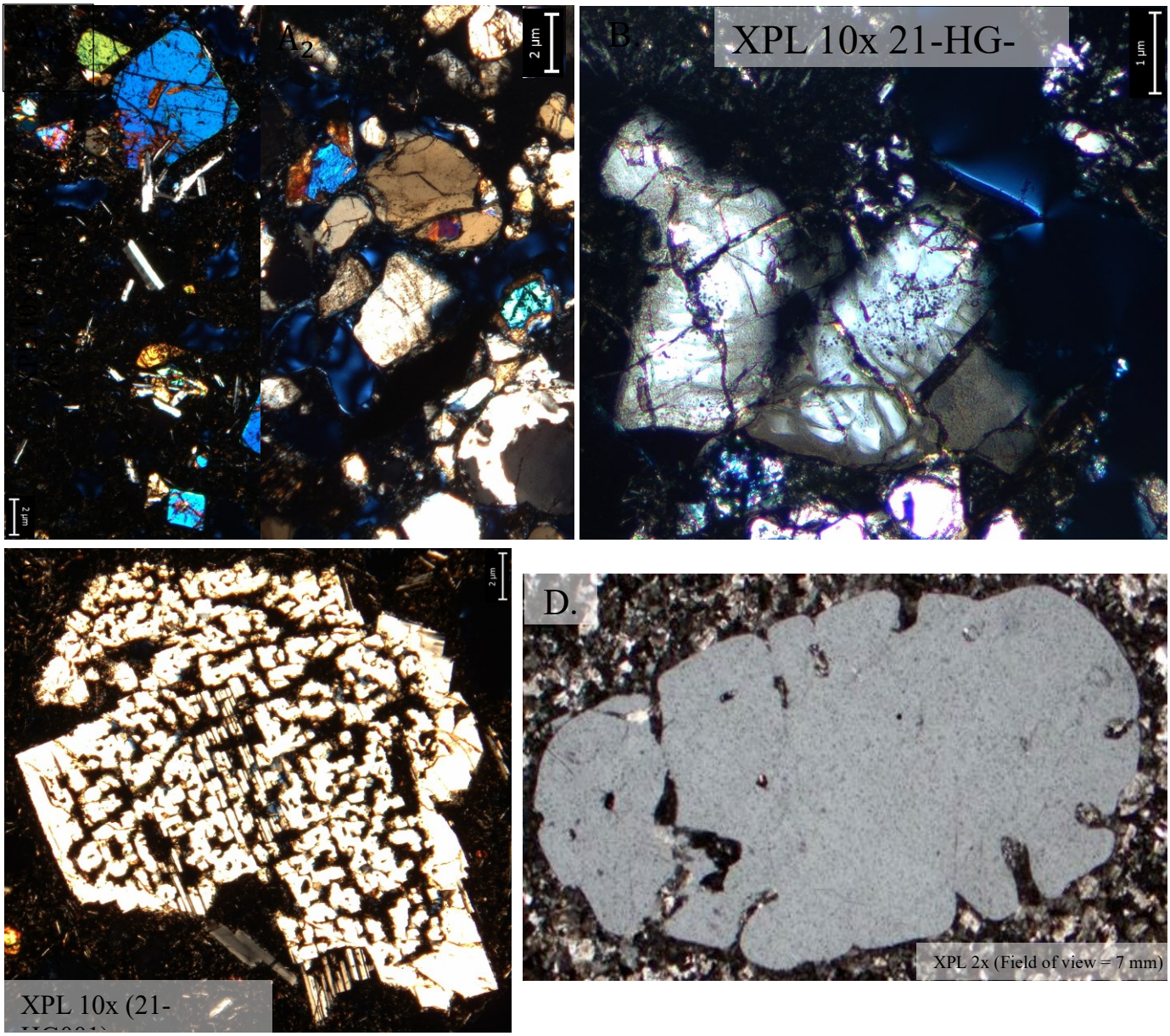

Figure 4. 5 Thin section images that illustrate the textures seen and an example of what would expected to be seen in the minerals from the rocks at Guffey Butte if there was melting. A_1) GB basalt sample 21-HG-002 shows subhedral to euhedral plagioclase and clinopyroxene crystals from a GB basalt. A_2) Homogenized sample 21-HG-024 shows subhedral to anhedral crystals of clinopyroxene. B) Homogenized sample 21-HG-025 showing subrounded quartz grains that are fractured. C) Plagioclase crystal in GB basalt sample 21-HG-001 that has a sieve texture. The plagioclase crystals surrounding it have a different texture. D) Quartz crystal that has embayment's which are indicative of melting. This sample is from Odenwaid, Germany and is used to demonstrate what would have been seen in melting occurred (Strekeisen, 2022).

4.3 Mixing through Kelvin-Helmholtz Instability

Guffey Butte is an optimal place to evaluate the characteristics and conditions of magma sediment mingling. The presence of water at the time of dike propagation is evident by the presence of phreatomagmatic deposits, peperites, a billowed dike, and thick quenched margins along dikes (0.5-2.5 cm). As the dikes propagate through wet siliciclastic sediment it could be expected for the interaction to pivot to be explosive. Guffey Butte maar is documentation of explosive interactions as GB basalt rose through the wet unconsolidated siliciclastic sediment. However, the GB basalt dikes and mixed dikes are preserved examples of non-explosive interactions in the same complex. The mixing observed in the non-explosive interactions may be the result of Kelvin-Helmholtz Instability (KHI). This instability occurs when there is differing velocities between the interface of two fluids of different densities resulting in shear velocity (Drazin, 2015). The boundaries between these fluids are broken and induces a wavy/oscillatory movement. The magma and the saturated siliciclastic sediment behave as fluids of differing densities (Buttner and Zimanwski, 1998; Skilling *et al*., 2002; and Befus *et al*., 2009). The magma propagating through the wet siliciclastic sediment has to be traveling at a velocity between 0.5-1 m/s to create the shear between the boundaries of the two fluids (Einarsson and Brandsdottir, 1980; Wilson and Head, 1981; Gudmundsson, 1984; Wilson and Head, 2002). The outer margin of the dikes began to cool rapidly, as evidence from the preserved quench margins, after the boundary is broken. Mixing must have occurred before the quenching of the margins to have quench margins within the homogenized section of dike (Figure4.6a-e).

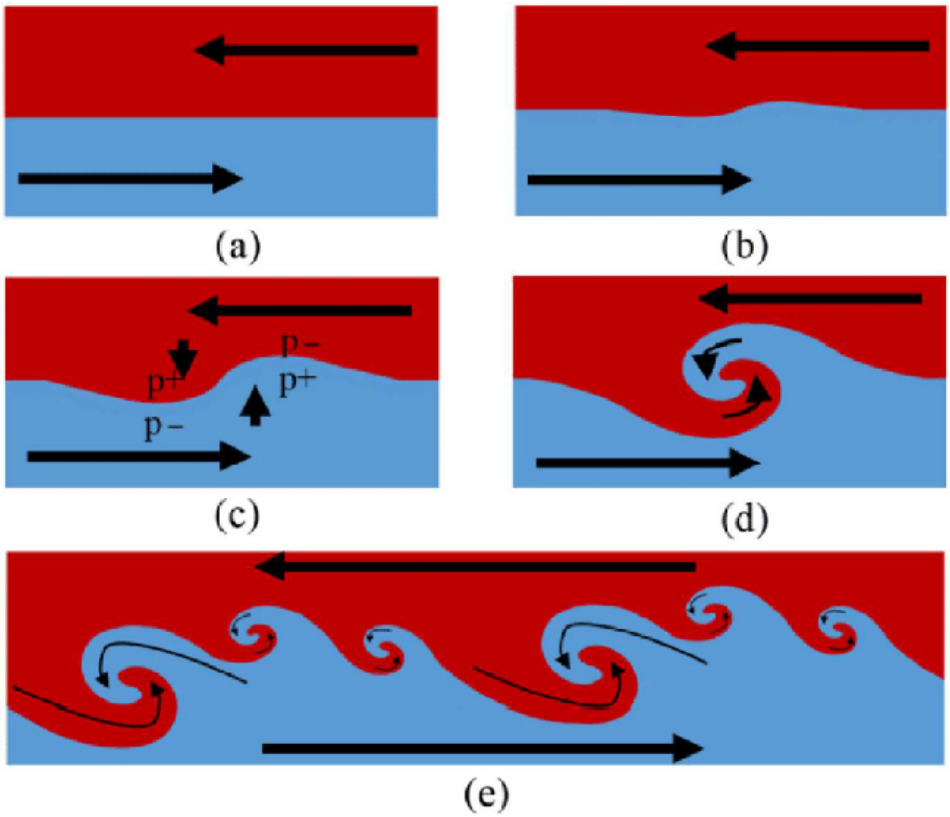

Figure 4. 6 A-E demonstrate the flow characteristics of KHI (Harwood *et al*., 2019; Lei *et al*., 2021). A) Two undisturbed fluids of differing densities moving in opposite directions separated by a thin vortex sheet that has a uniform velocity. B) A small perturbation causes the billowing of the vertex sheet. C) Regions of higher and lower pressure are a result of billowing as the velocities decrease and increases locally. Local changes in pressure increase the size of the billows and creates an unstable state. D) The layers begin to quickly fold over each other creating a vortex. E) Shows the range of wave sized that can occur within different lengths, with smaller billows/waved enveloping a larger one.

The wavy/oscillatory motion create as a result of the KHI could be what allows for the mixing between the magma and siliciclastic sediment to occur. As food die is added to water to show internal solitary waves the same principal can be applied to Guffey Butte with the propagation of magma into wet siliciclastic sediment. The different levels of mixing preserve the different stages of KHI depicted in figure 4.6. The least homogenized areas show the beginning of the HKI when the barrier of the two fluids has been disturbed (Figure

4.6 a-b). Moderately homogenized areas experience the wavy/oscillatory motion which is preserved in the texture of the dike as it cooled (Figure 4.6c-d). Banding textures are figure 4.6b, waves are figure 4.6c, and swirling is figure 4.6d. Homogenize areas have experienced the most KHI as there are no visible bands or swirls of GB basalt or siliciclastic sediment (Figure 4.6e). These changes occurred over distances of a few cm to meters (1m). A field image depicting this interaction can be seen in figure 4.7.

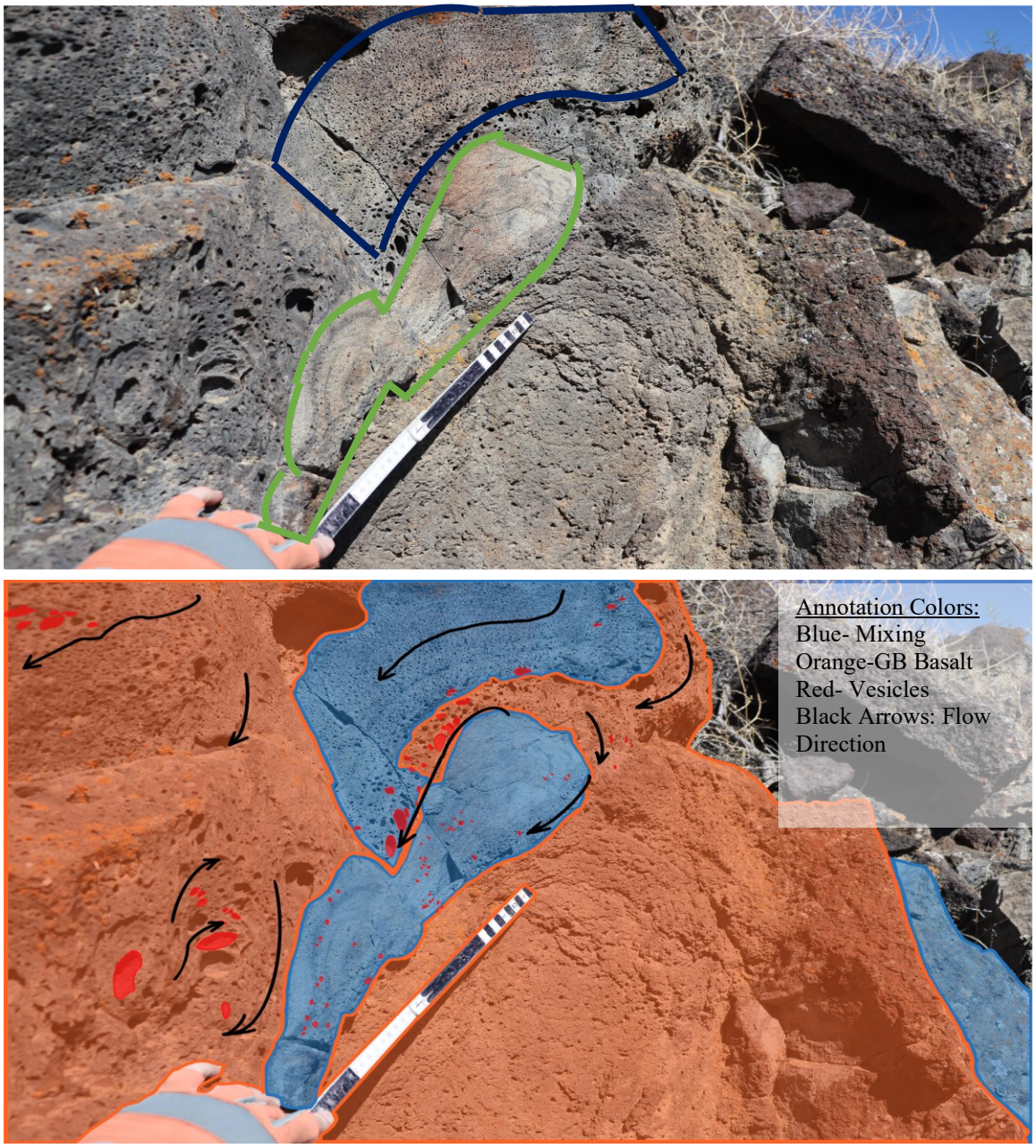

Figure 4. 7 Field image showing the preserved stages of KHI in the mixed dikes. A) The blue outline highlight figure 4.5 b-c. The green outline highlights figure 4.5 d-e. B) Field image annotated to demonstrate the potential direction of flow based on elongated vesicles that are subparallel to parallel to the transition from basalt to mixing in addition to the bands of basalt in the mixing.

CHAPTER 5. CONCLUSIONS

Magma sediment mingling is complex as there are many factors that influence its outcome. Guffey Butte is a prime place to study this as its dikes are made up of a range of intensity of magma sediment mingling. This study aims to break down the characteristics and conditions of the mixed dikes in a non-explosive environment through the use of multiple scales and techniques. Field measurements and observations were taken of exposed dikes at Guffey Butte in relations to the two main host sediments.

The studied dikes were emplaced sometime after the start of the eruption as they cut through pyroclastic material from earlier phases. GB basalts contain less lithics than mixed areas and samples. Both basaltic and siliciclastic minerals are preserved in mixed samples with exception to micas. From this it can be concluded that the temperature of the dike has to be above 900°C and below a temperature of 1,000°C as plagioclase and quartz are still present. There is no melting in the mixed dikes as proven by the lack of melting textures in thin section. However, this does not mean that melting does not occur in magma sediment mingling. 71 Gulch shows evidence of melting in its mixed samples (Bennis, 2019; Bennis and Graettinger, 2020). SEM-EDS analysis showed that there is no melting of minerals and confirmed the presence of k-feldspar in mixed samples with plagioclase rims which could be indicative of thermal disequilibrium.

Water is present at the time of the dike's propagation as the quench margins of the dikes are preserved on GB basalt dikes and on the southern portion of the mixed dike. The margins of the mixed dike contain siliciclastic sediment and have columnar cracks. Columnar joints made fully homogenized magma and sediment are evidence of the rapid heating and cooling of sediment.

The dikes show mingling can be diverse and the style over a spatial area is not systematic. Magma penetrates through wet unconsolidated siliciclastic sediment and due to their differing buoyancies mixing is then initiated through Kelvin-Helmholtz Instability. Levels of homogenization indicate the level of instability in the dike. Elongated vesicles show preferential orientation in the field and in thin section serving as supportive evidence of flow during dike propagation. Vesicle elongation is sub-parallel to parallel to the margins of the dike. In addition, elongated vesicles are sun-parallel to parallel to the bands and swirls preserved in moderately homogenized mixing.

This study serves as a framework for any future work carried out on the mixed dike of Guffey Butte. The maar deposits are more complex than previous field descriptions have captured. Thus, there is additional work left to be done to understand the eruptions. In terms of mixing future work can be done on magma rheology, depth required to mix, pressure, and water quantity be a potential focus of future work. As 71 Gulch presents melting in its mixed samples a comparison between its samples and those of Guffey Butte should be carried out once a better understanding of Guffey Butte is obtained.

The surface of the Earth is covered in unconsolidated siliciclastic martial that has the possibility of saturated. In addition, magma has the potential to interact with water in multiple forms, such as glaciers, groundwater, and large bodies of water. Therefore, it is bound for magma to interact with unconsolidated siliciclastic material at some point in time leading to the possibility for eruptions of varying degrees of explosivity. The mixed dikes illustrate a way in which magma migrates to the surface in a non-explosive manner while in a maar which was created explosively. Continuing research in explosive magma-water interactions is critical as it provides a better understanding of the necessary conditions for varying degrees of

explosivity. In turn this knowledge can improve monitoring and mitigation of active or potential phreatomagmatic eruptions.

APPENDIX

Tables

Sample ID	Lithology	Lat	Long	Elevation	Depth (m)	WP	Level of Homoginezation	Distance from Mixing Dike (m)	**Thin Section**	**SEM-EDS**	**Geochemistry (XRF and ICP-MS)**
21-HG-029	Pyroclastic	43.2894	-116.5384	830.69	-58.73	GB036		89			
21-HG-023	Pyroclastic	43.2897	-116.5389	849.56	-77.60	GB032		75	x		
21-HG-011	Pyroclastic	43.2904	-116.5373	836.84	-64.89	GB014		29			
21-HG-037	Pyroclastic	43.2904	-116.5373	831.07	-59.12	GB044		23	x		
21-HG-035	Sandstone	43.2908	-116.5376	796.50	-24.55	GB042		45	x	x	
21-HG-030	Silt stone	43.2902	-116.5383	808.68	-36.73	GB038		13	x		
21-HG-031	Sandstone	43.2902	-116.5383	808.68	-36.73	GB038		13	x	x	
21-HG-001	Basalt	43.2917	-116.5367	858.72	-86.77	GB005		168	x	x	
21-HG-002	Basalt	43.2917	-116.5367	858.72	-86.77	GB005		168	x		
21-HG-034	Basalt	43.2891	-116.5377	842.68	-70.73	GB040		142	x		
21-HG-036	Basalt	43.2913	-116.5376	811.66	-39.71	GB043		96	x		x
21-HG-027	Basalt	43.2894	-116.5385	827.25	-55.30	GB035		90	x		x
21-HG-028	Basalt	43.2894	-116.5384	830.69	-58.73	GB036		89	x		
21-HG-022	Basalt	43.2897	-116.5389	849.56	-77.60	GB032		71	x	x	x
21-HG-021	Basalt	43.2897	-116.5389	849.56	-77.60	GB032		71	x		x
21-HG-019	Basalt	43.2902	-116.5389	832.82	-60.87	GB022		40	x		
21-HG-020	Basalt	43.2900	-116.5387	828.98	-57.03	GB029		32	x		
21-HG-003	Basalt	43.2904	-116.5373	836.84	-64.89	GB007		29	x		
21-HG-004	Basalt	43.2904	-116.5373	836.84	-64.89	GB007		29	x	x	
21-HG-005	Basalt	43.2904	-116.5375	828.85	-56.90	GB011		12	x		
21-HG-013	Basalt	43.2904	-116.5378	809.50	-37.55	GB018		17	x	x	
21-HG-006	Least Homogenized	43.2904	-116.5376	823.39	-51.44	GB013	Least		x	x	
21-HG-018	Least Homogenized	43.2902	-116.5384	815.59	-43.64	GB021	Least		x		
21-HG-014	Least Homogenized	43.2904	-116.5378	809.50	-37.55	GB018	Least		x		
21-HG-012	Least Homogenized	43.2904	-116.5378	809.50	-37.55	GB018	Least		x	x	
21-HG-017	Least Homogenized	43.2902	-116.5382	799.17	-27.21	GB020	Least		x	x	
212-HG-009	Moderate Homoginezation	43.2904	-116.5376	828.80	-56.85	GB016			x	x	
21-HG-032 (a,b)	Moderate Homoginezation	43.2904	-116.5373	831.07	-59.12	GB008	Moderate		x		
21-HG-015	Moderate Homoginezation	43.2903	-116.5379	811.59	-39.64	GB019	Moderate		x	x	
21-HG-010	Moderate Homoginezation	43.2903	-116.5378	810.02	-38.06	GB017	Moderate		x	x	
21-HG-024	Homogenized	43.2897	-116.5389	849.56	-77.60	GB032	Homogenized	71	x		
21-HG-025	Homogenized	43.2897	-116.5389	849.56	-77.60	GB032	Homogenized	71	x		
21-HG-026	Homogenized	43.2897	-116.5389	849.56	-77.60	GB032	Homogenized	71	x		
21-HG-033	Homogenized	43.2904	-116.5373	836.84	-64.89	GB007	Homogenized		x		x
21-HG-008	Homogenized	43.2904	-116.5376	817.96	-46.01	GB015	Homogenized		x	x	
21-HG-007	Homogenized	43.2903	-116.5376	815.73	-43.78	GB014	Homogenized		x		
21-HG-016	Homogenized	43.2903	-116.5379	811.59	-39.64	GB019	Homogenized		x	x	x

All samples N numbers: Plagolcase, Quartz, Rock Fragments, and Other					
Sample ID	**Lithology**	**Pl**	**Qtz**	**Rock Fragments**	**Other**
21-HG-023	Scoria	36	35	0	144
21-HG-037	Lapilli Tuff	124	50	0	42
21-HG-030	Siltstone	20	294	0	4
21-HG-031	Sandstone	43	726	0	54
21-HG-035	Sandstone	27	839	0	36
21-HG-005	Basalt	356	20	0	15
21-HG-013	Basalt	207	146	8	12
21-HG-003	Basalt	231	153	2	9
21-HG-004	Basalt	211	105	2	27
21-HG-020	Basalt	193	146	8	31
21-HG-019	Basalt	33	7	0	81
21-HG-021	Basalt	410	32	0	155
21-HG-022	Basalt	370	32	0	240
21-HG-028	Basalt	137	102	0	26
21-HG-027	Basalt	317	3	0	81
21-HG-036	Basalt	262	28	1	57
21-HG-034	Basalt	238	72	0	53
21-HG-001	Basalt	532	0	0	99
21-HG-002	Basalt	425	2	0	83
21-HG-006	Least Homogenized	49	190	1	27
21-HG-018	Least Homogenized	20	291	1	23
21-HG-012	Least Homogenized	37	359	0	8
21-HG-014	Least Homogenized	199	406	0	13
21-HG-017	Least Homogenized	3	173	0	30
21-HG-032a	Moderate Homogenization	127	86	1	13
212-HG-009	Moderate Homogenization	4	81	0	28
21-HG-015	Moderate Homogenization	25	464	0	33
21-HG-010	Moderate Homogenization	34	438	0	8
21-HG-024	Homogenized	35	595	0	96
21-HG-025	Homogenized	13	405	0	55
21-HG-026	Homogenized	9	428	0	30
21-HG-033	Homogenized	42	776	0	37
21-HG-007	Homogenized	179	190	0	16
21-HG-008	Homogenized	29	284	0	6

Sample	Description	Petrography
21-HG-001	GB Basalt (Dike)	No preferential alignment of phenocrysts in the groundmass of plagioclase microlites. Tachylyte makes up a small section (10%). Vesicles are elongated and coalesced (15%). Euhedral plagioclase (40%), euhedral to subhedral clinopyroxene (20%), and euhedral to subhedral olivine (25%). Plagioclase with sieve texture. Oxides in crystals. Glomerocrysts measure ~0.025 mm consist of subhedral clinopyroxene.
21-HG-002	GB Basalt (Dike)	No preferential alignment of phenocrysts in the groundmass plagioclase microlites. Small plagioclase crystals make up the groundmass. Vesicles are elongated and coalesced (15%). Euhedral plagioclase (45%), euhedral to subhedral clinopyroxene (20%), and euhedral to subhedral olivine (25%). Plagioclase with sieve texture. Oxides in crystals.
21-HG-003	GB Basalt	Tachylyte groundmass with several small crystals difficult to identify microscopically. Plagioclase crystals with brown rims and white cores. Rock fragments measure between 20-80 mm. Vesicles make up no more than 5% and show no fill. Euhedral to subhedral plagioclase (55%), euhedral to subhedral clinopyroxene (6%), and euhedral to subhedral olivine (5%). Sporadic anhedral quartz crystals.
21-HG-004	GB Basalt (Dike)	Tachylyte groundmass (90%) with elongated to coalesced vesicles (10%). Euhedral to subhedral plagioclase (75%), subhedral clinopyroxene (4%), and subhedral olivine (8%). Vesicles are irregularly shaped and have very minute amounts of fill by secondary minerals. Rock fragment measure between 0.01-.034 mm.
21-HG-005	GB Basalt (Dike with siliciclastic material running through ~30 cm)	Tachylyte groundmass (92%) with sporadic sideromelane (8%).

		Vesicles are subrounded to coalesced and are lined with secondary minerals. No vesicles are completely filled. There is no preferential alignment of phenocrysts. Subhedral plagioclase (35%), subhedral to euhedral clinopyroxene (5%), and subhedral to euhedral olivine (5%). Sporadic quartz crystals measuring between 0.005-0.030 mm.
21-HG-006	Least Homogenized (Dike)	Tachylyte groundmass (90%) with subrounded vesicles (10%). Vesicles are subrounded-rounded and are lined with secondary minerals. No vesicles are completely filled. Plagioclase crystals with dark to light brown rims. Crystal size changes from crystals between 0.003-0.03 mm to crystals less than 0.003. Anhedral to subhedral plagioclase (40%), anhedral quartz (48%), subhedral clinopyroxene (7%), and anhedral to subhedral olivine (5%). Crystals are fractured and rounded to angular.
21-HG-007	Homogenized (Dike)	Tachylyte groundmass (94%) with vesicles that are subrounded to coalesced (6%). Rock fragments range in size from 0.01-0.03 mm. Plagioclase crystals with light to dark brown rims. Anhedral to subhedral plagioclase (36%), anhedral quartz (54%), subhedral clinopyroxene (5%), and subhedral olivine (5%).
21-HG-008	Homogenized (Dike with margin)	Tachylyte groundmass (88%) with vesicles that are subrounded to coalesced (12%). Vesicles are either fully or partially lined with secondary minerals. None of the vesicles are completely filled. Subhedral plagioclase (37%), anhedral quartz (53%), anhedral to subhedral clinopyroxene (4%), and subhedral olivine (6%). Crystals are highly fractured and angular to rounded.

21-HG-009	Moderate Homogenization (Dike with margin columnar joints)	Tachylyte ground mass (92%) with vesicles (8%) that are parallel to subparallel to the margin preserved. Vesicles are subrounded to elongated and have secondary minerals. Calcite fills several vesicles. Subhedral plagioclase (10%), anhedral quartz (15%), anhedral to subhedral clinopyroxene (4%), subhedral olivine (5%). Bands of varying thickness (0.01-0.04 mm) and color are visible.
21-HG-010	Moderate Homogenization (Dike)	Tachylyte groundmass (94%) with vesicles (6%) that subrounded to coalesced. Vesicles are lined with secondary minerals but are not completely filled. Rock fragments range in size from 0.005-0.05 mm. Subhedral plagioclase (35%), anhedral quartz (40%), subhedral clinopyroxene (4%), and subhedral olivine (6%). Crystals are fractured and show no evidence of embayment.
21-HG-012	Least Homogenized (Dike)	Tachylyte groundmass (92%) with vesicles (8%) that are subrounded to elongated. Vesicles are lined with secondary minerals but are not completely filled. Subhedral to euhedral plagioclase (%30), anhedral quartz (65%), subhedral clinopyroxene (2%), and subhedral olivine (3%).
21-HG-013	GB Basalt (Dike)	Tachylyte groundmass with vesicles that are angular to subrounded. Vesicles are also coalesced and have secondary mineral lining the interior. None a completely filled. Rock fragments average in size between 0.005-0.04 mm. Subhedral to anhedral plagioclase (73%), anhedral quartz (17%), subhedral to anhedral clinopyroxene (4%), and subhedral to anhedral olivine (6%).
21-HG-014	Least Homogenized (Dike)	Tachylyte groundmass (94%) with vesicles (6%) that are subrounded. Several plagioclase crystals with light to dark brown rims.

		Subhedral to euhedral plagioclase (30%), anhedral quartz (62%), subhedral clinopyroxene (3%), subhedral olivine (5%). Several crystal edges are rounded or jagged. A majority of crystals are small (no larger than 0.05 mm) with sporadic ones between 0.005-0.010 mm.
21-HG-015	Moderately Homogenized (Dike)	Tachylyte groundmass (80%) with vesicles (20%)that are rounded to subrounded. Vesicles are lined with secondary minerals and are none are completely filled. Subhedral to anhedral plagioclase (25%), anhedral quartz (67%), subhedral clinopyroxene (3%), and subhedral olivine (5%).
21-HG-016	Homogenized	Tachylyte groundmass with minimal vesicles (3%). Subhedral plagioclase (29%), anhedral quartz (64%), subhedral clinopyroxene (3%), and subhedral olivine (4%). The concentration of crystals through the sample.
21-HG-017	Least Homogenized	Tachylyte groundmass with vesicles (%) that are subrounded to coalesced. Vesicles are lined with secondary minerals and are not fully filled. Plagioclase crystals with light to dark brown rims. Rock fragments range in size from 0.005-0.03 mm. Subhedral to anhedral plagioclase (36%), anhedral quartz (54%), subhedral clinopyroxene (4%), and subhedral olivine (6%). Several crystals have been bisected or have angular chucks missing.
21-HG-018	Least Homogenized	Tachylyte groundmass (95%) with subrounded to rounded vesicles (5%). Vesicles have a lining of secondary mineral fill and none are fully filled. Rock fragments range in size from 0.005-0.034 mm. Plagioclase crystals have light to dark brown rims, and some have a similar colored core.

		Subhedral to euhedral plagioclase (31%), anhedral quartz (63%), anhedral to subhedral clinopyroxene (3%), and subhedral olivine (3%).
21-HG-019	GB Basalt (Margin in pyroclastic material)	Tachylyte groundmass (85%) with vesicles (15%) that are subrounded and coalesced. Vesicles are lined with secondary minerals and none are fully filled. Plagioclase crystals with light to dark brown rims and have sieve textures. Subhedral to euhedral plagioclase (84%), anhedral quartz (10%), subhedral clinopyroxene (2%), and subhedral olivine (4%).
21-HG-020	GB Basalt	Tachylyte groundmass (%) with subrounded to coalesced vesicles (%). Vesicles are lined with secondary minerals but are not fully filled. Rock fragments measure range in size from 0.005-0.08 mm. Plagioclase crystals with brown rims and sieve texture. Subhedral to euhedral plagioclase (78%), anhedral quartz (12%), subhedral to euhedral clinopyroxene (4%), and subhedral to euhedral olivine (6%).
21-HG-021	GB Basalt	Tachylyte groundmass (75%) with subrounded to coalesced vesicles (25%). Vesicles are lined with secondary minerals. The ground mass is also made up of microlites of plagioclase. Glomerocrysts range in size from 0.01-0.03 mm. Euhedral plagioclase (84%), anhedral quartz (3%), subhedral to euhedral clinopyroxene (5%), and subhedral to euhedral olivine (8%).
21-HG-022	GB Basalt	Tachylyte groundmass (%) with subrounded to coalesced vesicles (%). Vesicles are lined with secondary minerals. Euhedral plagioclase (77%), anhedral quartz (5%), euhedral clinopyroxene (8%), euhedral olivine (10%).
21-HG-023	Scoria	Tachylyte groundmass (%) with vesicles (%) that are rounded to subrounded. Several are

		coalesced and have secondary mineral fill lining the vesicle. Plagioclase with sieve textures. Euhedral plagioclase (45%), anhedral quartz (10%), subhedral to euhedral clinopyroxene (17%), subhedral to euhedral olivine (29%).
21-HG-024	Homogenized (Columnar Joints)	Tachylyte groundmass (95%) with sporadic vesicles (5%) that are rounded to subrounded. Plagioclase with light to dark brown rims and several with sieve textures. Subhedral to euhedral plagioclase (30%), anhedral quartz (52%), subhedral clinopyroxene (8%), subhedral olivine (10%).
21-HG-025	Homogenized (Columnar Joints)	Tachylyte groundmass (85%) with subrounded vesicles (15%). Rock fragments range in size between 0.005-0.20mm. Subhedral to euhedral plagioclase (30%), anhedral quartz (52%), subhedral clinopyroxene (8%), subhedral olivine (10%).
21-HG-026	Homogenized (Columnar Joints)	Tachylyte groundmass with subrounded to coalesced vesicles. Vesicles are lined with secondary minerals but not completely filled. Plagioclase crystals have light to dark brown rims. Subhedral to euhedral plagioclase (34%), anhedral quartz (53%), subhedral to euhedral clinopyroxene (5%), subhedral to euhedral olivine (8%).
21-HG-027	GB Basalt (Billowed Dike)	Tachylyte groundmass with microlites of plagioclase. Plagioclase microlites have no preferred orientation. Subhedral to euhedral plagioclase (75%), anhedral quartz (7%), subhedral to euhedral clinopyroxene (8%), subhedral to euhedral olivine (10%).
21-HG-028	GB Basalt	Tachylyte groundmass (97%) with sporadic vesicles (3%) that are subrounded. Subhedral to euhedral plagioclase (42%), anhedral quartz (20%), subhedral clinopyroxene (8%), and subhedral olivine (10%).

21-HG-030	Silt Stone	Moderately sorted with microcrystalline quartz making up the groundmass (65%). Quartz crystals are angular to subrounded (62%). Plagioclase crystals are angular to subangular (35%). Olivine crystals are subangular to subrounded (3%).
21-HG-031	Sandstone	Well sorted with a groundmass composed of microcrystalline quartz (25%). Angular to subangular plagioclase (30%). Rounded to subangular quartz (66%). Angular to subrounded olivine (2%) and clinopyroxene (2%).
21-HG-032a	Moderate Homogenization	Tachylyte groundmass (85%) with vesicles (15%) that are that are subrounded to coalesced. Rock fragments measure between 0.005-0.04 mm. Plagioclase crystals have light to dark brown rims with sieve textures. Subhedral to euhedral plagioclase (25%), anhedral quartz (68%) subhedral to euhedral clinopyroxene (3%), and subhedral to euhedral olivine (4%).
21-HG-032b	Moderate Homogenization	Tachylyte groundmass (95%) with vesicles (5%) that are subrounded to coalesced. Subhedral to euhedral plagioclase (25%), anhedral quartz (45%), subhedral clinopyroxene (2%), and subhedral olivine (3%).
21-HG-033	Homogenized	Tachylyte groundmass (90%) with vesicles (10%) that are subrounded to coalesced. Vesicles are lined with secondary minerals and several are almost completely filled. Subhedral to euhedral plagioclase (30%), anhedral quartz (63%), subhedral clinopyroxene (3%), and subhedral olivine (4%).
21-HG-034	GB Basalt	Tachylyte groundmass (80%) with vesicles (20%) that are rounded to subrounded. Vesicles are coalesced and are lined with secondary minerals. Subhedral to euhedral plagioclase (34%), anhedral quartz (56%), subhedral to euhedral clinopyroxene (4%), and subhedral to euhedral olivine (6%).

21-HG-035	Sandstone	Well sorted with a microcrystalline quartz groundmass. Subhedral to euhedral plagioclase (20%), anhedral quartz (71%), subhedral clinopyroxene (3%), subhedral olivine (5%), euhedral mica (1%).
21-HG-036	GB Basalt	Tachylyte groundmass (%) with sporadic vesicles (4%) that are subrounded to rounded. Rock fragments measure between 0.01-0.04 mm. Plagioclase crystals have light to dark brown rims. Euhedral plagioclase (76%), anhedral quartz (5%), subhedral to euhedral clinopyroxene (7%), and subhedral to euhedral olivine (12%).
21-HG-037	Lapilli Tuff	Tachylyte groundmass (75%) with vesicles (25%) that are rounded to subrounded and coalesced. Rock fragments measured between 0.01-0.03 mm. Subhedral to euhedral plagioclase (72%), anhedral quartz (17%), subhedral to euhedral clinopyroxene (4%), and subhedral to euhedral olivine (7%).

SEM-EDS Spectra Graphs

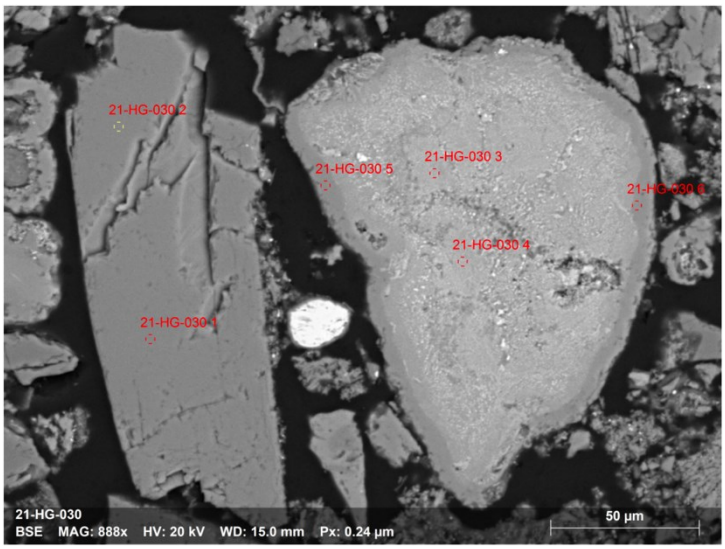

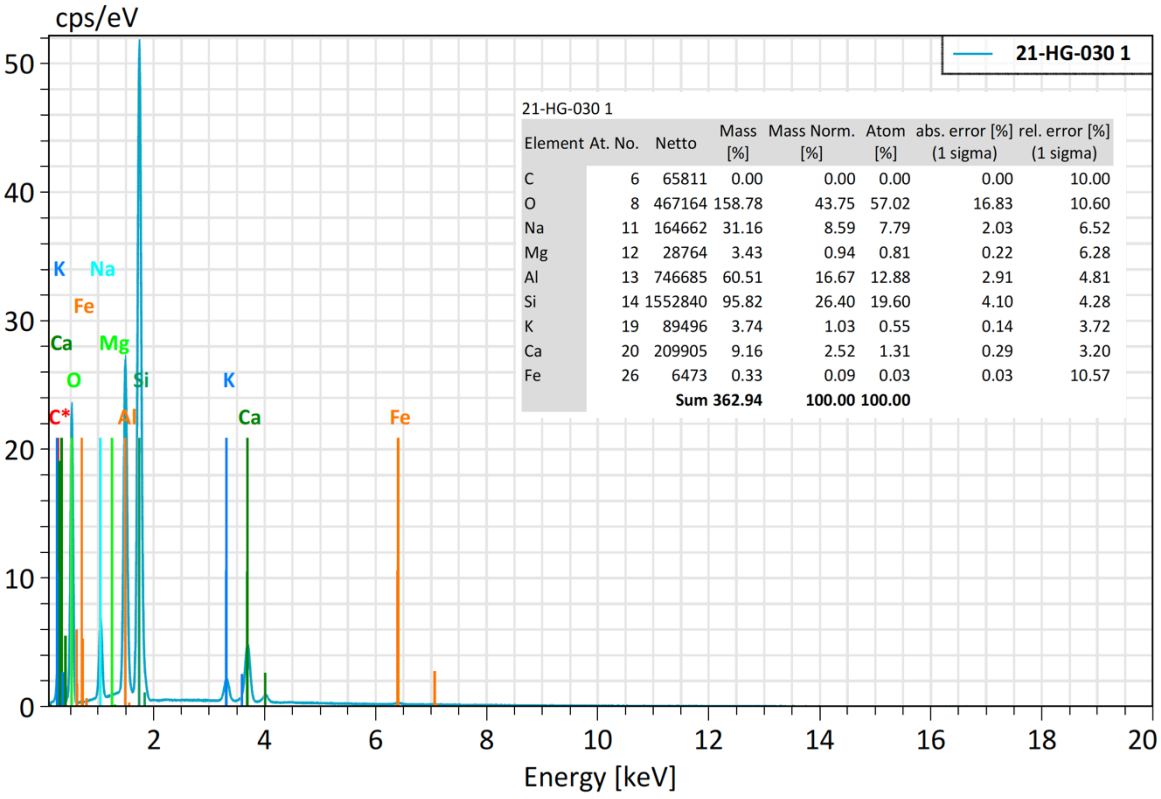

21-HG-030 1

Element	At. No.	Netto	Mass [%]	Mass Norm. [%]	Atom [%]	abs. error [%] (1 sigma)	rel. error [%] (1 sigma)
C	6	65811	0.00	0.00	0.00	0.00	10.00
O	8	467164	158.78	43.75	57.02	16.83	10.60
Na	11	164662	31.16	8.59	7.79	2.03	6.52
Mg	12	28764	3.43	0.94	0.81	0.22	6.28
Al	13	746685	60.51	16.67	12.88	2.91	4.81
Si	14	1552840	95.82	26.40	19.60	4.10	4.28
K	19	89496	3.74	1.03	0.55	0.14	3.72
Ca	20	209905	9.16	2.52	1.31	0.29	3.20
Fe	26	6473	0.33	0.09	0.03	0.03	10.57
		Sum	362.94	100.00	100.00		

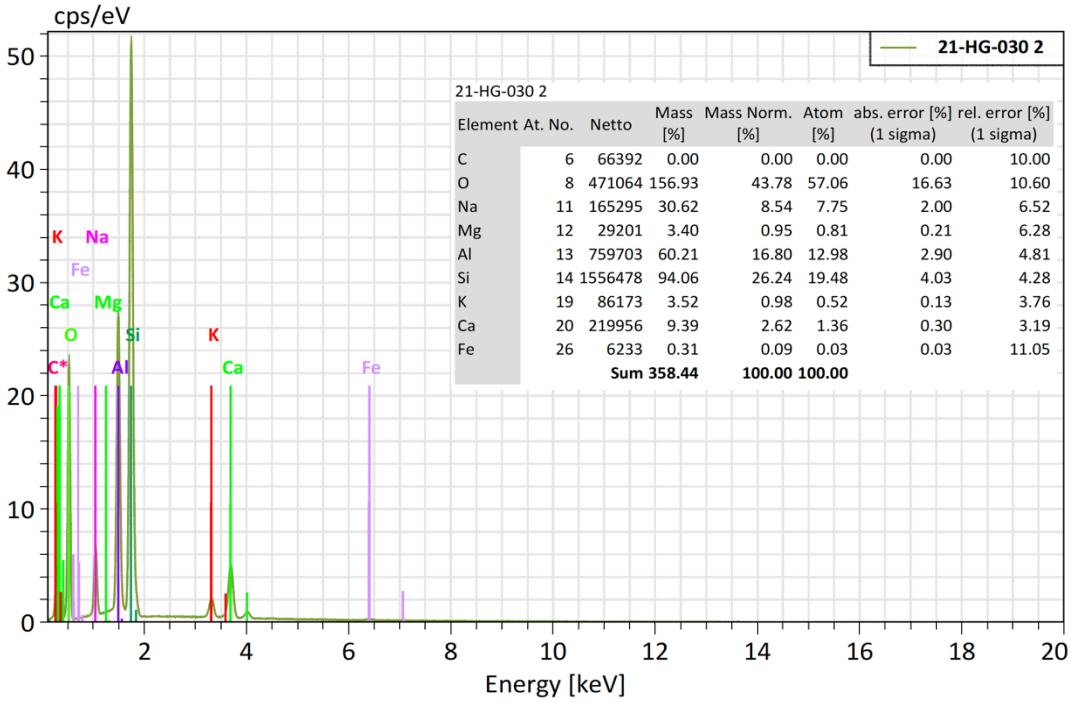

21-HG-030 2

Element	At. No.	Netto	Mass [%]	Mass Norm. [%]	Atom [%]	abs. error [%] (1 sigma)	rel. error [%] (1 sigma)
C	6	66392	0.00	0.00	0.00	0.00	10.00
O	8	471064	156.93	43.78	57.06	16.63	10.60
Na	11	165295	30.62	8.54	7.75	2.00	6.52
Mg	12	29201	3.40	0.95	0.81	0.21	6.28
Al	13	759703	60.21	16.80	12.98	2.90	4.81
Si	14	1556478	94.06	26.24	19.48	4.03	4.28
K	19	86173	3.52	0.98	0.52	0.13	3.76
Ca	20	219956	9.39	2.62	1.36	0.30	3.19
Fe	26	6233	0.31	0.09	0.03	0.03	11.05
			Sum 358.44	100.00	100.00		

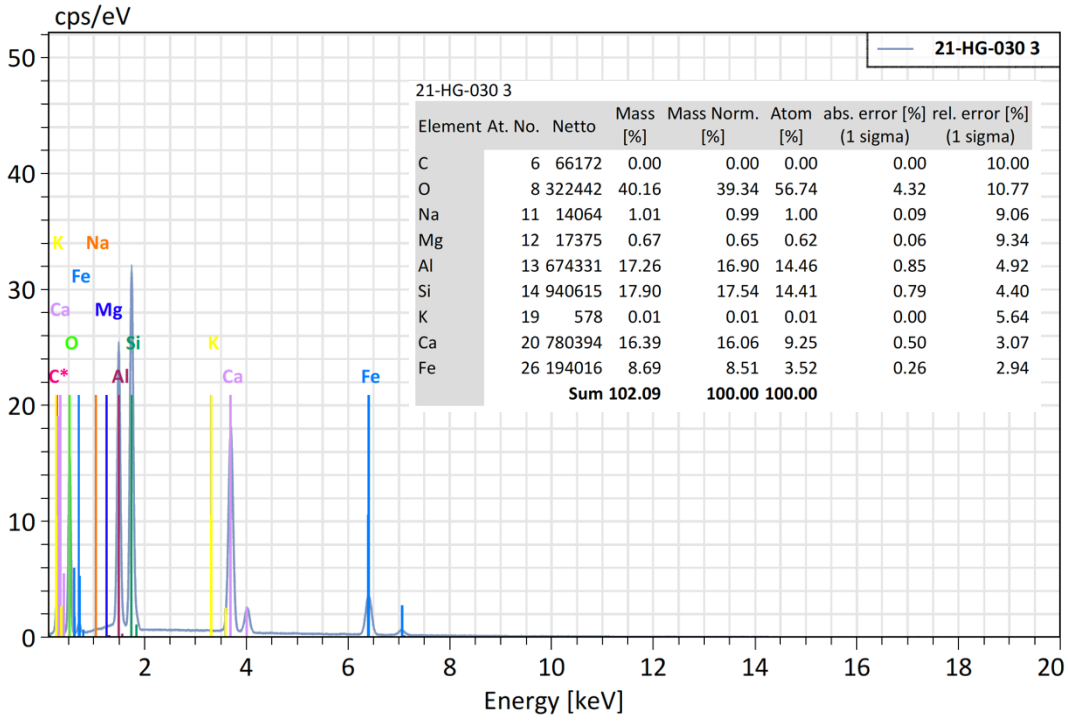

21-HG-030 3

Element	At. No.	Netto	Mass [%]	Mass Norm. [%]	Atom [%]	abs. error [%] (1 sigma)	rel. error [%] (1 sigma)
C	6	66172	0.00	0.00	0.00	0.00	10.00
O	8	322442	40.16	39.34	56.74	4.32	10.77
Na	11	14064	1.01	0.99	1.00	0.09	9.06
Mg	12	17375	0.67	0.65	0.62	0.06	9.34
Al	13	674331	17.26	16.90	14.46	0.85	4.92
Si	14	940615	17.90	17.54	14.41	0.79	4.40
K	19	578	0.01	0.01	0.01	0.00	5.64
Ca	20	780394	16.39	16.06	9.25	0.50	3.07
Fe	26	194016	8.69	8.51	3.52	0.26	2.94
			Sum 102.09	100.00	100.00		

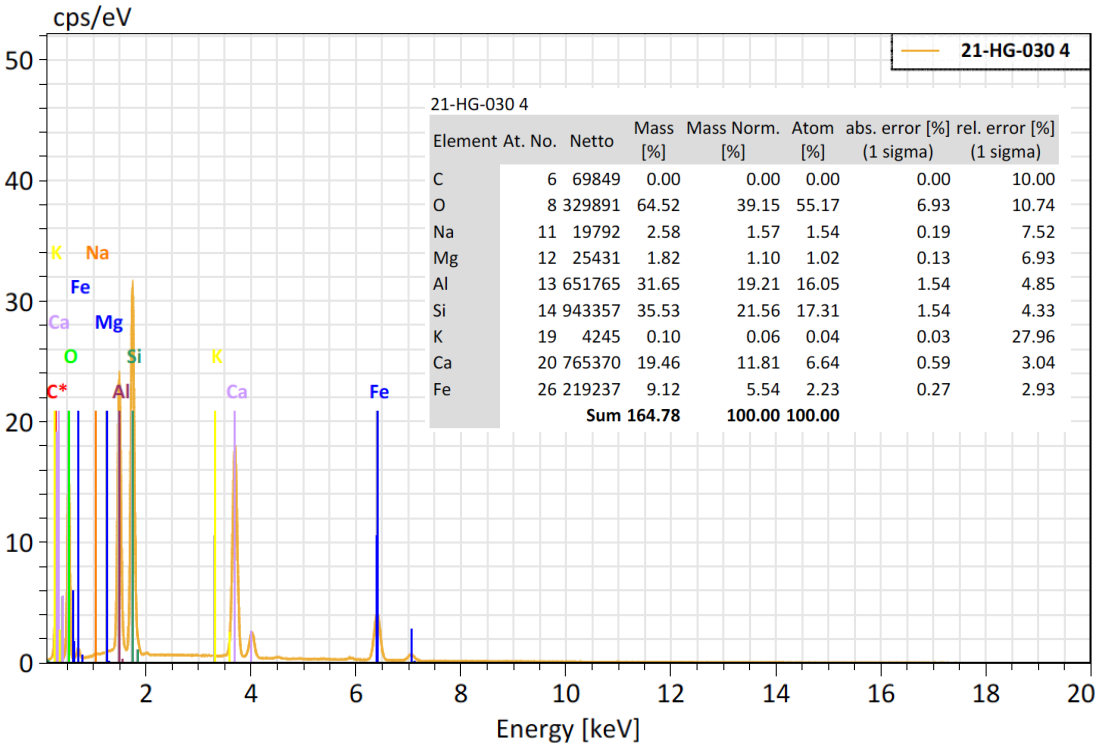

21-HG-030 4

Element	At. No.	Netto	Mass [%]	Mass Norm. [%]	Atom [%]	abs. error [%] (1 sigma)	rel. error [%] (1 sigma)
C	6	69849	0.00	0.00	0.00	0.00	10.00
O	8	329891	64.52	39.15	55.17	6.93	10.74
Na	11	19792	2.58	1.57	1.54	0.19	7.52
Mg	12	25431	1.82	1.10	1.02	0.13	6.93
Al	13	651765	31.65	19.21	16.05	1.54	4.85
Si	14	943357	35.53	21.56	17.31	1.54	4.33
K	19	4245	0.10	0.06	0.04	0.03	27.96
Ca	20	765370	19.46	11.81	6.64	0.59	3.04
Fe	26	219237	9.12	5.54	2.23	0.27	2.93
		Sum	**164.78**	**100.00**	**100.00**		

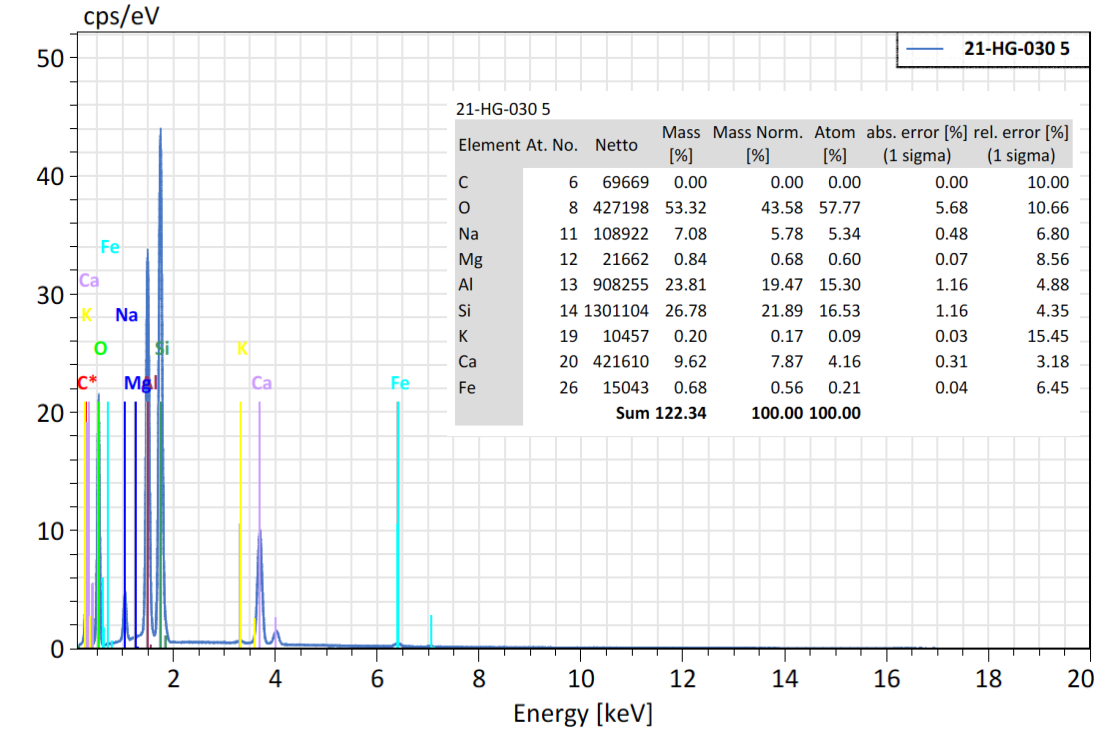

21-HG-030 5

Element	At. No.	Netto	Mass [%]	Mass Norm. [%]	Atom [%]	abs. error [%] (1 sigma)	rel. error [%] (1 sigma)
C	6	69669	0.00	0.00	0.00	0.00	10.00
O	8	427198	53.32	43.58	57.77	5.68	10.66
Na	11	108922	7.08	5.78	5.34	0.48	6.80
Mg	12	21662	0.84	0.68	0.60	0.07	8.56
Al	13	908255	23.81	19.47	15.30	1.16	4.88
Si	14	1301104	26.78	21.89	16.53	1.16	4.35
K	19	10457	0.20	0.17	0.09	0.03	15.45
Ca	20	421610	9.62	7.87	4.16	0.31	3.18
Fe	26	15043	0.68	0.56	0.21	0.04	6.45
		Sum	**122.34**	**100.00**	**100.00**		

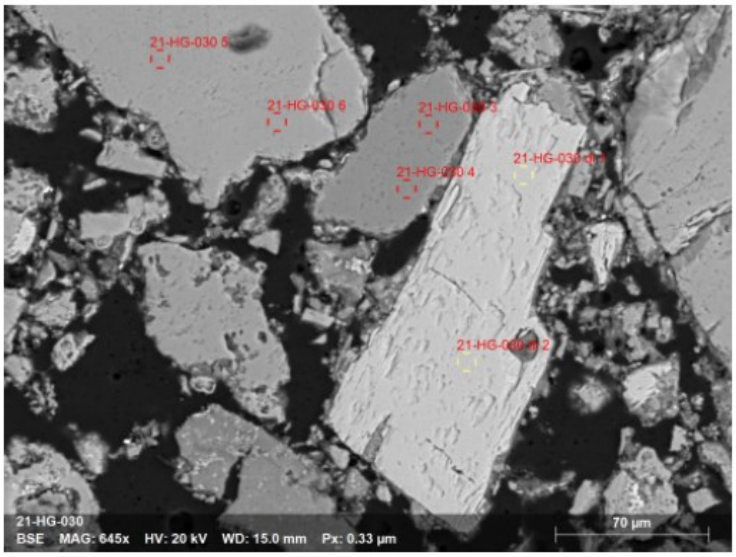

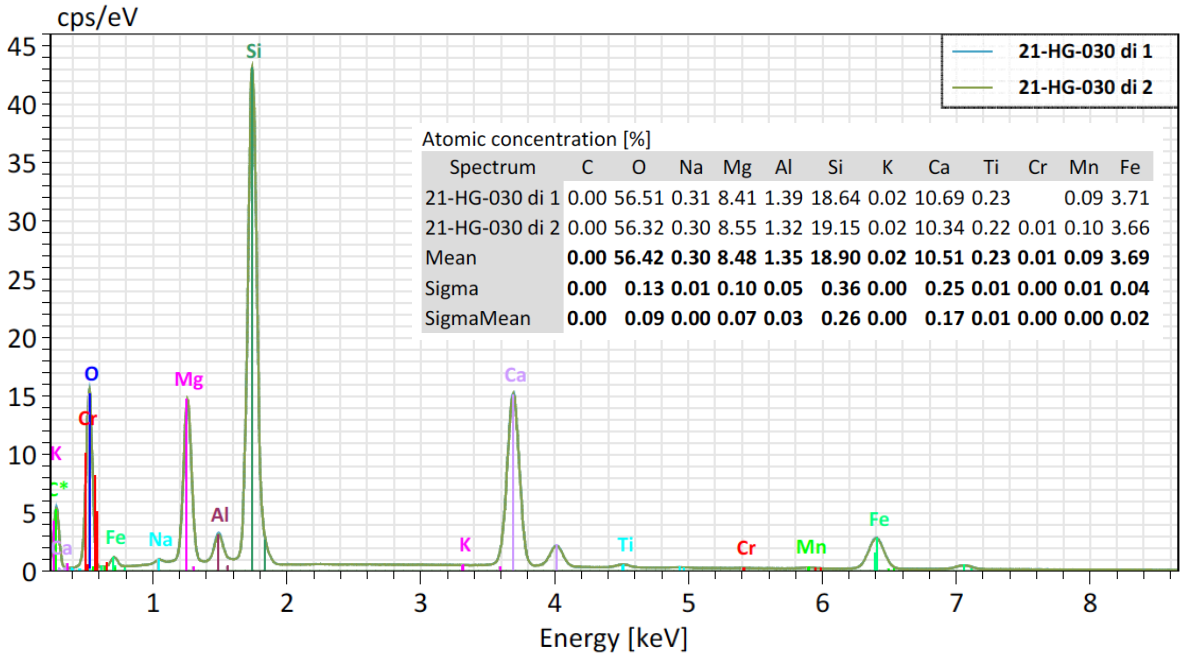

Atomic concentration [%]

Spectrum	C	O	Na	Mg	Al	Si	K	Ca	Ti	Cr	Mn	Fe
21-HG-030 di 1	0.00	56.51	0.31	8.41	1.39	18.64	0.02	10.69	0.23		0.09	3.71
21-HG-030 di 2	0.00	56.32	0.30	8.55	1.32	19.15	0.02	10.34	0.22	0.01	0.10	3.66
Mean	**0.00**	**56.42**	**0.30**	**8.48**	**1.35**	**18.90**	**0.02**	**10.51**	**0.23**	**0.01**	**0.09**	**3.69**
Sigma	**0.00**	**0.13**	**0.01**	**0.10**	**0.05**	**0.36**	**0.00**	**0.25**	**0.01**	**0.00**	**0.01**	**0.04**
SigmaMean	**0.00**	**0.09**	**0.00**	**0.07**	**0.03**	**0.26**	**0.00**	**0.17**	**0.01**	**0.00**	**0.00**	**0.02**

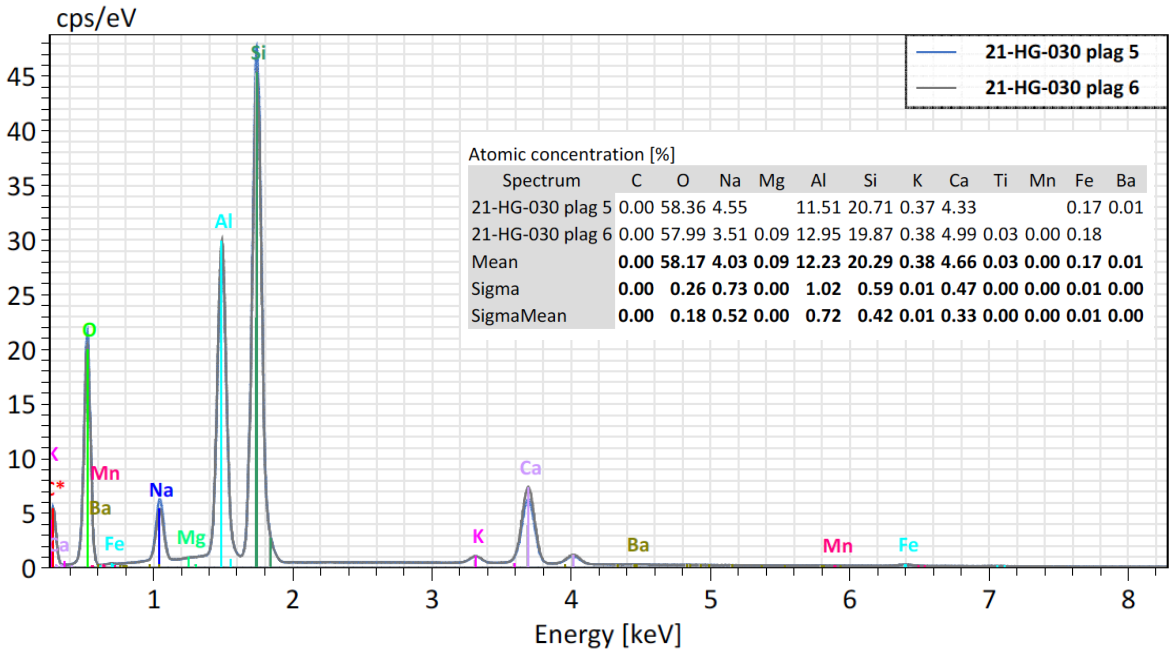
cps/eV
21-HG-030 plag 5
21-HG-030 plag 6
Atomic concentration [%]
Spectrum C O Na Mg Al Si K Ca Ti Mn Fe Ba
21-HG-030 plag 5 0.00 58.36 4.55 11.51 20.71 0.37 4.33 0.17 0.01
21-HG-030 plag 6 0.00 57.99 3.51 0.09 12.95 19.87 0.38 4.99 0.03 0.00 0.18
Mean 0.00 58.17 4.03 0.09 12.23 20.29 0.38 4.66 0.03 0.00 0.17 0.01
Sigma 0.00 0.26 0.73 0.00 1.02 0.59 0.01 0.47 0.00 0.00 0.01 0.00
SigmaMean 0.00 0.18 0.52 0.00 0.72 0.42 0.01 0.33 0.00 0.00 0.01 0.00
Si
Al
O
K
Mn
Na
Ba
Ca
Mg
Fe
Energy [keV]

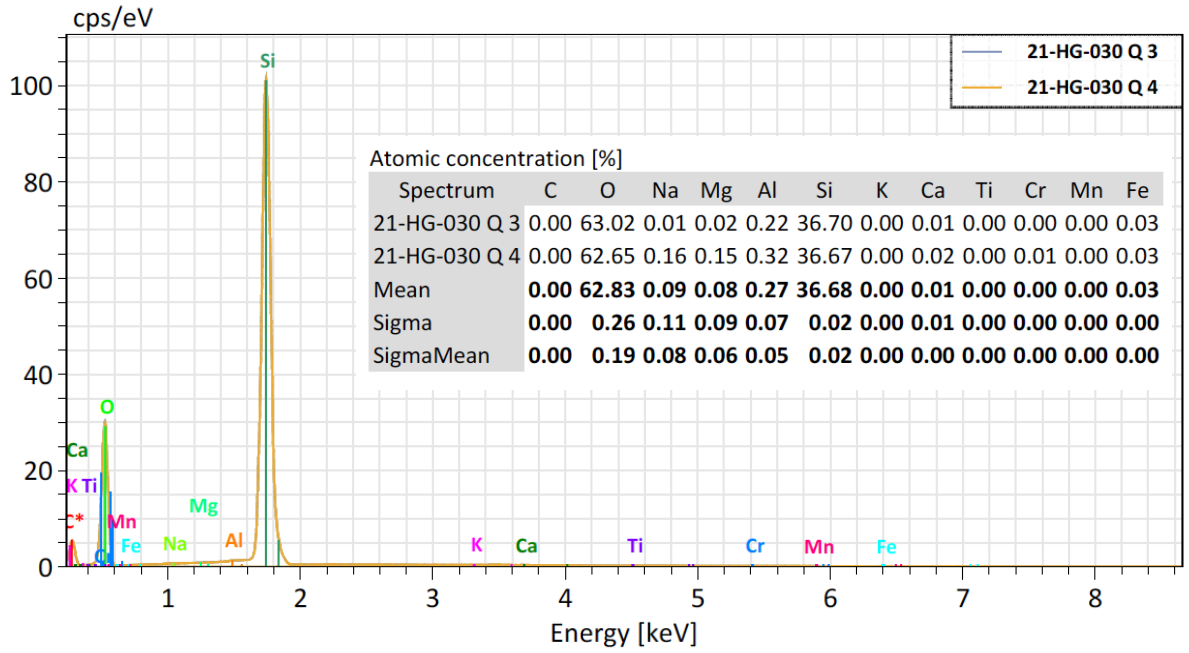
cps/eV
21-HG-030 Q 3
21-HG-030 Q 4
Atomic concentration [%]
Spectrum C O Na Mg Al Si K Ca Ti Cr Mn Fe
21-HG-030 Q 3 0.00 63.02 0.01 0.02 0.22 36.70 0.00 0.01 0.00 0.00 0.00 0.03
21-HG-030 Q 4 0.00 62.65 0.16 0.15 0.32 36.67 0.00 0.02 0.00 0.01 0.00 0.03
Mean 0.00 62.83 0.09 0.08 0.27 36.68 0.00 0.01 0.00 0.00 0.00 0.03
Sigma 0.00 0.26 0.11 0.09 0.07 0.02 0.00 0.01 0.00 0.00 0.00 0.00
SigmaMean 0.00 0.19 0.08 0.06 0.05 0.02 0.00 0.00 0.00 0.00 0.00 0.00
Si
O
Ca
K
Ti
Mg
Mn
Fe
Na
Al
Energy [keV]

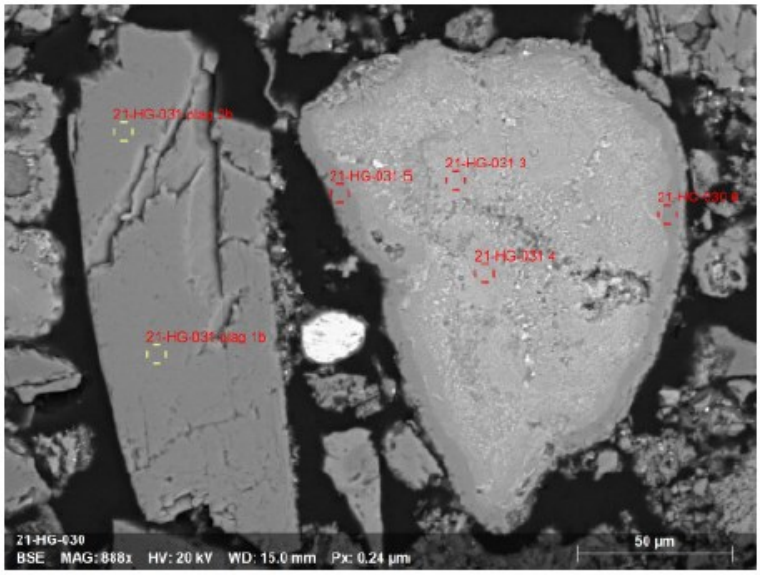

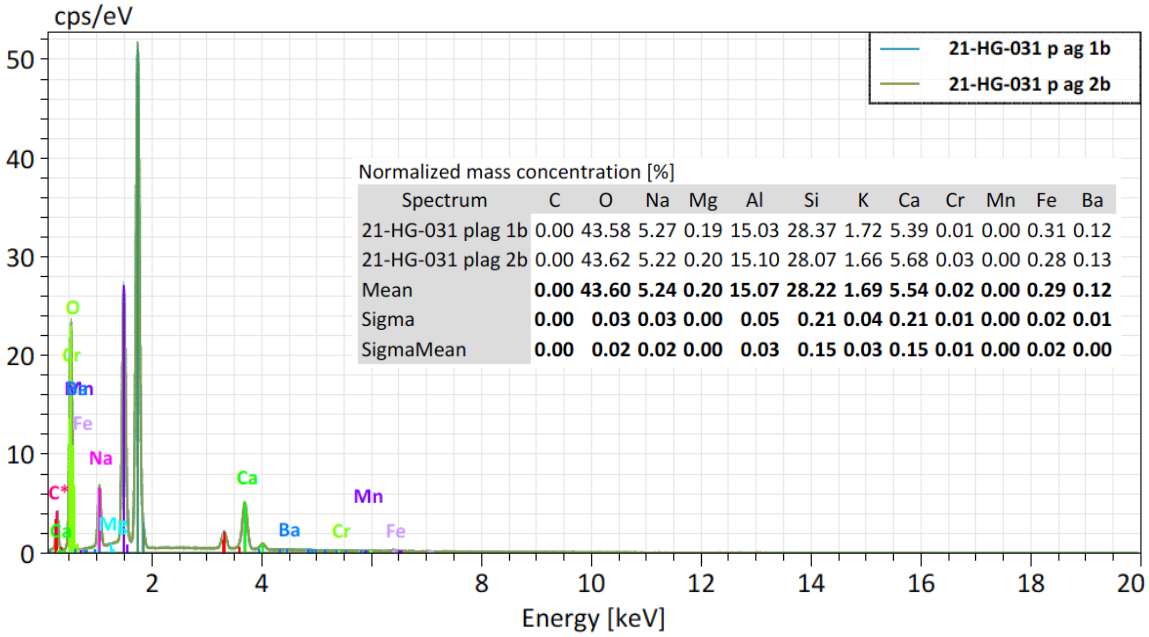

Normalized mass concentration [%]

Spectrum	C	O	Na	Mg	Al	Si	K	Ca	Cr	Mn	Fe	Ba
21-HG-031 plag 1b	0.00	43.58	5.27	0.19	15.03	28.37	1.72	5.39	0.01	0.00	0.31	0.12
21-HG-031 plag 2b	0.00	43.62	5.22	0.20	15.10	28.07	1.66	5.68	0.03	0.00	0.28	0.13
Mean	**0.00**	**43.60**	**5.24**	**0.20**	**15.07**	**28.22**	**1.69**	**5.54**	**0.02**	**0.00**	**0.29**	**0.12**
Sigma	**0.00**	**0.03**	**0.03**	**0.00**	**0.05**	**0.21**	**0.04**	**0.21**	**0.01**	**0.00**	**0.02**	**0.01**
SigmaMean	**0.00**	**0.02**	**0.02**	**0.00**	**0.03**	**0.15**	**0.03**	**0.15**	**0.01**	**0.00**	**0.02**	**0.00**

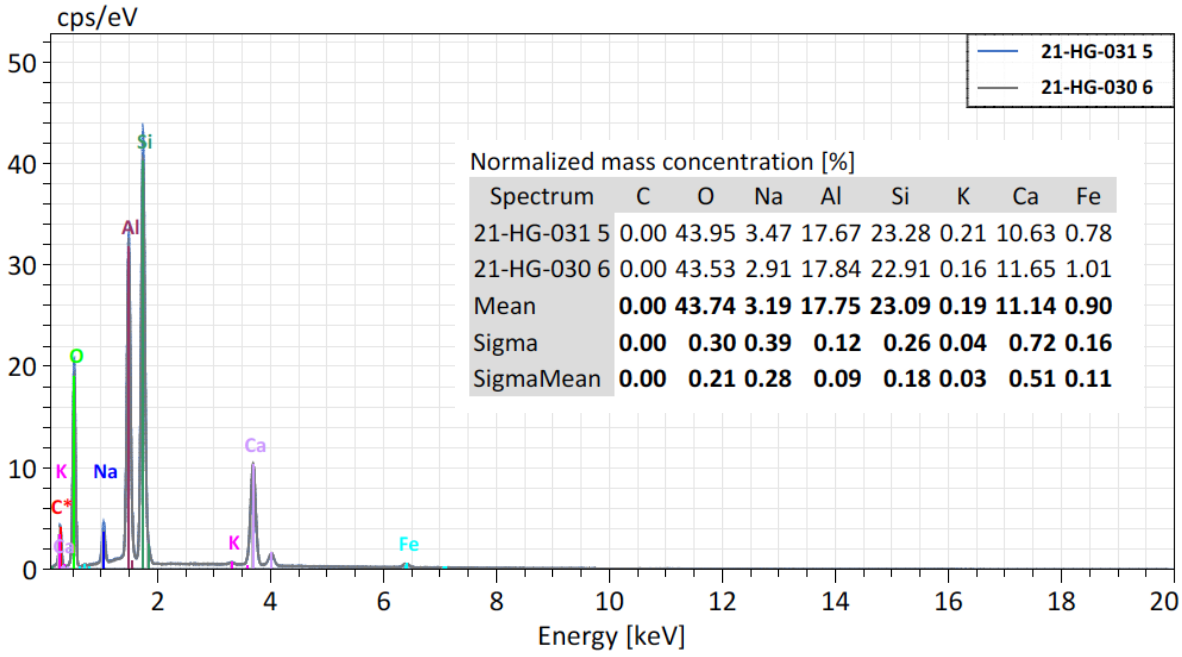

Normalized mass concentration [%]

Spectrum	C	O	Na	Al	Si	K	Ca	Fe
21-HG-031 5	0.00	43.95	3.47	17.67	23.28	0.21	10.63	0.78
21-HG-030 6	0.00	43.53	2.91	17.84	22.91	0.16	11.65	1.01
Mean	**0.00**	**43.74**	**3.19**	**17.75**	**23.09**	**0.19**	**11.14**	**0.90**
Sigma	**0.00**	**0.30**	**0.39**	**0.12**	**0.26**	**0.04**	**0.72**	**0.16**
SigmaMean	**0.00**	**0.21**	**0.28**	**0.09**	**0.18**	**0.03**	**0.51**	**0.11**

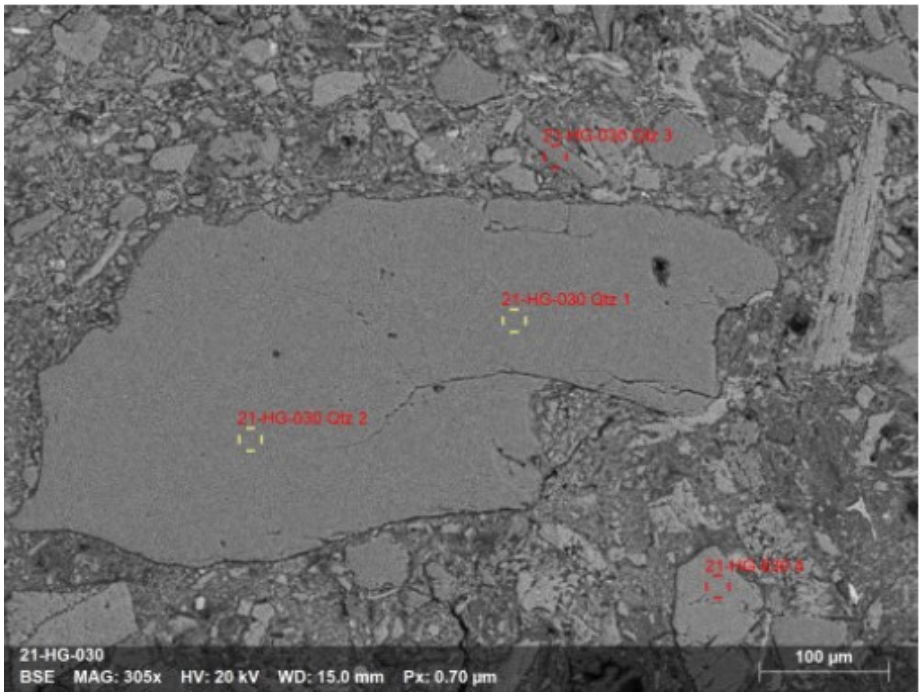

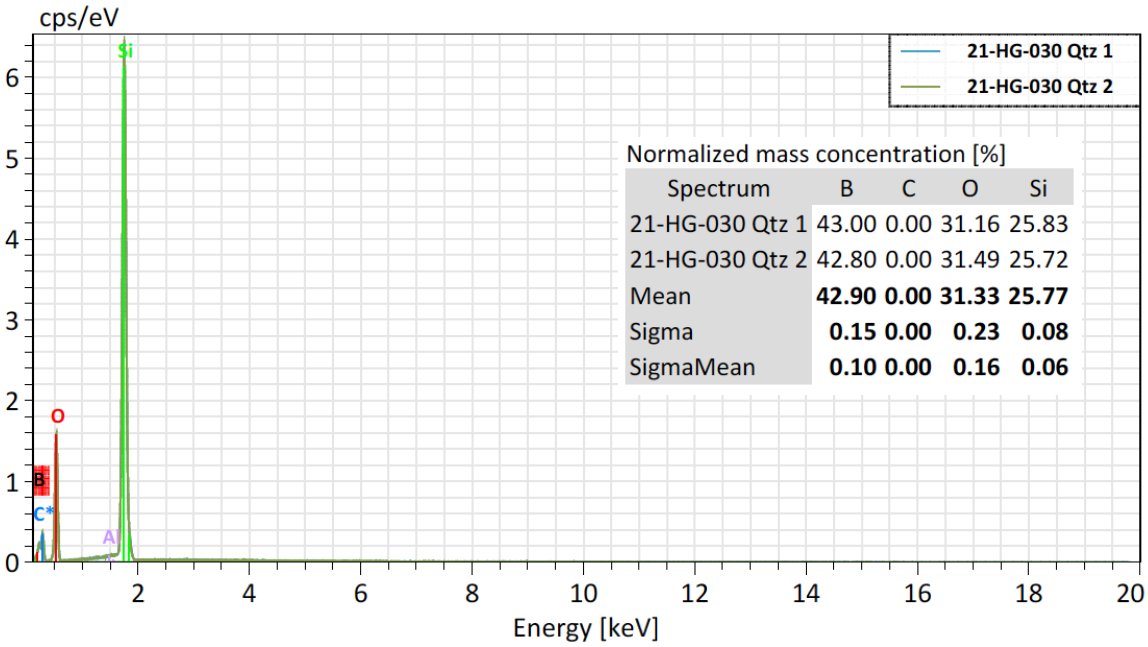

Normalized mass concentration [%]

Spectrum	B	C	O	Si
21-HG-030 Qtz 1	43.00	0.00	31.16	25.83
21-HG-030 Qtz 2	42.80	0.00	31.49	25.72
Mean	**42.90**	**0.00**	**31.33**	**25.77**
Sigma	**0.15**	**0.00**	**0.23**	**0.08**
SigmaMean	**0.10**	**0.00**	**0.16**	**0.06**

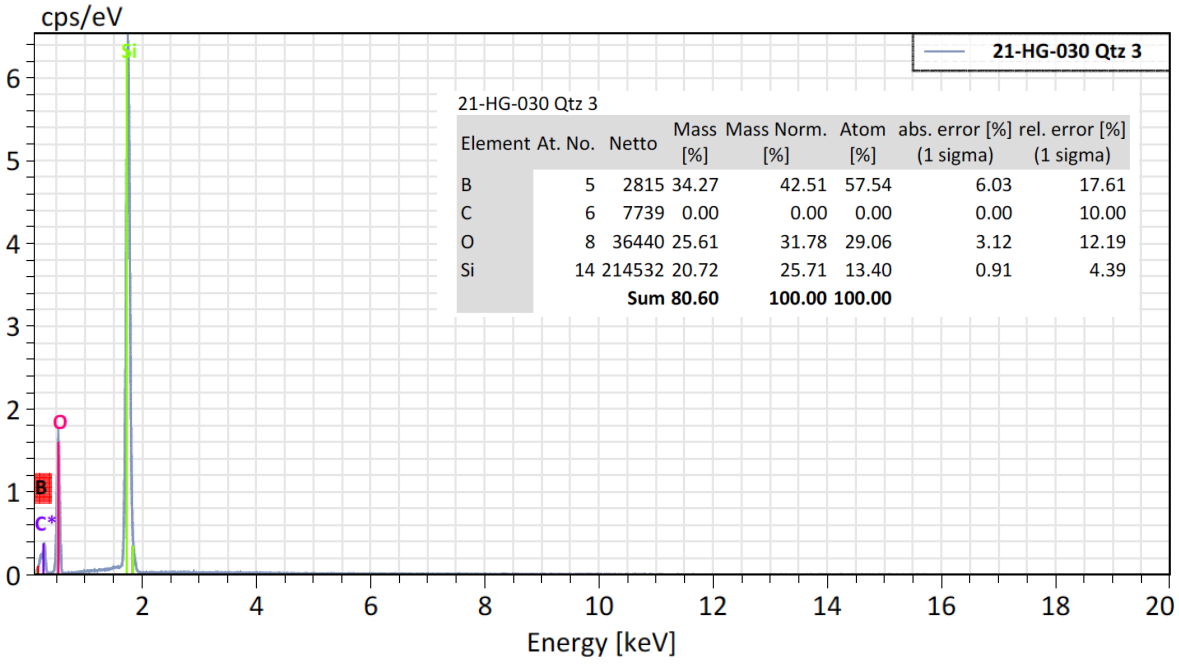

21-HG-030 Qtz 3

Element	At. No.	Netto	Mass [%]	Mass Norm. [%]	Atom [%]	abs. error [%] (1 sigma)	rel. error [%] (1 sigma)
B	5	2815	34.27	42.51	57.54	6.03	17.61
C	6	7739	0.00	0.00	0.00	0.00	10.00
O	8	36440	25.61	31.78	29.06	3.12	12.19
Si	14	214532	20.72	25.71	13.40	0.91	4.39
		Sum	**80.60**	**100.00**	**100.00**		

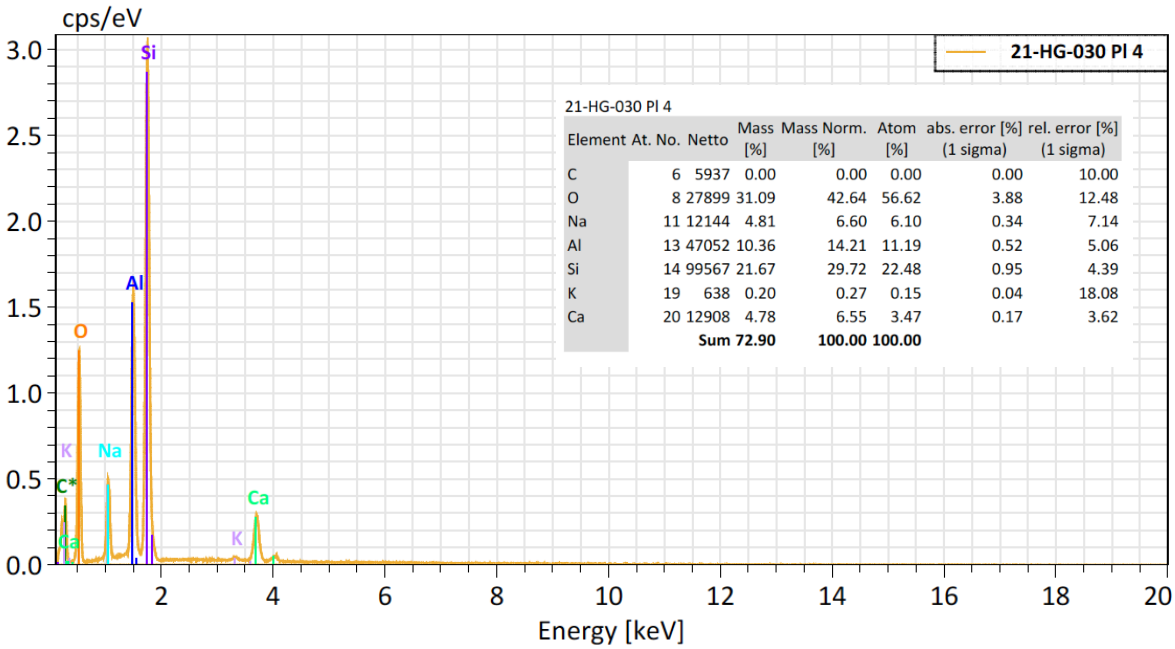

21-HG-030 Pl 4

Element	At. No.	Netto	Mass [%]	Mass Norm. [%]	Atom [%]	abs. error [%] (1 sigma)	rel. error [%] (1 sigma)
C	6	5937	0.00	0.00	0.00	0.00	10.00
O	8	27899	31.09	42.64	56.62	3.88	12.48
Na	11	12144	4.81	6.60	6.10	0.34	7.14
Al	13	47052	10.36	14.21	11.19	0.52	5.06
Si	14	99567	21.67	29.72	22.48	0.95	4.39
K	19	638	0.20	0.27	0.15	0.04	18.08
Ca	20	12908	4.78	6.55	3.47	0.17	3.62
			Sum 72.90	**100.00**	**100.00**		

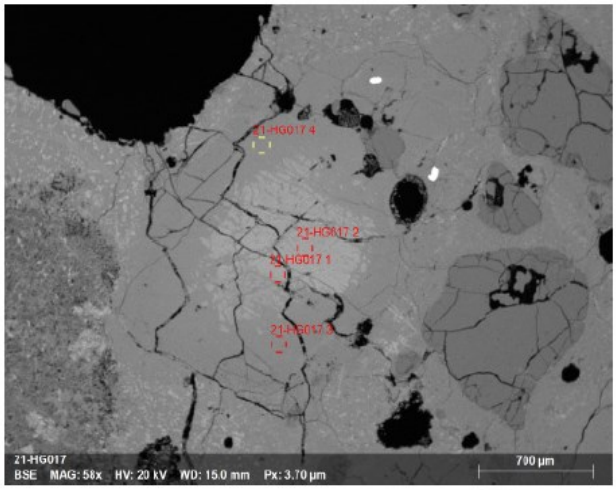

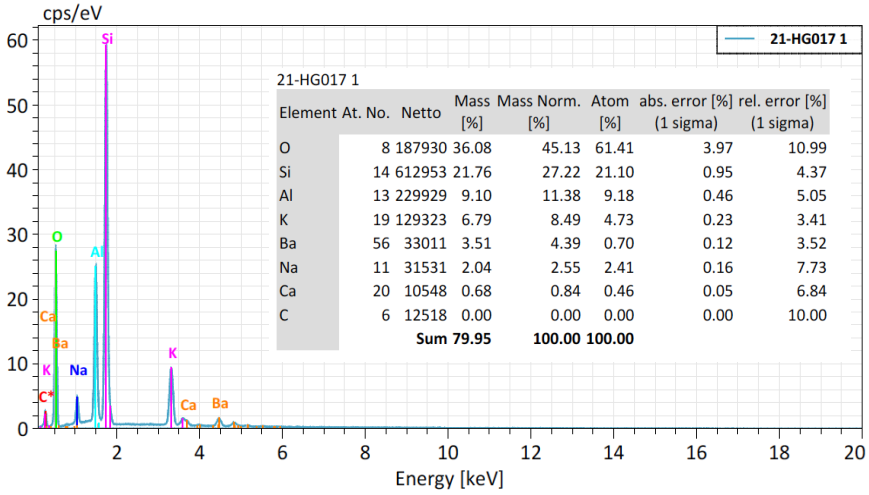

21-HG017 1

Element	At. No.	Netto	Mass [%]	Mass Norm. [%]	Atom [%]	abs. error [%] (1 sigma)	rel. error [%] (1 sigma)
O	8	187930	36.08	45.13	61.41	3.97	10.99
Si	14	612953	21.76	27.22	21.10	0.95	4.37
Al	13	229929	9.10	11.38	9.18	0.46	5.05
K	19	129323	6.79	8.49	4.73	0.23	3.41
Ba	56	33011	3.51	4.39	0.70	0.12	3.52
Na	11	31531	2.04	2.55	2.41	0.16	7.73
Ca	20	10548	0.68	0.84	0.46	0.05	6.84
C	6	12518	0.00	0.00	0.00	0.00	10.00
			Sum 79.95	**100.00**	**100.00**		

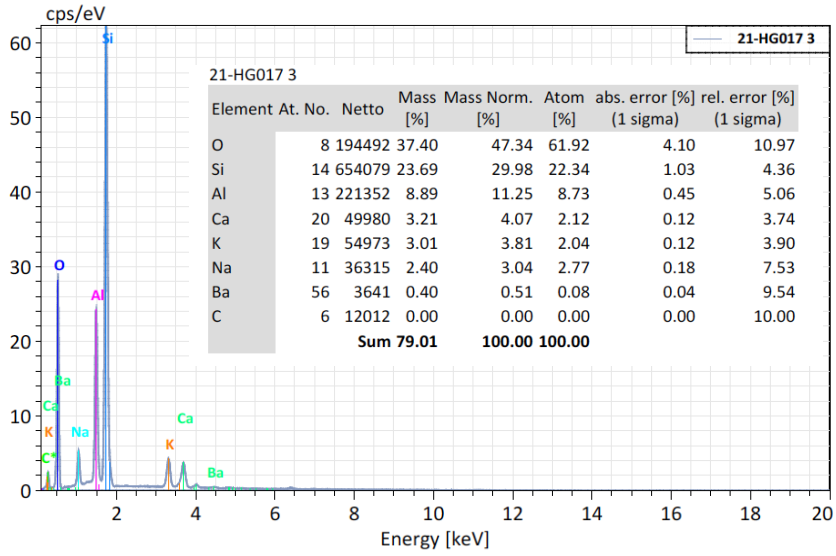

21-HG017 3

Element	At. No.	Netto	Mass [%]	Mass Norm. [%]	Atom [%]	abs. error [%] (1 sigma)	rel. error [%] (1 sigma)
O	8	194492	37.40	47.34	61.92	4.10	10.97
Si	14	654079	23.69	29.98	22.34	1.03	4.36
Al	13	221352	8.89	11.25	8.73	0.45	5.06
Ca	20	49980	3.21	4.07	2.12	0.12	3.74
K	19	54973	3.01	3.81	2.04	0.12	3.90
Na	11	36315	2.40	3.04	2.77	0.18	7.53
Ba	56	3641	0.40	0.51	0.08	0.04	9.54
C	6	12012	0.00	0.00	0.00	0.00	10.00
			Sum 79.01	**100.00**	**100.00**		

BIBLIOGRAPHY

Aasly, K., Malvik, T., and Myrhuag, E.H., 2007. Advance Methods to Characterize Thermal Properties of Quartz :

Ainslie, N.G., MaCkenzie, J.D., Turnbull, D., 1961. Melting Kinetics of Quartz and Cristobalite: General electric Research Laboratory. 65,1718-1724.

Amin, J., Valentine, G.A., 2017. Compound maar crater and co-eruptive scoria cone in the Lunar Crater Volcanic Field (Nevada, USA). J. Volcano. Geotherm. Res. 339, 41–51.

Befus, K.S., Hanson, R.E., Miggins, D.P., Breyer, J.A., Busbey, A.B., 2009. Nonexplosive and explosive magma/wet-sediment interaction during emplacement of Eocene intrusions into Cretaceous to Eocene strata, Trans-Pecos igneous province, West Texas. J. Volcanol. Geotherm. Res. 181, 155–172. https://doi.org/10.1016/j.jvolgeores.2008.12.017 Bennis, K.L., 2019. Reconstructing the 71 Gulch Eruption: Implications for the Evolution of Phreatomagmatic Eruptions and Their Products. University of Missouri - Kansas City. Masters thesis.

Bennis, K.L., 2019. Reconstructing the 71 Gulch Eruption: Implications for the Evolution of Phreatomagmatic Eruptions and Their Products. University of Missouri - Kansas City. Masters thesis.

Bennis, K.L., Graettinger, A.H., 2020. Basaltic phreatomagmatic fissure at 71 Gulch Part 1: sediment magma mingling and eruptive behavior. Bull. Volcanol. 82, 1–17. https://doi.org/10.1007/s00445-020-01416-1

Bonnichsen, B., Godchaux, M.M., 2002. Late Miocene, Pliocene, and Pleistocene geology of southwestern Idaho with emphasis on basalts in the Bruneau-Jarbridge, Twin Falls, and

western Snake River Plain regions. Tecton. Magmat. Evol. Snake River Plain Volcan. Prov. Idaho Geol. Surv. Bull. 30, 233–312.

Bonnichsen, B., Leeman, W.P., Honjo, N., McIntosh, W.C., Godchaux, M.M., 2008. Miocene silicic volcanism in southwestern Idaho: geochronology, geochemistry, and evolution of the central Snake River Plain. Bull. Volcanol. 70, 315–342. https://doi.org/10.1007/s00445-007-0141-6.

Bonnichsen, B., Boroughs, S., Godchaux, M.M., Wolff, J., 2016. From land to lake: Basalt and rhyolite volcanism in the western Snake River Plain, Idaho. F. Guid. 41, 93–125.

Brand BD, White CM (2007) Origin and stratigraphy of phreatomagmatic deposits at the Pleistocene Sinker Butte Volcano, Western Snake River Plain, Idaho. J Volcanol Geotherm Res 160: 319–339. https://doi.org/10.1016/j.jvolgeores.2006.10.007.

Branlund, J.M., Hofmeister, A.M., 2012. Heat transfer in plagioclase feldspar: American Mineralogist. 97, 1145-1154. DOI: http://dx.doi.org/10.2138/am.2012.3968.

Breitkreuz, C., Rocchi, S., 2018. Physical geology of Shallow Magma Systems Dykes, Sills and Laccoliths: Advances in Volcanology. ISBN : 978-3-319-14083-4.

Busby-Spera, C.J., White, J.D.L., 1987. Variation in peperite textures associated with differing host-sediment properties. Bull. Volcanol. 49, 765–776.

Büttner, R., Zimanowski, B., 1998. Physics of thermohydraulic explosions: Physical Review E. 57, 5726-5729 Büttner, R., Dellino, P., La Volpe, L., Lorenz, V., Zimanowski, B., 2002. Thermohydraulic explosions in phreatomagmatic eruptions as evidenced by the comparison between pyroclasts and products from Molten Fuel Coolant Interaction experiments. J. Geophys. Res. Solid Earth 107, ECV 5-1-ECV 5-14. https://doi.org/10.1029/2001jb000511 135.

Casas, D., Pimentel, A., Pacheco, J., Martorelli, E., Sposato, A., Ercilla, G., Alonso, B., Chiocci, F., 2018. Serreta 1998–2001 submarine volcanic eruption, offshore Terceira (Azores): Characterization of the vent and inferences about the eruptive dynamics. J. Volcanol. Geotherm. Res. 356, 127–140. https://doi.org/https://doi.org/10.1016/j.jvolgeores.2018.02.017.

Coffin, M.F., Eldholm, O., 1994. Large igneous provinces: Crustal structure, dimensions, and external consequences: Reviews of Gephysics. 32, 1-36. https://doi.org/10.1029/93RG02508.

Drazin, P.G., 2015. DYNAMIC METEOROLGY | Kelvin-Helmholtz Instability. In: Encyclopedia of Atmospheric Sciences (Second Edition). Academic Press, pp. 343–346. https://doi.org/10.1016/B978-0-12-382225-3.00190-0 .

Dvorak, J.J., 1992. Mechanism of explosive eruptions of Kilauea Volcano, Hawaii. Bull. Volcanol. 54, 638–645. https://doi.org/10.1007/BF00430777.

Einarsson, P., Brandsdottir, B., 1980. Seismological evidence for lateral magma intrusion during the July 1978 deflation of the Krafla volcano in NE- Iceland. J. Geophys. - Zeitschrift fur Geophys. 47, 160–165. https://doi.org/10.2172/890964.

Galletly, A., 2021. Quantitative Characterization of Billwed Structures Along th Margins of Basaltic Intrusions to Determine Process and Timing of Formation: Case Studies from Big Bend National Park., Texas and 81 Gulch, Idaho. University of Missoutri-Kansas City. Masters Thesis.

Gardien, V., Thompson, A.B., Grujic, D., Ulmer, P., 1995. Experimental melting of biotite + plagioclase + quartz ± muscovite assemblages and implications for crustal melting: Journal of Geophysical Research. 100, 15581-15591.

Gardien, V., Thompson, A.B., Ulmer, P., 2000. Melting of Biotite + Plagioclase + Quartz Gneisses: the Role of H2O in the Stability of Amphibole: Journal of Petrology. 41, 651-666.

Godchaux, M.M., Bonnichsen, B., Jenks, M.D., 1992. Types of phreatomagmatic volcanos in the Western Snake River Plain, Idaho, USA. J. Volcanol. Geotherm. Res. 52, 1–25. https://doi.org/10.1016/0377-0273(92)90130-6.

Graettinger, A.H., 2012. Building Ice-Age Askja: Processes, Products and Paleoclimate: University of Pittsburgh. Masters thesis.

Graettinger, A.H., Skilling, I.P., McGarvie, D.W., and Hoskuldsson, A., 2012. Intrusion of basalt into frozen sediments and generation of Coheren-Margined Volcaniclastic Dikes (CMVD's). Journal of Volcanology and Geothermal Research, 217-218, 30-38.

Graettinger A, Bennis KL, Brand B, Reynolds E, Nolan J (2020) Basaltic phreatomagmatic fissure at 71 Gulch Part 2: unusual pyroclasts from sediment magma mingling and melting. Bull Volcanol. https://doi. org/10.1007/s00445-020-01417-0Gudmundsson, A., 1984. Formation of dykes, feeder-dykes, and the intrusion of dykes from magma Chambers. Bull. Volcanol. 47, 537–550. https://doi-org.proxy.library.umkc.edu/10.1007/BF01961225.

Hanson, R.E., Hargrove, U.S., 1999. Processes of magma/wet sediment interaction in a large-scale Jurassic andesitic peperite complex, northern Sierra Nevada, California. Bull. Volcanol. 60, 610–626. https://doi.org/10.1007/s004450050255.

Hooten, J.A., Ort, M.H., 2002. Peperite as a record of early-stage phreatomagmatic fragmentation processes: An example from the Hopi Buttes volcanic field, Navajo

Nation, Arizona, USA. J. Volcanol. Geotherm. Res. 114, 95–106. https://doi.org/10.1016/S0377-0273(01)00282-7.

Houghton, B.F., Schmincke, H.U., 1989. Rothenberg scoria cone, East Eifel: a complex Strombolian and phreatomagmatic volcano. Bull. Volcanol. 52, 28–48.

Jenks D., M., Bonnichsen, B., 1989. Subaqueous Basalt Eruptions Into Pliocene Lake Idaho, Snake River Plain, Idaho. Idaho Geol. Surv. Bull. 17–34.

Kano, K., 2002. Middle Miocene volcaniclastic dikes at Kukedo, Shimane Peninsula, SW Japan: Fluidization of volcaniclastic beds by emplacement of syn-volcanic andesitic dikes. J. Volcanol. Geotherm. Res. 114, 81-94. https://doi.org.10.1016/S0377-0273(01)002839.

Kwon, C.W., Gihm, Y.S., 2017. Fluidization of host sediments and its impacts on peperites-forming processes, the Cretaceous Buan Volcanics, Korea. J. Volcanol. Geotherm. Res. 341, 84–93. https://doi.org/10.1016/j.jvolgeores.2017.05.019.

Larson, E., 1929. The Temperatures of Magmas: American Mineralogist. 14, 81-94.

Lavine, A., Aalto, K.R., 2002. Morphology of a crater-filling lava lake margin, the Peninsula tuff cone, Tule Lake National Wildlife Refuge, California: Implications for formation of peperite textures. J. Volcanol. Geotherm. Res. 114, 147-163, https://doi.org/10.1016/S0377-0273(01)00285-2

Malde, H.E., Powers, H.A., 1962. Upper Cenozoic stratigraphy of western Snake River Plain, Idaho. Geol. Soc. Am. Bull. 73, 1197–1220.

Malde, H.E., 1972. Stratigraphy of the Glenns Ferry Formation from Hammett to Hagerman, Idaho. US Govt. Print. Off.

McLean, C.E., Brown, D.J., Rawcliffe, H.J., 2016. Extensive soft-sediment deformation and peperite formation at the base of a rhyolite lava: Owyhee Mountains, SW Idaho, USA. Bull. Volcanol. 78. https://doi.org/10.1007/s00445-016-1035-2.

Morrow, L.S., 1996. Geology of Guffey Butte, western Snake River Plain. Idaho Univ. Idaho. Masters thesis.

Muirhead, J.D., Van Easton, A.R., Re, G., White, J.D.L., Ort, M.H., 2016. Monogenetic volcanoes fed by interconnected dikes and sills in the Hopi Buttes volcanic field, Navajo Nation, USA: Bull Volcanol. 78, 1-16. DOI 10.1007/s00445-016-1005-8

Németh, K., White, C.M., 2009. Intra-vent peperites related to the phreatomagmatic 71 Gulch Volcano, western Snake River Plain volcanic field, Idaho (USA). J. Volcanol. Geotherm. Res. 183, 30–41. https://doi.org/10.1016/j.jvolgeores.2009.02.020.

Németh, K., Kósik, S., 2020. Review of explosive hydrovolcanism Geosci 10. https://doi.org/10.3390/geosciences10020044.

Nichols, C., Graettinger, A.H., 2021. The influence of regional stress and structural control on the shape of maar crates: Volcanica. 4, 23-29. https://doi.org/10.30909/vol.04.01.2339.

Re, G., White, J.D.L., Muirhead, J.D., Ort, M.H., 2016, Subterraneal fragmentation of magma during conduit initiation and evolution in the shallow plumbing system of the small-volume Jagged Rocs volcanoes (Hopi Buttes Volcanic Field, Arizona, USA): Bull Volcanol. 78, 1-20. DOI 10.1007/s00445-016-1050-3

Ross, P.-S., G. Carrasco-Núñez, and P. Hayman (2017). Felsic maar-diatreme volcanoes: a review". Bulletin of Volcanology 79.2. issn: 1432-0819. doi: 10.1007/s00445-016-1097-1.

Senger, K., Millett, J., Planke, S., Ogata, K., Eide, C.H., Festoy, ., Galland, O., Jerram, D.A., 2017. Effects of igneous intrusions on the petroleum system: a review: First Break. https://doi.org/10.3997/1365-2397.2017011.

Shervais, J.W., Shroff, G., Vetter, S.K., Matthews, S., Hanan, B.B., McGee, J.J., 2002. Origin and evolution of the western Snake River Plain: Implications from stratigraphy, faulting, and the geochemistry of basalts near Mountain Home, Idaho. Tecton. Magmat. Evol. Snake River Plain Volcan. Prov. 30, 343–361.

Skilling, I.P., White, J.D.L., McPhie, J., 2002. Peperite: a review of magma–sediment mingling. J. Volcanol. Geotherm. Res. 114, 1–17.

Smith, J.V., 1972. Critical Review of Synthesis and Occurrence of Plagioclase feldspar and Possible Phase Diagram: The Journal of Geology. 80, 505-525.

Sonder, I., Harp, A.G., Graettinger, A.H., Moitra, P., Valentine, G.A., Büttner, R., Zimanowski, B., 2018. Meter-Scale Experiments on Magma-Water Interaction. J. Geophys. Res. Solid Earth 123, 10,597-10,615. https://doi.org/10.1029/2018JB015682.

Starostin, A.B., Barmin, A.A., Melnik. O.E., 2005. A transient model for explosive and phreatomagmatic eruptions: Journal of Volcanology and Geothermal Research. 143, 133-151.

Strekeisen, A., 2020, Embayed textures:https://www.alexstrekeisen.it/english/vulc/embayed.php (accesed July 2022)

Sun, S., McDonough, W.F., 1995. The composition of the Earth: Chemical Geology. 120, 223-253. https://doi.org/10.1016/0009-2541(94)00140-4.

Swirydczuk, K., Larson, G.P., Smith, G.R., 1981a. Volcanic ash stratigraphy of the Glenns Ferry and Chalk Hills Formations, western Snake River Plain, Idaho. Idaho Bureau of Mines and Geology, Department of Lands.

Swirydczuk, K., Wilkinson, B.H., Smith, G.R., 1981b. Synsedimentary lacustrine phosphorites from the Pliocene Glenns Ferry Formation of southwestern Idaho. J. Sediment. Res. 51, 1205–1214.

Swirydczuk, K., Larson, G.P., Smith, G.R., 1982. Volcanic ash beds as stratigraphic markers in the Glenns Ferry and Chalk Hills Formations from Adrian, Oregon, to Bruneau, Idaho. Cenozoic Geol. Idaho Idaho Bur. Mines Geol. Bull. 26, 543–558.

Valentine, G.A., Gregg, T.K.P., 2008. Continental basaltic volcanoes — Processes and problems. J. Volcanol. Geotherm. Res. 177, 857–873. https://doi.org/https://doi.org/10.1016/j.jvolgeores.2008.01.050

Valentine, G.A., Graettinger, A.H., Sonder, I., 2014. Explosion depths for phreatomagmatic eruptions. Geophys. Res. Lett. 41, 3045–3051. https://doi.org/10.1002/2014GL060096.

Valentine, G. A., White, J. D. L., Ross, P.-S., Graettinger, A. H., Sonder, I., 2017. Updates to Conceptson Phreatomagmatic Maar-Diatremes and Their Py-roclastic Deposits: Frontiers in Earth Science 5. issn:2296-6463. doi: 10.3389/feart.2017.00068.

van Otterloo, J., Ort, M.H., Cruden, A.R., 2018. Unique occurrence of a folded in-vent dike: New insights on magma-water mixing. Geology 46, 379–382.

Waichel, B.L., de Lima, E.F., Sommer, C.A., Lubachesky, R., 2007. Peperite formed by lava flows over sediments: An example from the central Parana Continental Flood Basalts,

Brazil: Journal of Volcanology and Geothermal Research. 159, 343-354. https://doi.org/10.1016/j.jvolgeores.2006.07.009.

Watson, C.A, 1999. The Evolution of Guffey Butte Tuff Cone Complex, Western Snake River Plain, Idaho: Boise State University. Masters Thesis.

White, C.M, Michaud, H.M., 2004. The Influence of Subsurface Geology on Eruptive Styles at the Guffey Butte Maar, Western Snake River Plain, Idaho: Rocky Mountain (56th Annual) and Cordilleran (100th Annual) Joint Meeting (May 3-5). Geological Society of Americas Abstracts with Programs, 36, 84.

White, J.D.L., Houghton, B.F., 2006. Primary volcanoclastic rocks: Geology. 34, 677-680. DOI:10.1130/G22346.1.

White, J. and P.-S. Ross (2011). "Maar-diatreme volcanoes: A review". Journal of Volcanology and Geothermal Research 201.1-4, pp. 1–29. issn: 0377-0273. doi:10.1016/j.jvolgeores.2011.01.010.

White, J.D.L., 1996. Impure coolants and interaction dynamics of phreatomagmatic eruptions. J. Volcanol. Geotherm. Res. 74, 155–170. https://doi.org/10.1016/S0377-0273(96)00061-3.

White, J.D.L., 1996. Pre-emergent construction of a lacustrine basaltic volcano, Pahvant Butte, Utah (USA): Bull Volcanol. 58, 249-262.

White, J.D.L., McPhie, J., Skilling, I., 2000. Peperite: A useful genetic term. Bull. Volcanol. 62, 65–66. https://doi.org/10.1007/s004450050293.

White, C.M., Hart, W.K., Bonnichsen, B., Matthews, D., 2002. Geochemical and Sr-isotopic variations in western Snake River Plain basalts, Idaho. Tecton. Magmat. Evol. Snake River Plain Volcan. Prov. Idaho Geol. Surv. Bull. 30, 329–342.

White, C.M., Michaud, H.M., 2004. The Influence of Subsurface Geology on Eruptive Styles at the Guffey Butte Maar, Western Snake River Plain, Idaho: Geological Society of America Abstract with Programs, v. 36, no. 4, p. 84.

Wilson, L., Head III, J.W., 1981. Ascent and eruption of Basaltic Magma on the Earth and Moon. J. Geophys. Res. 86, 2971–3001. https://doi.org.proxy.library.umkc.edu/10.1029/JB086iB04p02971

Wilson, L., Head III, J.W., 2002. Heat transfer and melting in subglacial basaltic volcanic eruptions: Implications for volcanic deposit morphology and meltwater volumes. Geol. Soc. Spec. Publ. 202, 5–26. https://doi.org/10.1144/GSL.SP.2002.202.01.02

Wohletz, K.H., 1986. Explosive magma-water interactions: Thermodynamics, explosions mechanisms, and field studies: Bulletin of Volcanology. 48, 245-264.

Wood, S.H., Clemens, D.M., 2002. Geologic and tectonic history of the western Snake River Plain, Idaho and Oregon. Tecton. Magmat. Evol. Snake River Plain Volcan. Prov. Idaho Geol. Surv. Bull.

Zimanowski, G.F., Volker, L., 1991. Quantitative experiments on phreatomagmatic explosions: Journal of Volcanology and Geothermal Research. 48, 341-358.

Zimanowski, B., Büttner, R., Lorenz, V., Häfele, H.G., 1997. Fragmentation of basaltic melt in the course of explosive volcanism. J. Geophys. Res. Solid Earth 102, 803–814. https://doi.org/10.1029/96JB02935.

VITA

Hannah received her Bachelor of Arts in Geology from The College of Wooster in 2020 under the guidance of Dr. Meagen Pollock. While attending The College of Wooster Hannah was a teaching assistant for Processes and Concepts laboratory, Hydrology lecture and laboratory, and Natural Hazards lecture. She performed research spanning the topics of geochemistry, petrology, and physical volcanology. In addition to a sociological and economical study of farming diversification in Ohio. She presented two of her research projects at the American Geophysical Unions National conference in San Francisco, California (December 2019).

In December of 2022, Hannah graduated from the University of Missouri-Kansas City with her Master of Science in Environmental and Urban Geosciences. Through the course of 1.5 years as a master's student, she participated in research at State University of New York at Buffalo's Geohazard Field Station and conducted field work at Guffey Butte, Idaho. Hannah was a graduate teaching assistant while completing her masters, in addition to being the MELT Labs resident pub board artist. She presented her research at the Geological Society of Americas Connects conference in Portland, Oregon (October 2021).

Hannah is affiliated with the Association of Women Geoscientists, the Geological Society of America, the American Geophysical Union, GeoLatinas, and Asian American and Pacific Islanders in Geosciences.